Smartphone-Fluidic Imaging System for Cell-Based Therapy in Diabetes and its Complication

---

A

Dissertation

Presented to

the faculty of the School of Engineering and Applied Science

University of Virginia

---

in partial fulfillment

of the requirements for the degree

Doctor of Philosophy

by

Xiaoyu Yu

May 2024

APPROVAL SHEET

This
Dissertation
is submitted in partial fulfillment of the requirements
for the degree of
Doctor of Philosophy

Author: Xiaoyu Yu

This Dissertation has been read and approved by the examing committee:

Advisor: Jianjie Ma

Advisor:

Committee Member: Craig Meyer

Committee Member: Gustavo Rohde

Committee Member: Chuanxi Cai

Committee Member: Huiwang Ai

Committee Member:

Committee Member:

Accepted for the School of Engineering and Applied Science:

Jennifer L. West, School of Engineering and Applied Science

May 2024

ACKNOWLEDGEMENTS

First and foremost, I want to express my heartful thanks to my PhD advisor, Dr. Jianjie Ma. His intuitive and insightful advice has helped me tremendously during the progression of my thesis. His always has faith in me, and his encouragement really helped me during hard time. I could not have finished my thesis without the help from him. In the meantime, I want to thank my mentors, Dr. Jose Oberholzer, and Dr. Yong Wang. Their unwavering support and insightful guidance have been pivotal to my PhD career, providing me with knowledge and confidence to pursue my research with diligence and passion.

Also, I am grateful to my thesis committee chair, Dr. Craig Meyer, who has provided me with invaluable help and advice on my research plan and on the progress of my PhD career. Also, my appreciation goes to my other committee members, Dr. Gustavo Rohde, Dr. Huiwang Ai, and Dr. Chuanxi Cai for their constructive feedback and encouragement throughout this journey.

Special thanks are due to Kimberly Fitzhugh-Higgins, the graduate student coordinator from Biomedical Engineering (BME) department. Her advice has been extremely helpful in navigating me through the complexities of graduate studies.

On top, I want to thank my dear colleagues, Dr. Yuan Xing, Yi He, and Pu Zhang, my undergraduate student, Amelia Bergeron, and Dr. Yiyu Zhang from our collaboration lab. They have provided immense help and support for my research.

In addition, I want to mention that chapter 3 of this thesis is constructed based on [111], and chapter 4 of this thesis is constructed based on [134]. I want to express my thanks again to my mentors Dr. Wang and Dr. Oberholzer, my committee Dr. Huiwang Ai, my colleagues, Dr, Yuan Xing, Yi He, Pu Zhang, Dr. Yiyu Zhang, and also to Dr. Melur Ramasubramanian, Farid Ghamsari, and Emily Lin. I could not have finished my projects and made the publications without their help.

Sincere appreciation to my parents for their life experience as adults and consolation as family. The chat with them every weekend made me feel that although my home is tens of thousand miles away, my family is always at my side.

Finally, I want to acknowledge the most important person in my life- my fiancée Xinrui Shi. As a fellow PhD student, she provided help on my research with her knowledge and experience. More importantly, as a life partner, her assistance at home allowed me to better concentrate on my

career, and her emotional support encouraged me and gave me strength during hard times. I couldn't have made it to the end of my PhD without her at my back.

TABLE OF CONTENTS

Acknowledgements ii
LIST OF FIGURES viii
LIST OF ABBREVIATIONS xii
ABSTRACT 1
CHAPTER 1. Introduction 2
  1.1 Type 1 Diabetes and islet transplantation 2
    1.1.1 Insulin and blood glucose regulation 2
    1.1.2 Type 1 and Type 2 Diabetes 2
    1.1.3 Treatments to T1D 3
      1.1.3.1 Insulin therapy 3
      1.1.3.2 Immune therapy 4
      1.1.3.3 Islet transplantation 4
      1.1.3.4 Other cell-based therapies 5
  1.2 Microfluidic technology 6
  1.3 Paper microfluidic 8
    1.3.1 Paper microfluidic fabrication 10
    1.3.2 Blood separation on paper 12
  1.4 Digital imaging system 12
    1.4.1 Smartphone based imaging system 12
    1.4.2 Microscopic setup 13
    1.4.3 Fluorescence imaging 15
    1.4.4 Digital image/video analysis 17
CHAPTER 2. A Smartphone-Fluidic Digital Imaging Analysis System for Pancreatic Islet Mass Quantification 22
  2.1 Introduction 22
    2.1.1 Islet equivalent and Dithizone staining 22
    2.1.2 Islet morphology 24

2.2 Methodology 24
  2.2.1 Design of the Smartphone-Fluidic Digital Imaging Analysis system 24
    2.2.1.1 Design of Image acquisition system 24
    2.2.1.2 Design of the microfluidic device 26
    2.2.1.3 Photo-lithography-fabrication of microfluidic device 27
  2.2.2 Video analysis algorithm 28
    2.2.2.1 Cell identification and segmentation 29
    2.2.2.2 Cell tracking 36
  2.2.3 Feature extraction 37
    2.2.3.1 Size, IEq and volume quantification 38
    2.2.3.2 Circularity and solidity quantification 41
    2.2.3.3 Trapped islet percentage estimation: 43
  2.2.4 Human islets preparation and manual mass quantification 44
    2.2.4.1 Human islets loading and video recording on-chip 45
2.3 Results and discussion 45
  2.3.1 Human islet quantification 45
  2.3.2 Islet size estimation 46
    2.3.2.1 Estimation of equivalent diameters 47
    2.3.2.2 Estimation of volume 47
    2.3.2.3 Comparison of two volume estimation methods 49
  2.3.3 Islet morphology estimation 49
  2.3.4 Islet purity estimation 51
  2.3.5 Conclusion 53
CHAPTER 3. Smartphone-Fluidic Fluorescence Imaging System for Studying Islet Physiology 55
3.1 Introduction 55
  3.1.1 Islet metabolism 55
  3.1.2 The Glucose Stimulated Insulin Secretion Assay 57

3.1.3 Islet Perifusion 58
3.1.3.1 Microfluidic islet perifusion system 58
3.1.3.2 Fluorescence dyes in islet perifusion 59
3.1.3.3 Genetically Encoded Fluorescence Protein Bio-Indicator in islet perifusion 60
3.1.3.4 Other stimuli in islet perifusion 60
3.2 Methodology 61
3.2.1 Design of the Smartphone-Fluidic Fluorescence Digital Imaging Analysis system 61
3.2.2 Mouse islet isolation and culture 64
3.2.3 Buffer solution preparation 65
3.2.4 Fluorescence imaging of islets 65
3.2.5 Software development for islet imaging 66
3.3 Results and discussion 66
3.3.1 Imaging resolution validation of optical system 66
3.3.2 Intracellular insulin stimulator-secretion coupling factors in response to stimuli 70
3.3.2.1 The effects of photo-bleach and shear stress 70
3.3.2.2 Response of fluo-4 labeled islets to glucose stimulation 71
3.3.2.3 Response of fluo-4 labeled islets to other stimuli 73
3.3.2.4 Response of Rhodamine-123 labeled islets to other glucose 75
3.3.3 Fluorescence imaging of islets labelled with GEFPIs 76
3.3.3.1 The effects of photo-bleach and shear stress 76
3.3.3.2 Response of GEFPI-labeled islets to glucose stimulation 77
3.3.3.3 Response of GEFPI-labeled islets to other stimuli 78
3.3.4 Conclusion 80
CHAPTER 4. Smartphone-based Imaging Systems for Blood Creatinine Measurement 81
4.1 Introduction 81
4.1.1 Kidney function Assessment 81

4.1.1.1 Clinical measurement for creatinine 81

4.1.1.2 Point-of-care creatinine test 83

4.2 Methodology 83

4.2.1 Fabrication of channel structure on paper 83

4.2.2 Design of paper-microfluidic device 83

4.2.3 Jaffe-reaction-based creatinine assay 84

4.2.4 Enzyme-based fluorescence creatinine assay 86

4.2.5 Design of fluorescence imaging system 88

4.3 Result 90

4.3.1 Result of Jaffe-reaction-based assay 90

4.3.1.1 Assay validation in 96 well plate 90

4.3.1.2 Assay validation on paper using creatinine standards 91

4.3.1.3 Assay validation on paper using whole blood samples 95

4.3.2 Result of Enzyme-based fluorescence assay 96

4.3.3 Conclusion 98

CHAPTER 5. Conclusion, Discussion and Future Direction 99

References 101

LIST OF FIGURES

Figure 1. Working principle of microscope. **(A)** Refraction light path in a convex lens. **(B)** Working principle of single-convex-lens magnification system. **(C)** Working principle of double-convex-lens magnification system. 15

Figure 2. (A) Working principle of fluorescence. **(B)** An example spectrum of fluorescence (GFP). **(C)** Light path of a typical fluorescence microscope. 17

Figure 3. Demonstration of manual IEq assessment. 23

Figure 4. Design of smartphone case. 25

Figure 5. Demonstration of the magnification system in the smartphone-based imaging system. 26

Figure 6. (A) Overall design of the micorfluidic device. **(B)** A scale marker was put into the design such that the size in pixels can be transformed into size in μm. **(C)** An example image of islets flowing through the viewing area. 27

Figure 7. Flow chart of video processing algorithm. **(A)** Flow chart of the individual frame analysis. **(B)** Flow chart of cell matching algorithm. 29

Figure 8. Demonstration of background subtraction. 31

Figure 9. Demonstration of Otsu threshold. 32

Figure 10. Demonstration of distance transform (DT). The BW image (top left) went through DT (top right) first, and then thresholding (bottom). 33

Figure 11. Demonstration of morphological operation. The DT image (top left) went through morphological erosion (top right), and then morphological dilation (bottom). 35

Figure 12. Demonstration of watershed algorithm. This algorithm requires both the original BW image, and the image processed by distance transform and morphological operations as input. It outputs a clustering result with each cluster representing one cell. 35

Figure 13. Demonstration of cell tracking. **(A)** Matching process demonstration of a cell that already exists in the frame at T-1. Distances between the cell in yellow rectangle in frame T and all the cells in frame T-1 were calculated. The cell pair with shortest distance (orange) matches. **(B)** Matching process demonstration of a cell that does not exist in the frame at T-1. Distances

between the cell in light blue rectangle in frame T and all cells in frame T-1 were calculated. All the distances exceed a threshold. So, the cell in the light blue rectangle is new cell. 37

Figure 14. Demonstration of ellipse fitting. 39

Figure 15. Demonstration of volume calculated by revolving 2D ellipse around major axis. 40

Figure 16. Demonstration of volume calculated by revolving 2D ellipse around minor axis. 41

Figure 17. Demonstration of circularity and solidity calculation... 42

Figure 18. Demonstration of islet purity (trapped islet percentage) calculation. **(A)** Two islets trapped in aciner tissue, with purity of 67.31% and 66.73% respectively. **(B)** A free islet with purity of 99.05%. 44

Figure 19. Comprison between manuual counting and smartphone-based counting. Six human islets samples of varied sample sizes were assessed by both manual counting and the smartphone-based system. 46

Figure 20. Distribution of islet diameter. The mean diameter of the islet sample is 99.87 ± 53.91 µm. 47

Figure 21. Comparison between volume calculated from traditional IEq assessment method (IEqV) and the one obtained from smartphone system (EFV). 48

Figure 22. Distribution curves of volume calculated from two different methods (revolving 2D ellipse around major axis and minor axis). 49

Figure 23. Islets circularity distribution. The islet sample has an average circularity of 0.591 ± 0.127.. 50

Figure 24. Islets solidity distribution. The islet sample has an average solidity of 0.853 ± 0.107. 51

Figure 25. Trapped islet percentage and morphology assessment of islets from middle layer. The islet sample has an average DTZ$^+$ ratio of 0.576 ± 0.223, average circularity of 0.534 ± 0.102, and average solidity of 0.793 ± 0.102. 52

Figure 26. Trapped islet percentage and morphology assessment of islets from top layer. The islet sample has an average DTZ$^+$ ratio of 0.735 ± 0.213, average circularity of 0.635 ± 0.139, and average solidity of 0.853 ± 0.107.. 53

Figure 27. The process of islet metabolism.. 57

Figure 28. Design of the smartphone-based fluorescnece imaging system. 61

Figure 29. Optical principle of the smartphone-based fluroescence system.......................... 62

Figure 30. Design of the microfluidic device. The two images on the left are the front and side view of the device. The image on the right is an amplified view of the cell-loading wells. 63

Figure 31. Simulation of liquid diffusion in the microfluidic device. **(A)** Simulation setup in COMSOL. **(B)** Simulation result of glucose concentration vs. time. 64

Figure 32. Validation of the magnification system. **(A)** Images of the resolution targets. The lowest resolved groups (Group 7) are highlighted using red box in the image on the left**,** and the image on the right is the zoom -in image of the highlighted area with a yellow vertical line cut in the middle of the horizontal line pairs. **(B)** The corresponding cross-sectional plot of the intensity along the yellow vertical line. 67

Figure 33. Validation of the optical system with no magnification. **(A)** Images of the resolution targets. The lowest resolved groups (Group 3) are highlighted using red box in the image on the left**,** and the image on the right is the zoom -in image of the highlighted area with a yellow vertical line cut in the middle of the horizontal line pairs. **(B)** The corresponding cross-sectional plot of the intensity along the yellow vertical line. 69

Figure 34. Representative tracings of $[Ca^{2+}]_i$ in mouse islets following continuous addition of 2 mM glucose (Fluo-4). 71

Figure 35. Representative tracings of $[Ca^{2+}]_i$ in mouse islets following glucose stimulation at varying concentrations (8 and 20 mM) (Fluo-4)... 72

Figure 36. Representative tracings of $[Ca^{2+}]_i$ in mouse islets following 14 mM glucose and 30 mM KCl stimulation (Fluo-4)... 73

Figure 37. Representative tracings of $[Ca^{2+}]_i$ in mouse islets following 14 mM glucose and 200 μM Diazoxide stimulation (Fluo-4)... 74

Figure 38. Representative tracings of $[Ca^{2+}]_i$ in mouse islets following 250 μM Tolbutamide stimulation (Fluo-4). 75

Figure 39. Representative tracings of Ψmito in mouse islets following 14 mM glucose stimulation (Rhodamine-123). 76

Figure 40. Representative tracings of $[Ca^{2+}]_i$ in mouse islets following continuous addition of 2 mM glucose (GEFPI). 77

Figure 41. Representative tracings of $[Ca^{2+}]_i$ in mouse islets following 14 mM glucose stimulation (GEFPI). 78

Figure 42. Representative tracings of $[Ca^{2+}]_i$ in mouse islets following 14 mM glucose and 200 μM Diazoxide stimulation (GEFPI). 79

Figure 43. Representative tracings of $[Ca^{2+}]_i$ in mouse islets following 250 μM Tolbutamide stimulation (GEFPI). 80

Figure 44. Design of the paper microfluidic device. 84

Figure 45. Design of the cassette that is used to hold the paper microfluidic device. **(A)** Lid of the cassette. **(B)** Bottom of the cassette. **(C)** Image of the assembled cassette (with paper microfluidic device loaded in it) taken by smartphone camera. 86

Figure 46. Design of the specifically designed multi-well device. **(A)** Top view of the device. **(B)** Bottom view of the device. **(C)** Overall design of the device. 89

Figure 47. Validation of Jaffe reaction in 96 well plate. **(A)** Image of Jaffe reaction result of standard samples. **(B)** Plot of Hue vs. concentration of the standard samples. A straight line was fitted to the data points. 91

Figure 48. Validation of Jaffe reaction on Whatman filter paper. Picric acid, Sodium Hydroxide, and creatinine samples were added sequentially to the paper. **(A)** Image of Jaffe reaction result of standard samples. **(B)** Plot of Hue vs. concentration of the standard samples. A straight line was fitted to the data points. 92

Figure 49. Validation of Jaffe reaction on Whatman filter paper. Sodium Hydroxide was pre-coated on the paper. The mix of Picric acid and creatinine samples were then added to the paper. **(A)** Image of Jaffe reaction result of standard samples. **(B)** Plot of Hue vs. concentration of the standard samples. A straight line was fitted to the data points. 93

Figure 50. Validation of the effect of blood separation membrane and long-distance diffusion on Jaffe reaction. **(A)** Image of Jaffe reaction result of standard samples. **(B)** Plot of Hue vs. concentration of the standard samples. A straight line was fitted to the data points. 94

Figure 51. Validation of paper microfluidic device using whole blood samples. **(A)** Image of testing result of standard samples. **(B)** Plot of Hue vs. concentration of the standard samples. A straight line was fitted to the data points. 96

Figure 52. Representative result of enzymatic fluorescence assay for creatinine measurement. **(A)** Fluorescence image of enzymatic assay result of standard samples. **(B)** Plot of fluorescence vs. concentration of the standard samples. A straight line was fitted to the data points 97

Figure 53. Validation of enzymatic fluorescence creatinine assay on human samples. 98

LIST OF ABBREVIATIONS

SFDIA	Smartphone-Fluidic Digital Imaging Analysis
GEFPI	Genetically Encoded Fluorescent Protein Indicator
T1D	Type 1 Diabetes
T2D	Type 2 Diabetes
PDMS	Polydimethylsiloxane
CMOS	Complementary Metal Oxide Semiconductor
POC	Point of Care
IEq	Islet Equivalent
DTZ	Dithizone
PLA	Polylactic Acid
FOV	Field of View
BW	Black and White
DT	Distance Transform
EFV	Ellipse-Fitting-based Volume
IEqV	IEq-based Volume
RGB	Red Green Blue
HSV	Hue Saturation Value
PBS	Phosphate-Buffered Saline
KRB	Krebs Ringer Buffer
VDCC	Voltage-Dependent Calcium Channels
GSIS	Glucose Stimulated Insulin Secretion
ELISA	Enzyme-Linked Immunosorbent Assay
GFP	Green Fluorescent Protein
AAV	Adeno-Associated Virus

ABSTRACT

Diabetic nephropathy is a serious complication of both Type 1 and 2 diabetes. Islet transplantation, a cell-based therapy, has become a successful therapy for T1D that is able to achieve tight glycemic control without the needs of insulin injection.

In order to achieve long-term glycemic control, it is essential to have better evaluation of isolated human islet mass and function prior to islet transplantation. In **Aim1** of the thesis, we developed a smartphone-fluidic Digital Imaging Analysis (SFDIA) System, in combination with a microfluidic technique for islet mass assessment. With the system, we quantified islets by tracking multiple moving islets in a microfluidic channel and received a relatively consistent result. Furthermore, the software can analyze and extract key human islet mass parameters, including quantity, size, volume, IEq, morphology, and purity, which are not fully obtainable from the traditional manual counting methods. In **Aim2,** we equipped the SFDIA system with fluorescence imaging capability, and used the system to study the islets' functionality. We evaluated the system capability by performing real-time fluorescence imaging on mouse islets labelled with either chemical fluorescence dyes or genetically encoded fluorescent protein indicators (GEFPIs). The results showed that the system was capable of analyzing key beta-cell insulin stimulator-release coupling factors in response to various stimuli with high-resolution dynamics and good signal to noise ratio.

Creatinine is a waste product of muscle metabolism that is filtered out of the blood by the kidneys. High levels of creatinine in the blood indicates impaired renal function. As a result, creatinine has been an important indicator to monitor post-islet-transplant. In **Aim3**, we attempted to build a point-of-care (POC) paper-based device for whole blood creatinine measurement. We tested the device with mice whole blood samples, and proved that the device was able to take quantifiable readings to reflect creatinine concentration. Furthermore, we developed a multi-well enzymatic fluorescence assay with the help of the SFDIA system to measure creatinine in serum. We validated the assay using 30 human samples, and proved that the measurement from the assay aligned with the clinical readings.

CHAPTER 1. Introduction

1.1 Type 1 Diabetes and islet transplantation

Diabetes mellitus is a chronic disease characterized by abnormally high levels of glucose in the blood. It occurs when the pancreas does not produce enough insulin or when the body cannot effectively use the insulin it produces[1].

1.1.1 Insulin and blood glucose regulation

Insulin is a peptide hormone produced by beta cells of the pancreatic islets. It originates from the proinsulin, which is a single-chain polypetide that is composed of three domains: A, B chains, and C-peptide[2]. Before secretion, the proinsulin is packaged into transport vesicles and undergoes enzymatic cleavage by endopeptidases, known as prohormone convertases (PC1 and PC2), along with the exoprotease carboxypeptidase E. These enzymes cleave at two sites on the C-peptide, liberating insulin, a two-chain polypeptide hormone (A chain and B chain connected by disulfide bonds), and C-peptide, which are both stored in the vesicle until they are released into the bloodstream upon glucose stimulation[3].

The primary job of insulin is to facilitate the absorption of glucose from bloodstream into cells of various tissues. It does so by binding to insulin receptors on the surface of cells. This leads to the activation of the insulin receptor's intrinsic tyrosine kinase activity, which further phosphorylates insulin receptor substrates inside the cells. As a result, the PI3K-AKT pathway is activated, and promotes the movement of glucose transporter vesicles to the cell membrane, facilitating the uptake of glucose into the cell[4].

1.1.2 Type 1 and Type 2 Diabetes

Diabetes can be mainly categorized into Type 1 Diabetes (T1D) and Type 2 Diabetes (T2D). T1D, also known as insulin-dependent diabetes, typically develops early in life but can occur at any age. It's an autoimmune disease, meaning it arises from an erroneous attack by the body's immune system. Specifically, the immune system targets and destroys the insulin-producing beta cells in the pancreas, leading to little or no insulin production. As a result, glucose cannot enter cells and instead builds up in the bloodstream, resulting in high blood glucose levels[5]. T2D, on the other side, is relatively more common and often develops later in life. In T2D, the body develops resistance to insulin, meaning that cells are less responsive to insulin's effects and consequently do not take up glucose efficiently. Initially, the pancreas compensates by producing more insulin. Over time, the beta cells cannot keep up with the increased demand for insulin, leading to its relative deficiency. Both insulin resistance and deficiency contribute to high blood glucose levels in Type 2 diabetes[6]. In this work, studies were developed for a small aspect of T1D treatment.

Type 1 diabetes (T1D) is a devastating disease affecting ~1.6 million Americans and costing ~$18 billion per year in the US [7]. T1D can typically be diagosed through blood tests. One example is the Glycated hemoglobin test. This is done by measuring the percentage of glycated Hemoblobin A1c (HbA1c) in the plood, and assess the extent of glucose attachment to hemoglobin to estimate the average blood suger level over the lifespan of red blood cells. As a result, this test can give an estimation of blood sugar level over the past two to three months [8]. An A1c level below 5.7% is normally considered to be normal, an A1c level between 5.7%-6.4% is normally considered to be pre-diabetes, while 6.5% or higher A1c level can be considered to be diabetes. Another example is the fasting blood glucose test, which is a test that measures the level of blood glucose after a period of fasting (normally, individuals are required to abstain from consuming any food or beverages for 8 hours before the test) [9]. As a result, the fasting blood glucose test can measure the baseline blood glucose level, and blood glucose level lower than 5.6 mmol/L is often considered to be normal, blood glucose level of 5.6 mmol/L to 6.9 mmol/L is considered prediabetes, and blood glucose level above 7.0 mmol/L is considered to be diabetes.

1.1.3 Treatments for T1D

1.1.3.1 Insulin therapy

Currently, the standard treatment for T1D involves lifelong insulin therapy, where the patients need to take exogenous insulin to replace or supplement the body’s natural insulin to maintain the blood glucose level. This therapy was first introduced in the early 1920s [10], and became popular when animal insulin was made commercially available for clinical use. More recently, manufactured ‘human’ insulin became available. This is done through the process called recombinant DNA technology [11], where the insulin production gene is inserted into the bacteria or yeast cell. Insulin can be harvested from the culture mediums of the genetically modified cells, and made aviable to use after purification. Patients can take insulin through multiple daily injections using syringes. Nowadays, insulin pump, which is also referred as artificial pancreas [12], has been made available for diabetes treament, and can continuously infuse insulin into human body. With the help of insulin sensor and a closed-loop controlling system to adjust the amount of insulin, the insulin pump is proved to be more efficient in insulin delivery and can greatly alleviates patients' discomfort [12]. While insulin therapy is effective in managing blood sugar levels, it still has several drawbacks including does not restore the natural regulatory mechanisms of insulin production and can be burdensome for patients [13].

1.1.3.2 Immune therapy

Although at the current stage, no treatments have been proven to effectively reverse diabetes, attempts has been made on this task. One example is immune therapy, which aims to restore the immune tolerance of human body and halt the destruction of beta cells by the immune system, and thereby preserve/restore the insulin production [14]. One example is the regulatory T cell therapy. This therapy is currently undergoing phase 2 clinical trial. Regulatory T cells (Tregs) are known to suppress excessive immune responses and prevent autoimmune reactions. In this therapy, Tregs can be isolated from patients' own blood from a healthy donor. The isolated Tregs are expanded in laboratory and infused back into the patient through intravenous injection, or administered directly into a specific organ or site where immune dysregulation occurs. The infused Tregs can directly interact with immune cells, or secrete anti-inflammatory cytokines to suppress harmful immune responsese, and thus alleviate the auto-immune destruction on islet beta cells [15]. Immune therapy is one of the therapies that can potentially restore beta-cell funciton in the long term. However, this therapy is still in the experimental stage, and it can potentially induce side effects by modulating the immune system of the human body [15].

1.1.3.3 Islet transplantation

Islet transplantation is another therapy that aims at the reversal of T1D. In brief, this therapy involves the isolation of pancreatic islets from healthy donors[16], which is performed using enzymatic degradation and density centrifugation[17]. The isolated islets undergoe quantification and qualification anlysis before a sufficient amount of islets are transplanted into the diabetic patients through percutaneous cannulation of a brach of the portal vein.

The concept of islet transplantation first occurred back in 1893, but the first successful transplantation experiment took place in the year of 1972, in which rodents' islets were transplanted into a diabetic rodent model with proper *in vivo* function [18]. However, initial human trials were unsuccessful, largely due to the difficulty of isolating islets from the pancreas and the lack of effective immunosuppression until 1990 due to the big advancement on islet isolation techniques, including the use of enzymes to digest the pancreas and the development of purification methods to separate the islets from other pancreatic cells [18]. The major breakthrough in islet transplantation came in the year 2000 with the Edmonton Protocol. The Edmonton protocol involves infusing a substantial islet mass (>13,000 islet equivalent/kg from 2-3 donors. The concept of islet equivalent will be introduced later in this chapter) into the liver portal vein system while utilizing corticosteroid-free immunosuppressants, including rapamycin and tacrolimus[19, 20]. One study shows that most of the patients (~80%) achieved insulin independence within one year, but only 10% of them remained free from insulin dependency after five years [21]. Ever since, attempts has been made to replicate Edmonton's protocal in multiple clinical trials [22-24]. Variances in success rate were observed due to the differences in islet preparation procedure, immuno suppresive protocal and doses of transplanted islets. In a recent multicenter study sponsored by the NIH, transplanted outcomes were observed on 48 patients. In the experiments, 5000 islet equivalent/kg was transplanted initially, and 4000 islet equivalent/kg of subsequent dose was transplanted if the first dose did not achieve insulin independance. The result found that 87.5% of patients achieved normal HbA1c levels at one year, with a slightly lower rate of 71.0% at two years [24]. In our own study, the UIC protocal was used for islet transplantation. Compared to the Edmonton protocol, treatment with etanercept and exenatide was used on top of the immunosuppresion regime used in the Edmonton protocol, and a lower number of islet equivalent was transplanted. Based on the results from 44 subjects, 80% of patients became completely insulin free during the first year, with a retention rate of 55% at five years [22].

1.1.3.4 Other cell-based therapies

Other than the transplantation of isolated human islets, other cell-based therapy are also under development in the aim of curing T1D, and one example is stem cell therapy [10, 25]. Stem cells are the type of cells that can develop into many different cell types. For the purpose of T1D, researches are trying to induce the stem cell to differentiate into islet beta cells to replace the destroyed beta cells to produce insulin. Efforts has been made to encapsulate progenitor cells that are derived from Embryonic Stem Cells (ESCs) in a device and implant the device under skin. These progenitor cells are designed to mature into insulin-producing beta cells after transplantation [10].

Despite the different types of cell-based therapy for T1D, islet transplantation has been proved to be the most efficient cell therapy. However, challenges remain in the field of islet transplantation. However, the long term islet survival rate and insulin secretion remains a big challenge due to various factors including hypoxic liver enviornment, immune attacks (despite the immunosppression treatment), etc. Meanwhile, the shortage of pancreas doners is another limitation to islet tranplantion.

1.2 Microfluidic technology

Microfluidics is the technology that deals with the manipulation and control of small volumes of fluids on the micrometer scale [26]. It involves the precise handling of fluids, typically in channels or chambers with dimensions ranging from tens to hundreds of micrometers [26, 27]. Microfluidic devices are usually fabricated using bio-compatible materials, meaning that they are non-toxic for various biomedical applications. In my lab, Microfluidic devices are fabricated using a bio-compatible material called the Polydimethylsiloxane (PDMS). This is a type of silicone elastomer that possesses unique properties, including: Transparency, which is advantageous for optical detection and imaging in microfluidics; Easy fabrication, which gives it the flexibility to achieve different feature designs; Gas permeability, which can allow the exchange of oxygen, carbon dioxide, and is very helpful for various biological studies; Hydrophobicity, which means that PDMS can repel water, and is a big advantage in controlling fluid flow and preventing cross contamination [28]. In addition to the advantages brought by the materials, other strengths of microfluidic technology also include:

1. Miniaturization, which is one of the most significant advantages of microfluidics. By scaling down the dimensions of channels and chambers, microfluidic devices can perform complex tasks using small volumes of fluids.
2. Precision and Control, meaning that microfluidic devices provide precise control over fluid flow, mixing, and reaction parameters. This is enabled by the micro-scale dimension and

well-defined geometries of microchannels, and can result in better control over reaction conditions, reduced variability, and enhanced reproducibility.

3. Integration, meaning that microfluidic devices have the potential to integrate multiple laboratory functions onto one single chip. This integration eliminates the need for manual sample handling and reduces the risk of contamination.
4. Automation, which can be achieved by valve structure with external digital controller. This allows for high-throughput analysis, reducing human error, and improving reproducibility.
5. Rapid Analysis, which is also the result of the miniature dimension. The small volumes and confined fluid flows in microchannels result in shorter diffusion distances and faster reaction times. This allows for rapid analysis and high-throughput screening, making microfluidics ideal for applications that require quick results.
6. Portability and Accessibility, which is another advantage brought by the miniature dimension. This means that microfluidic technology can be applied to Point-Of-Care (POC) diagnostic devices that can be used in remote or resource-limited settings.

Because of these advantages, microfluidic technology has shown great potential in various biomedical applications. Some examples include:

1. Medical diagnostics. Microfluidic technology has seen wide application in medical diagnosis through the determination of ions, sugars, metabolites, proteins and etc. One study in 2019 demonstrated a wearable microfluidic device that can monitor glucose and lactate level for the diagnosis of diabetes and issues with transplanted surgery[29]. Another study in 2020 introduced a device that implemented the idea of ELISA with the help of magnetic nanoparticles to detect insulin in serum samples, which can contribute to the diagnosis of diabetes[30].
2. High-throughput screening. Microfluidics has the capability to do rapid screening of large libraries of compounds or genes, facilitating drug discovery, functional genomics, and identification of novel targets. One study in 2018 introduced a microfluidic design that incorporate similar concept of flow cytometry to screen the binding of monoclonal antibodies to cell surface[31].
3. Organ on a chip. This is a technology that aims to recreate the structure and function of human organs on miniature chips. It involves the development of microfluidic devices that incorporate living cells and tissue constructs to simulate the behavior and responses of

actual organs[31]. One study in 2010 introduced a lung-on-a-chip device through a multi-regions design. The different regions are separated by thin PDMS membrane, with alveolar epithelial cells, pulmonary microvascular endothelial cells cultured in different regions, to mimic the alveolar-capillary barrier structure[32].

The fabrication of a microfluidic device mainly involves three parts: mode fabrication, channel fabrication and assembly. **Mode fabrication** is done using a technique called the Photolithography[33]. A thin layer of photosensitive material called a photoresist is deposited onto the substrate. The photoresist is then exposed to ultraviolet (UV) light through a photomask, which contains the pattern of the desired microchannels and structures. The exposed photoresist undergoes a chemical reaction, making it either soluble (positive photoresist) or insoluble (negative photoresist) in a subsequent development step. After baking the photoresist at high temperature, the soluble part of the photo-resist can be washed away by development solution, leaving behind the desired pattern of channels and structures on the substrate. In **channel fabrication** step, various techniques can be employed depending on the materials used for fabrication. As mentioned earlier, PDMS is used in my lab. The liquid state PDMS is mixed with a curing agent and poured onto the mode created in the previous step. After heating for a certain amount of time, PDMS will cross-link and converts into solid state, and thus form the desired channel structures. In **assembly** step, the PDMS channel structure can either be bonded to glass or other substrate to create simple single layer device, or bounded to PDMS membrane, PDMS pillars and other PDMS channel structure to create multi-layer devices or very complicated 3D structures.

1.3 Paper microfluidic

Paper microfluidics is an emerging field that combines the principles of microfluidics with the simplicity and versatility of paper. It involves the use of paper as a substrate or medium to manipulate and control small volumes of fluids for various applications [34, 35].

The basic idea behind paper microfluidics is to take advantage of the unique properties of paper, such as its capillary action, porosity, and low cost, to create microfluidic devices. These devices typically consist of patterned paper channels or networks that can transport fluids, along with other components such as hydrophobic barriers, valves, and detection zones.

The main advantages of paper microfluidics include simplicity, low cost, ease of use, and portability. Paper is widely available, inexpensive, and does not require complex fabrication processes. It also allows for easy integration with other components, such as sensors or detection methods, making it suitable for point-of-care diagnostics, environmental monitoring, and resource-limited settings.

Paper microfluidics has been applied in various fields, including healthcare, environmental monitoring, food safety, and etc.[35] Some common applications include:

1. Diagnostic testing: Paper microfluidic devices can be used for rapid and low-cost diagnostic tests by integrating specific reagents and detection methods to the device. One study in 2014 suggests a paper microfluidic device to test nitrite in saliva based on Griess reaction, which can be used in the diagnosis of periodontitis[36]. One study in 2015 used paper-based electrochemical sensor detect nucleotide sequence characteristic of DNA from the hepatitis B virus[37]. Another study in 2017 describes a paper-based colorimetric biosensor for the measurement of glucose level in tear samples using TMB as the chromogenic reagent[38]. In the most recent COVID-19 pandemic, paper microfluidics also played an important role in the diagnosis of the disease. The concept of PCR was successfully incorporated onto the paper platform with the help of golden nano partials, which makes the diagnosis of COVID-19 available for home test[39].
2. Environmental testing: Paper-based sensors can be designed to detect various environmental contaminants, such as pH measurements, or detection of heavy metals, pesticides, and pollutants. One study in 2014 used paper microfluidics along with Android smartphone to measure nitrite concentration and the pH of water samples. This work demonstrated that paper-based device has the capability to detect multiple targets on single design and could obtain immediate result with simple operation. Another study in 2014 developed a paper microfluidic device, and utilized both colorimetric and electrochemical detection method to quantify metal in aerosolized particulate matter filter sample. With smart multiplexing design, the device was able to detect 6 different heavy metals.
3. Food safety: Paper-based assays can be developed to detect foodborne pathogens or contaminants, ensuring the safety of food products. One of the most common applications is to use the paper device for bacteria detection. One example is a work published 2017 that combined electrochemical and colorimetric method into one device to detect enzymes including β-galactosidase, β-glucuronidase, β-glucosidase that are produced by Escherichia coli and Enterococcus that are commonly found in food and water[40]. Another work

published in 2017 used a distance-based method to quantify salmonella. Since the quantification for this device is done by reading length of the color band, this device can operate with human eye[41].

1.3.1 Paper microfluidic fabrication

The fabrication of paper microfluidics often involves manual cutting and folding. However, manual methods have the drawbacks of low accuracy, low consistency, and low efficiency. To resolve these drawbacks, researchers have tried different fabrication processes [42, 43], which include:

1. Laser treatment. Laser treatment method utilized laser cutting machines to emit high-powered laser beam, and by moving the laser beam across the paper according to the design file, the machine can cut or change the property of the paper along the desired paths. In 2013, a work reported using CO_2 laser cutting machine to fabricate paper device[44]. In the study, the laser can burn the paper following the pre-designed path, and can from hollow microstructures that act as hydrophobic barrier. According to this study, the method can fabricate a typical 4cm by 4cm paper device within 20 seconds. The laser treatment method can create patterns on paper with low time consumption and high accuracy, and the expensive equipment has always been a big limitation to the method [43].
2. Wax printing. Wax printing involves depositing melted wax onto the paper selectively to create hydrophobic barriers or fluidic channels. The wax acts as a physical barrier, controlling the flow of fluids through the paper[45]. This method is one of the most widely used fabrication method for paper microfluidics. One study in 2012 reported using solid wax printer to print wax on filter paper with pre-designed patterns. After baking the device at high temperature, the melted wax could penetrate into the paper to form hydrophobic barrier[46]. However, one big problem with wax printing method is that wax printers are becoming more and more difficult to access due to the low demand on market. As a result, wax dipping method has become an alternative strategy for wax printing. A study in 2011 reported to use reusable iron mold to create desired structure. The mold is created using laser printer. The mold can be attached to paper through magnetic force, and by dipping the mold-attached paper into melted wax, hydrophobic wall structure can be created[47].

However, due to requirement to make iron mold, this method is expensive and time consuming as compared to the original wax printing method.

3. 3-D printing, which is a technology that involves printing Polypropylene filament directly onto paper. This method is relatively similar to the wax printing method. After the printing, the paper device needs to be re-baked at high temperature to allow the melted material penetrate into the paper and form barriers to achieve flow control. One work in 2020 reported this method[48]. Due to the limit of access of the wax printer, this is a good alternative to the wax printing method. Moreover, 3-D printer can be used to print complicated 3-D structure on top of the paper device using materials with relatively higher melting point to achieve functions that are otherwise impossible for the paper microfluidic device.
4. Inkjet etching. This method is migrated from the manufacturing method used in semiconductor. In this method, filter paper needs to be soaked in solution of polystyrene dissolved in toluene for a certain amount of time. The polystyrene can turn the paper to hydrophobic once the solvent evaporates. Then inkjet printer is used to print toluene following the pre-designed pattern repeatedly, so that the toluene can remove the polystyrene in the designated area. A work in 2010 reported this method, and used it to fabricate an immune-chemical sensing device to measure human IgG concentration[49].
5. Photolithography. This is similar to the technology used in the fabrication of traditional microfluidic device. This is done by exposing UV light through a photomask to the paper that is precoated with liquid state photoresist. The photomask is printed with desired features, such that these feature areas will cross-link after UV-exposure, while the rest of the areas can be washed away by development solutions[50]. One work in 2013 reported coupling octadecyl trichlorosilane to paper fiber and used UV-lithography technique to created designed pattern[51]. This work used the technique to measure nitrite in food samples. Overall, photolithography technique a produce device with reasonable cost and time consumption at relatively high accuracy. As reported in a study in 2008, this technique can create channels as small as 200 μm without the requirement for clean room environment and the aid of expensive aligner[50].

6. Other techniques. In addition to the methods mentioned above, lots of other technologies have also been applied in the fabrication of paper microfluidic devices, like ink stamping, computer-controlled knife cutting, screen printing, plasma treatment and etc.

1.3.2 Blood separation on paper

Sometimes, a paper microfluidic device needs to separate serums from whole blood samples. This can be achieved by using a specifically designed separation that is made of glass fiber or cellulosic. The membrane is designed such that the red blood cell can be effectively trapped by the fiber structure while still remains a high serum permeability[52]. As reported in a study in 2012, wax-printing technique was used to create a blood separation device using the blood separation membrane and the filter paper, and the device was able to separate serum from the whole blood with 24-55% hematocrit without dilution in 2 min[53].

1.4 Digital imaging system

With the advances in computation technology in recent years, digital imaging system starts to be widely applied in various applications, like industrial inspection and quality control[54], robotics and automatic driving[55]. This is especially true in the field of biomedical research, since medical imaging like Computed Tomography and Magnetic Resonance Imaging (MRI)[56], digital microscopy and molecular imaging[57] and lots of other applications, all benefit significantly from the fast development of digital signaling/imaging system. A digital imaging system often encompasses various components including image acquisition, image processing, image output/display and data storage.

1.4.1 Smartphone based imaging system

Nowadays, smartphone has become a highly integrated mobile device that combine the functionality of a phone with various other features including imaging capability, internet access, entertainment and etc. Modern smartphones are often equipped with high resolution complementary metal–oxide–semiconductor (CMOS) cameras, which allows the acquisition of high-resolution images and videos. Combined with mini-scale magnification setups, smartphone can be used for imaging of single cells without the need for expensive equipment[58-60]. Meanwhile, the processors built into the smartphone often have a more advanced architecture and fabrication technology than computer processor, meaning that in spite of more compact size, these smartphone processors can still produce comparable computation power. As a result, smartphone nowadays can handle very complicated and high-computation-cost tasks including sophisticated image processing, or even the training of a deep neural network[61]. Moreover, with the advances in wireless communication technology, and storage and computing capability of smartphone can be further extended with the help of cloud storage/computing. With these advantages, smartphone has become a very popular choice as a portable and low-cost platform for various biomedical researches[62]. Due to its compact size, it is often used along with microfluidic technology for POC applications.

1.4.2 Microscopic setup

As introduced in the previous section, the built-in CMOS camera can be used to acquire cellular images with the help of external lenses for magnification.

Optical magnifications are often achieved using convex lenses. As light enters a convex lens, the rays will follow the principle of refraction[63]. Refraction can be described as the bending of light as it passes from one transparent medium to another. In the case of a convex lens, the two mediums are air and lens (glass or plastics like acrylic). The principle of refraction can be understood through Snell's law, which states that the ratio of the sine of the angle of incidence (θ_1) to the sine of the angle of refraction (θ_2) is equal to the ratio of the velocities of light in the two mediums. Mathematically, it can be expressed as:

$$n_1 sin\theta_1 = n_2 sin\theta_2 \tag{1}$$

Where n_1 is the refractive index of the first medium (where the incident light is coming from), n_2 is the refractive index of the second medium (where the light is entering), θ_1 is the angle of incidence (the angle between the incident light ray and the normal to the interface between the two mediums), and θ_2 is the angle of refraction (the angle between the refracted light ray and the normal to the interface). When light travels from a medium with a lower refractive index to a medium with a higher refractive index, it slows down and bends towards the normal (an imaginary line perpendicular to the interface). This causes the light ray to change direction. Conversely, when light travels from a medium with a higher refractive index to a medium with a lower refractive index, it speeds up and bends away from the normal. The amount of bending or refraction depends on the angle of incidence and the refractive indices of the two media involved. If the angle of incidence is increased, the angle of refraction will also increase. Fig. 1A is a demonstration of the principle of refraction in a convex lens.

Following the principle of refraction, light rays can converge when they enter convex lens. As shown in Fig. 1A, when parallel rays of light are shed to the lens, they will be merged to one single point on the other side of the lens which is known as the focal point (f_0). The distance between the lens and its focal point is often referred as the focal distance. The extent of convergence/focal length is dependent on the material as well as the curvature of the lens.

A convex lens on its own can be used for magnification as shown in fig. 1B. The relationship between focal length, object distance and image distance can be expressed in the following equations:

$$\frac{1}{f} = \frac{1}{u} + \frac{1}{v} \tag{2}$$

Where f represents focal length, u represents object distance and v represents image distance. When the object distance is smaller than focal length, the image distance becomes a negative number, meaning that a virtual image is formed at the same side of the lens with the object. When the object distance is larger than the focal length, the image distance is a positive number, meaning that a real image is formed at the opposite side of the lens with the object (Fig. 1B). The magnification ratio of the single convex lens can be calculated as follow:

$$M = \frac{v}{u} = \frac{f}{|f - u|} \tag{3}$$

From this function, it can be derived that for a real-image magnification system, the object distance needs to be between f and $2f$ in order for the magnification ratio to be larger than 1. When the object is closer to the focal point, the magnification ratio becomes bigger.

To achieve a higher magnification ratio, a compound microscope design can be employed. Fig. 1C shows a two-lenses magnification system. The lens closer to the object is often referred as the objective lens and the lens closer to the eye/sensor is often referred as the eyepiece. In the system, the object is placed between f and $2f$ of the objective lens such that a real magnified image can be formed on the opposite side of the lens. The eyepiece is positioned such that the real-image from objective lens is located within the focal point of the eyepiece. As a result, a magnified virtual image can be observed by human eye, and the magnification ratio can be calculated as the multiplication of the magnification ratios of the two lenses.

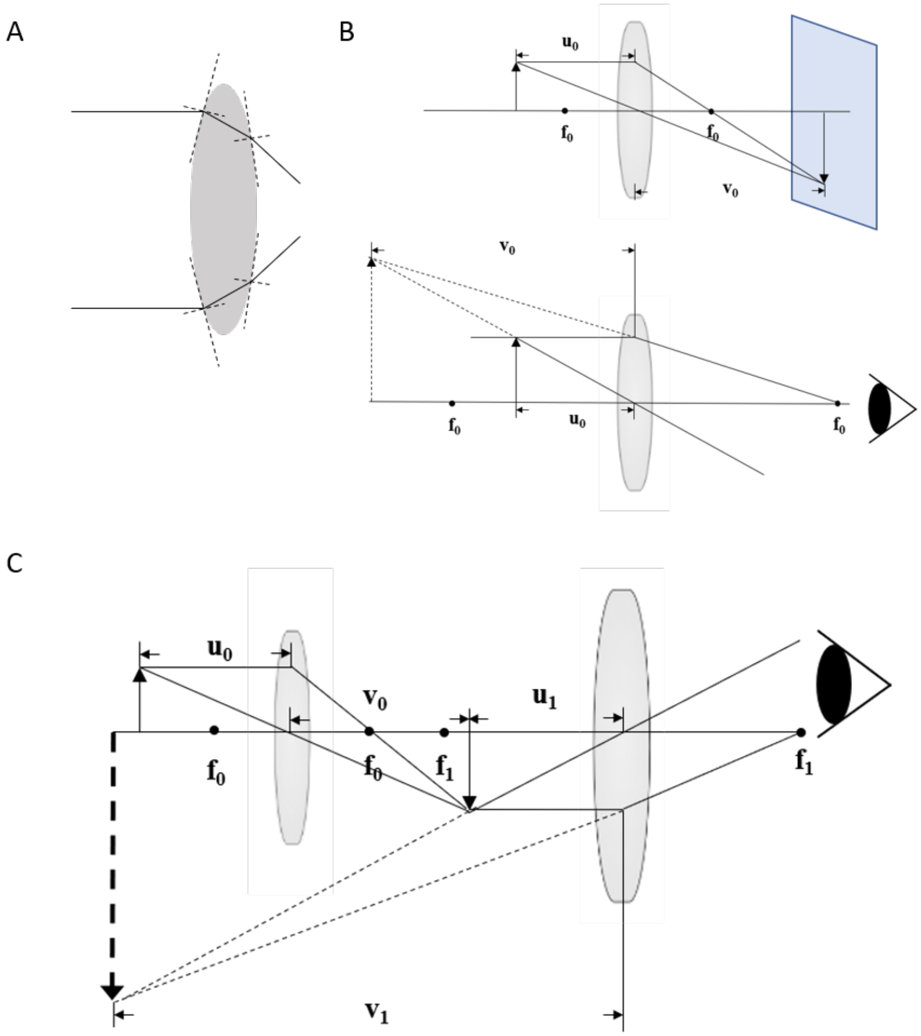

Figure 1. Working principle of microscope. **(A)** Refraction light path in a convex lens. **(B)** Working principle of single-convex-lens magnification system. **(C)** Working principle of double-convex-lens magnification system.The real-world microscope often utilizes much more complicated lens setups as compared to the ones discussed earlier. As a result, a big improvement can be made on chromatic aberration, spherical aberration, and other optical parameters to obtain higher quality images.

1.4.3 Fluorescence imaging

As mentioned in section 1.3, fluorescence probes are often used to mark islets for the monitoring of islets metabolism process.

Fluorescence is a phenomenon in which certain substances absorb light energy at a specific wavelength and re-emit it at a different wavelength. As shown in Fig. 2A, when a fluorescent molecule or fluorophore absorbs a photon, one of its electrons gets excited from its ground energy level to a higher energy level (S_0), creating an excited state (S_1). This photon's energy must match the energy difference between these two levels. After absorbing the energy, the electron stays in the excited state for a certain amount of time, during which it can lose energy in non-radiative processes. Then, the electron returns to its ground state, and releases the rest of the energy. This release of energy appears as a photon that we can detect as fluorescence. Due to the energy loss in the non-radiative processes, the energy of the emitted photon is less than the energy of the absorbed photon, and thus, causes the emitted light to have longer wavelength than the excitation light. Fig. 2B shows an example spectrum of fluorescence, where the left curve represents the spectrum of the excitation light, and the right curve represents the spectrum of the emission light[64].

The concept of fluorescence is widely applied in biomedical researches due to its high sensitivity, high specificity and etc. Other than the application mentioned in previous section, it can also be used for flow cytometry, cell sorting, immunofluorescence and etc.[65, 66].

Due to the working principle of fluorescence, the optical setup for fluorescent imaging is very different from bright field imaging. Fig. 2C is an illustration of a simple fluorescent imaging setup used for fluorescence microscope. It mainly contains three optical components, including the excitation filter, emission mirror and the dichroic mirror. In this setup, the light source is placed on the right, and the light beam first goes through the excitation filter, leaving only the excitation wavelength left in the light beam. The light is then reflected by the dichroic mirror and casted on the sample. A dichroic mirror is a specifically designed optical component that can reflect the excitation light and pass emission light. The sample excited by the excitation light will emit the emission light, which will go through the dichroic mirror, and then pass through the emission filter before entering the optical sensor[67]. With proper setup, the sensor can only sense the part of the sample that are marked with fluorescence markers.

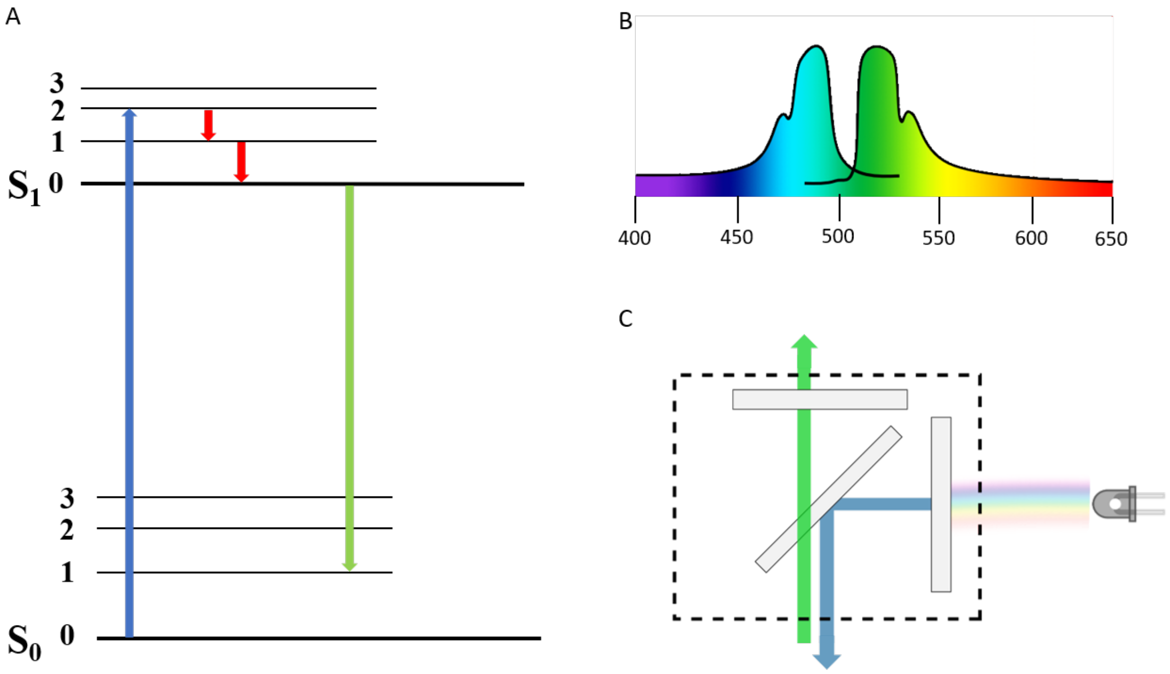

Figure 2. (A) Working principle of fluorescence. **(B)** An example spectrum of fluorescence (GFP). **(C)** Light path of a typical fluorescence microscope.

1.4.4 Digital image/video analysis

Digital image/video analysis involves implementing different mathematical, statistical tools using computer programs to understand, interpret and extract useful information from digitized images. Most of the images acquired by digital CMOS cameras are 8-bit images with three color channels. The three-color channels are Red (R), Green (G), and Blue (B). Being an 8-bit image means that the an 8-bit integer is used to represent the light intensity in each pixel for each color channels. In this work, digital image/video analysis is mainly used for cell studies. Techniques that are often used for cell image/video analysis are listed below:

1. Image filtering is an essential technique in image/video analysis. The basic idea behind image filtering is to convolve an image with a filter kernel, also known as a convolution matrix or mask. This process (2-D convolution) is to slide the filter kernel over the input image, performing element-wise multiplication between the filter values and the corresponding pixel values in the image. The resulting products are summed up, and the sum is placed in the corresponding position of the output array. This process is repeated for each position in the image until the entire image is convolved[68]. To perform the 2D

convolution operation, the filter kernel is typically smaller in size compared to the input image. One of the most widely used filters is the smoothing filter, or mean filter. A typical setup for the smoothing filter is to have all the pixels in the filter kernel to have the same value (1/size of filter), such that outcome of the convolution operation is the average of all pixel values in the neighborhood[68]. Some other filters include: a) Edge detection filter, which is a filter designed to highlight boundaries and identify edges, lines and sharp transitions in color intensity[69]. Some example edge detection filters include the Sobel filter[70], the Prewitt filter[71], and the Canny edge detector[72]. b) Frequency domain filter, which is a filter that transform images into the frequency domain using techniques such as the Fast Fourier Transform[73]. These filters are used for tasks such as denoising, image restoration, and compression. The Wiener filter[74] and the Butterworth filter[75] are examples of frequency domain filters. c) Morphological filters, which are filters based on mathematical morphology and are used for analyzing and manipulating the shape, structure, and connectivity of objects in an image. Morphological filters are based on two fundamental operations: dilation and erosion, which are operations that can expand or shrink the boundaries of regions or objects in an image[76]. Based on these two operations, other operations like opening and closing can be done to achieve more complicated operations[76]. Overall, image filtering is a fundamental technique in digital image analysis that allows for the digital image/video analysis operations as will be introduced below.

2. Feature extraction. Feature extraction is another fundamental technique in digital image analysis. The goal is to extract meaningful information about the object or features that allows further processing and analysis[77]. Some of the common features used in digital analysis include: a) Geometry related features, like area, slope, perimeter, centroid, and etc. b) Color related features, like average RGB, color histogram, mean, standard deviation and etc. Among the color features mentioned above, mean and standard deviation can be categorized into a concept called the color moment[77], where mean is the first order moment, and standard deviation is the second order moment. c) Texture. This feature refers to the visual patterns, variations, or arrangements of pixels. It is easy to be recognized by human eye and is often described suing adjectives like rough, smooth and etc. But the quantification of texture has always been a challenge. One example of textures is the Gray

Level Co-occurrence Matrices (GLCM), which is a method that captures the statistical relationships between pairs of pixels in an image. GLCM can cover the concept of entropy, contrast, correlation, energy, homogeneity and etc.[78] d) Other features. Besides the features mentioned above, there are algorithms that utilized multiple features mentioned above to recognize objects in the image with distinct features, the result of which can be used future processing steps like segmentation and classification. One example is the Scale-Invariant Feature Transform (SIFT) algorithm which is an algorithm first introduced in 1999[79]. This method can find key points (local maxima) that have distinctive and robust features, and create descriptor for each key points based on histogram of gradients orientation.

3. Image segmentation. Image segmentation is a computer vision technique that involves dividing an image into multiple regions or segments. It plays a crucial role in extracting meaningful information from images and enabling higher-level understanding and processing[80, 81]. Different techniques have been developed to deal with segmentation in different scenarios. Some examples are: a) Thresholding. This is a simple but strong technique in the scenario that light objects are placed on shady background. This technique involves selecting threshold values, and classifying the color intensity of the pixel is higher or lower based on the threshold ranges[81]. Traditionally, thresholds were chosen manually meaning that priori knowledge of the object is required for thresholding. Later on, some automatic threshold selection algorithms emerged. One example is the Otsu thresholding, which can find threshold values by minimizing the intra-class variance while maximizing the inter-class variance of pixel intensities in each class[82]. b) Edge-based method. This method functions by detecting edges or boundaries between different regions in an image. This can be achieved by detecting abrupt changes in pixel intensities, normally using the Canny edge detector or Laplacian edge detector that were mentioned earlier[81]. c) Feature-based clustering method. This is a method that group pixels together based on their similarity in features like color, texture and etc.[81] One example of clustering is the K-mean clustering, which is an unsupervised learning algorithm that can iteratively assigning data points to clusters based on the similarity (distance) in feature vectors, and updating cluster center until convergence[83]. d) Other segmentation methods. On top of the methods mentioned above, there are more advanced image segmentation techniques, which

are often used in video analysis, and can correct the segmentation result on single image based on information from multiple frames. Some examples are the inversion technique, which was designed to track muscle activities on face[80], topological alignment method, which is a method used in cell tracking based on the alignment of two consecutive frames [80].

4. Classification. Classification is a technique that refers to the process of categorizing or labeling pixels or regions within an image based on their visual characteristics or patterns. It plays a crucial role in various applications such as object recognition, scene understanding, and etc.[84] In image classification, acquired data often needs to be preprocessed before any further processing. This is normally done using the different types of digital filter as mentioned previously. One commonly used filter is the smoothing filter which can be used to remove noise[84]. Since classification method needs to assign predefined classes/categories to pixels or regions based on things like color, texture and etc., feature extraction is also a preliminary step to classification. In most cases, features extracted from the image do not all have contribution to classification, so feature selection is normally performed to select optimal features for the task to reduce computation complexity and minimize over-fitting (for supervised learning)[84]. Some examples of feature selection method include Principal Component Analysis which is a technique that seeks to find a new set of uncorrelated variables (or principal components) that can capture the maximum variance in the data[85], and Linear Discriminant Analysis which is a supervised dimensionality reduction technique that aims to find a lower-dimensional representation of the data that maximizes class separability[86]. The selected features can then be used for classification purpose. In general, classification can be categorized into unsupervised classification and supervised classification. Unsupervised classification refers to the method that does not rely on labeled training data, and can automatically group pixels or regions-based on the similarity of their features. Some examples are the k-mean clustering as introduced previously, Gaussian mixture model[87], hierarchical clustering[88] and etc. Supervised classification on the other hand, refers to models that are trained using labeled training data, where each pixel or region is manually labeled with the corresponding class. Some examples of supervised classification include decision tree[89], random forest[90], support vector machine[91] and etc.

5. Object tracking. Object tracking is a technique that refers to the process of locating a certain object and follow/track the object over time in a video sequence. This is a process requires the recognition of object in individual image frames, and find similarity in video sequences against the potential position variation, scale variation, illumination changes, texture changes, and etc. This means that feature extraction and classification of single frames are the prerequisite step for tracking. Tracking is often achieved based on the similarity of static features (color, texture, …), and the prediction from the dynamic features (velocity, acceleration, …)[92]. Some tracking algorithms examples include: a) Kalman filter, which is a widely used method predict the object's position and update it using observed measurements, incorporating both motion dynamics and measurement uncertainties[93]. b) Particle filter, which is which is an improved version of Kalman filter that that can deal with non-Gaussian noises[94]. c) Mean shift filter, which is an iterative algorithm that seeks to locate the peak of a probability distribution in a feature space[95].
6. Deep learning. Deep learning is a technique that emerge quickly in recent years due to the fast advances of computation power of computing units. Deep learning is a type of supervised learning, and is built based on the concept of neural network. It can be generally understood as a model that consists of neural network layers of different types and large amounts[96]. In most cases, deep learning method requires a large training dataset, and high computation power to function, and as a result, the technique is capable of performing all the image/video analysis tasks that are mentioned above with superior performance given appropriate structure. Some common structures in deep learning include a) convolution neural network, which is a structure based on the concept of convolution, and is often used for feature extraction in image analysis[97]. b) Recurrent neural network, which is a structure that has the capability to capture temporal dependencies and sequential patterns in data, and often used to process time-dependent data like object tracking for video analysis, natural language processing[98], or analysis of other type of time-dependent signals like the ECG signal[99], acceleration signal[100] and etc. c) Transformer, which is a structure built based on attention mechanism[101], and has shown groundbreaking performance in tasks like natural language processing as compared to Recurrent Neural Network. It is now being used to build the large generative language model and has achieved great success[102].

CHAPTER 2. A Smartphone-Fluidic Digital Imaging Analysis System for Pancreatic Islet Mass Quantification

2.1 Introduction

During islet transplantation, the isolated islets need to be inspected under a microscope prior to the transplantation procedure. The inspection often involves the assessment of islet mass and islet morphology which are keys to the outcome of islet transplantation[22, 103, 104].

2.1.1 Islet equivalent and Dithizone staining

Islet mass quantification, or islet quantity assessment mainly involves the assessment of islet size and islet purity[104]. Conventionally, size is assessed using the concept of Islet Equivalent (IEq) [105] in islet transplantation. IEq is defined as an islet with a diameter of 150 (size estimation). As shown in Fig. 3, in traditional method, IEq is assessed based on the diameter of islets[106]. Since islets are not perfectly spherical in most cases[107], the longest axis of the islets is often used to estimate the diameter of the islets. The islets are categorized into diameter of 50-100, 100-150, 150-200. 250-300, 300+ μm, and the number in each category are multiplied with corresponding multipliers (0.167, 0.667, 1.685, 3.488, 6.315 and 10.352, respectively)[106]. The sum of the multiplication is used as the IEq assessment of a batch of islets. These multipliers are obtained based on the average islets' size in each category[106]. Islet purity is often estimated by examining Dithizone (DTZ) stained islets under brightfield microscope[106]. When isolating islets from doners' pancreas, it is inevitable to have components like acinar tissues which do not have the function to secret insulin in response to glucose left in the isolated islets[106]. DTZ, as a zinc-chelating agent, can bind to the Zinc ion which is specific to islet beta cells, and display red color. The average percentage of red area can then be used as an estimation of islets purity.

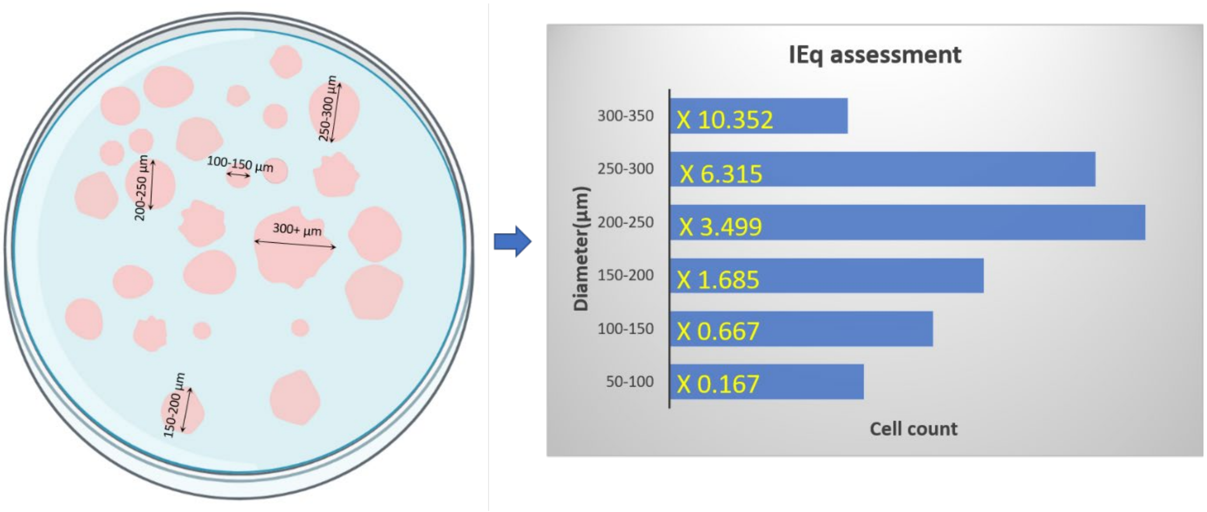

Figure 3. Demonstration of manual IEq assessment.

A multi-center study was conducted to validate the conventional manual counting procedure for quantifying isolated, dithizone-stained human islets (the IEq quantification method described in the previous paragraph) as a reliable methodology by ascertaining the accuracy, repeatability (intra-observer variability), and intermediate precision (inter-observer variability)[108]. This was done by letting 36 technicians from 8 institutions perform IEq evaluation on 2 sets of images. Each image set contained 12 photographs of DTZ stained human islets of an entire islet. On top, software-assisted analysis was performed by 3 technicians on the 2 sets of images as a comparison. The intra-observer variation was assessed by letting each technician assess each image twice and comparing the result. The inter-observer variation by comparing the results obtained by different observers using coefficient of variation (CV) (variance divided by average). On top, the average CV across different images in each dataset was also compared. The result reveals that assessment obtained by software-assisted method had significantly higher accuracy and lower inter-observer variance, intra-observer variance, and average variance across images as compared to manual islet quantification method. Given that the technicians in this study underwent professional training, this result can be worse when individuals with less experience perform the assessment.

Due to the problem of manual assessment in accuracy and consistency, researchers have started to look into the possibility of using digital imaging analysis to help with islet mass quantification.

2.1.2 Islet morphology

On top of IEq and purity, islet morphology, or more specifically, the degree of fragmentation is another parameter that is assessed during the examination of islets under microscope. In general, intact islets are preferred in islet transplantation because they maintain a more optimal distribution of different cell types (alpha cell, beta cell, and etc.). The spatial arrangement of these cells in the islet contributes to their function. If islets are fragmented, it can disrupt this optimal cell distribution, potentially affecting their ability to respond to changes in blood glucose levels. Moreover, higher fragmentation can also lead to more exposure of islet cells to the immune system, increasing the risk of immune response post-transplant[109]. In 2021, a study was conducted on establishing the relationship between islets morphology and transplantation outcomes. In the study, human islets were transplanted into diabetic mice model. Islets were assessed on their morphology prior to the transplantation, and a score was created based on parameters including shape, border, integrity, diameter and etc. The result shows that a linear relationship can be established between the morphological score and the transplantation outcome[110].

2.2 Methodology

2.2.1 Design of the Smartphone-Fluidic Digital Imaging Analysis system

2.2.1.1 Design of Image acquisition system

In the work, we built a Smartphone-Fluidic Digital Imaging Analysis (SFDIA) system for islet counting[111], which contains a smartphone, a set of detachable lenses, a LED light, and microfluidic biochips. As shown in Fig. 4, the frame was designed to hold smartphone on the top, optical pieces in the middle, and the microfluidic device at the bottom. Illumination was provided by a white diffused LED source (Adafruit Industries, New York, NY), which was placed beneath the microfluidic device to provide backlight illumination. The frame was 3D printed using MakerBot 3D printer (MakerBot® Industries, New York, NY) using Polylactic Acid (PLA) material, and had a length of 180 mm, width of 85 mm and height of 100mm.

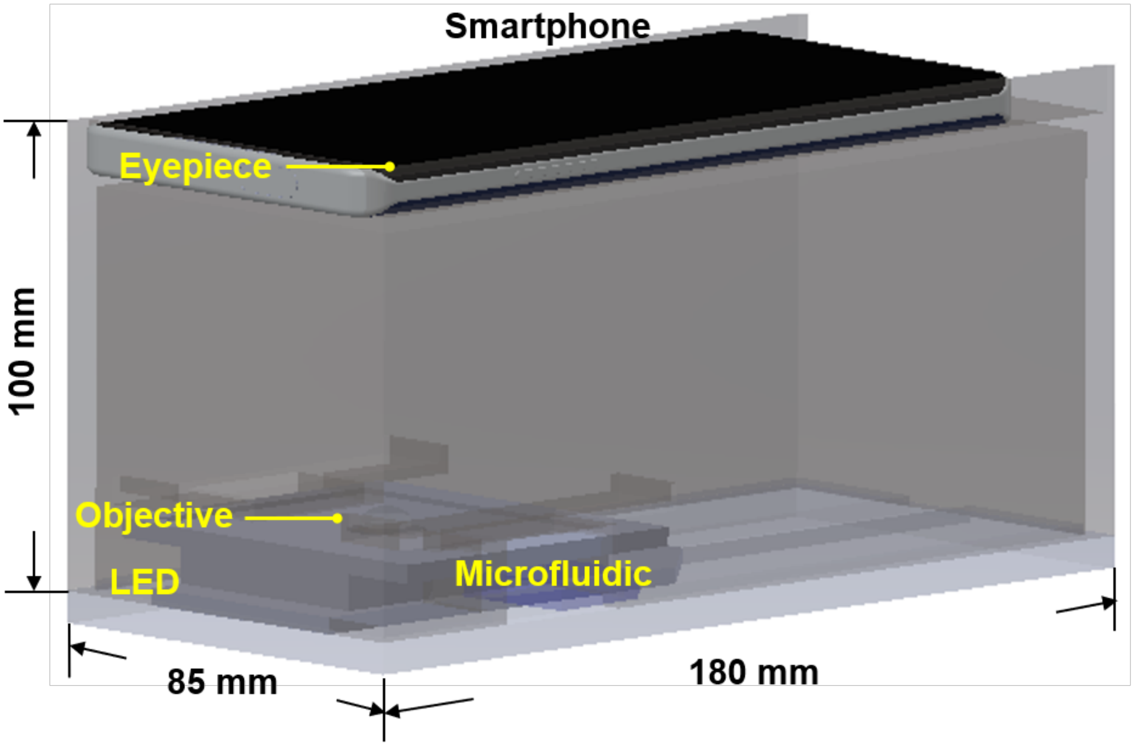

Figure 4. Design of smartphone case.

Two convex-plano lenses (Thorlabs, Newton, NJ) were used for magnification in this work. The working principle was similar to what was described in chapter 1.4.2 (Fig. 1C). In the previous description, the setup was used for a microscope, while in the smartphone system, the image needs to be captured by the smartphone camera, meaning that the image formed by the lens on the left (objective) needs to be a real image. The setup used for the smartphone system is shown in Fig. 5. The objective (lens on the left) had a focal length of 12 mm (f_0) and was placed 16 mm (u_0) to the right of the sample. In this way, a real image was formed 48 mm on the other side of the objective based on the calculation from Eq. 2. The eye piece had a focal distance of 15 mm (f_1), and was placed 68 mm above the eyepiece (20 mm above the real image generated by eye piece), which resulted in a real image generated on the other side of the eyepiece. Based on the magnification equation (Eq. 3), the magnification from the objective is ~3, and the magnification from the eyepiece is also ~3, meaning that the total magnification that the system offers is around 9.

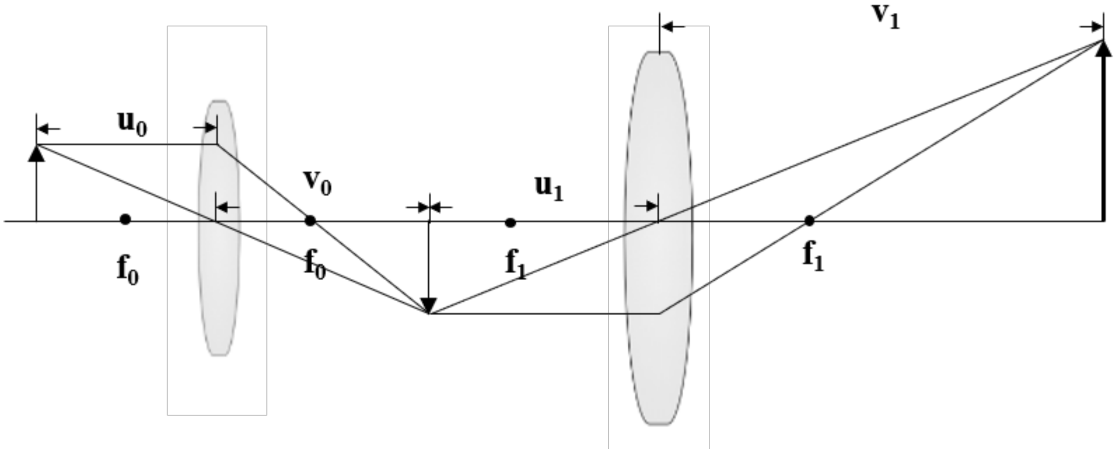

Figure 5. Demonstration of the magnification system in the smartphone-based imaging system.

2.2.1.2 Design of the microfluidic device

The microchannel (500 µm wide and 500 µm wide) was made of one layer of PDMS by soft-photolithography (which will be mentioned in detail later in the chapter) and is bonded to a glass slide[112]. The device consisted of an islet loading area with a repeated loop channel and a straight channel as a viewing area. The repeated loop channel has a total length of 700 mm and a total liquid volume of 250 µL. It is designed to preload islets and to act as a buffer zone for focusing islets in the middle of the channel, while also separating islets in distance (Fig. 6A). The straight channel is also 700 mm in length and contains a viewing area of 2 mm^2 for smartphone imaging and video recording. In the Field of View (FOV), there are two embedded scale markers of 1 mm and 0.1 mm (Fig. 6B). These markers serve as a conversion scale calibrated to equivalent pixel density. Fig. 6C shows an example image of flowing islets taken from the FOV by smartphone camera.

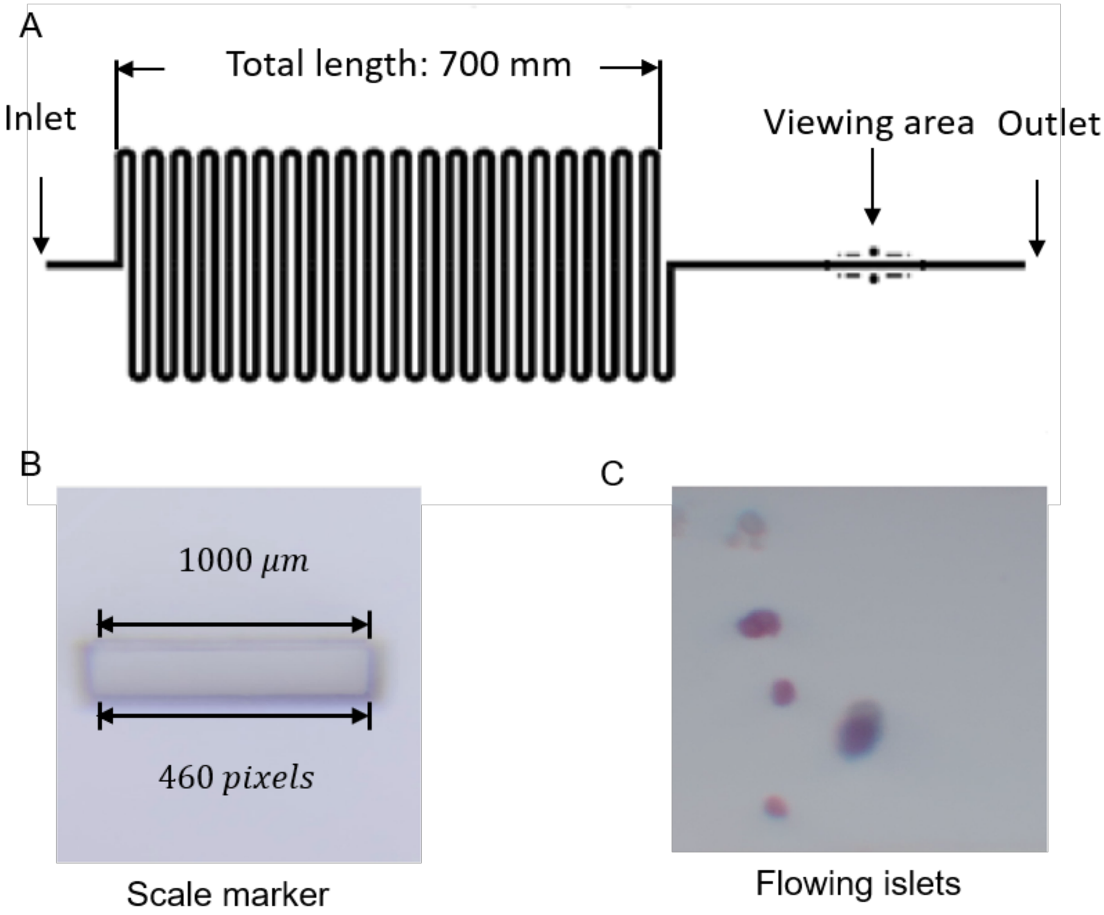

Figure 6. (A) Overall design of the micorfluidic device. **(B)** A scale marker was put into the design such that the size in pixels can be transformed into size in µm. **(C)** An example image of islets flowing through the viewing area.

2.2.1.3 Photo-lithography-fabrication of microfluidic device

The microfluidic device was fabricated using soft- photolithography protocol. The device was designed in AutoCAD within a circle of 10 cm radius. The design was printed on a transparent film (Fineline Imaging, Colorado Springs, CO) with high resolution (16000dpi). SU-8 2150 photoresist (Microchem, Wstborough, MA) was used to make the master mold for the microfluidic device. The material was pre-spun to 400 µm on top of the silicon wafers. The printed film functioned as a photomask, and was placed on top of the photoresist. The wafer was then exposed to UV light such that the transparent part of the photomask could let the UV let come through and shed on the photoresist. The SU-8 photoresist is a negative photoresist, meaning that when exposed to UV light, the material would cross-link and solidify. The uncross-linked photoresist was then washed away by cleaning the wafer with SU-8 developer solution. When designing the photomask, the features (channel, well, and etc.) were designed to be transparent, while the rest of the mask were black. As a result, the parts left on the wafer should resemble the features printed on the film. Once the SU-8 negative mold master was fabricated, devices could be made by pouring PDMS was poured on top to generate positive feature at desired thickness. The PDMS was first mixed with curing agent at a ratio of 10:1. The mixed PDMS was then poured onto the mold and placed at 80°C for 6 hours for solidification. The parts with features were then cut and peeled off from the mold. Punchers of certain sizes were used to puncture inlets and chambers on the PDMS layer. The PDMS layer were bonded to a glass slide by treating both material with oxygen plasma for 5 minutes, followed by 2hr of heating at 80 °C while pressed together with weight.

2.2.2 Video analysis algorithm

The first step in video processing is individual frame analysis. This consists of mainly two parts: cell identification and cell segmentation. The second step in video processing was to track cells between adjacent frames. The outline of the algorithm is shown in Fig. 7.

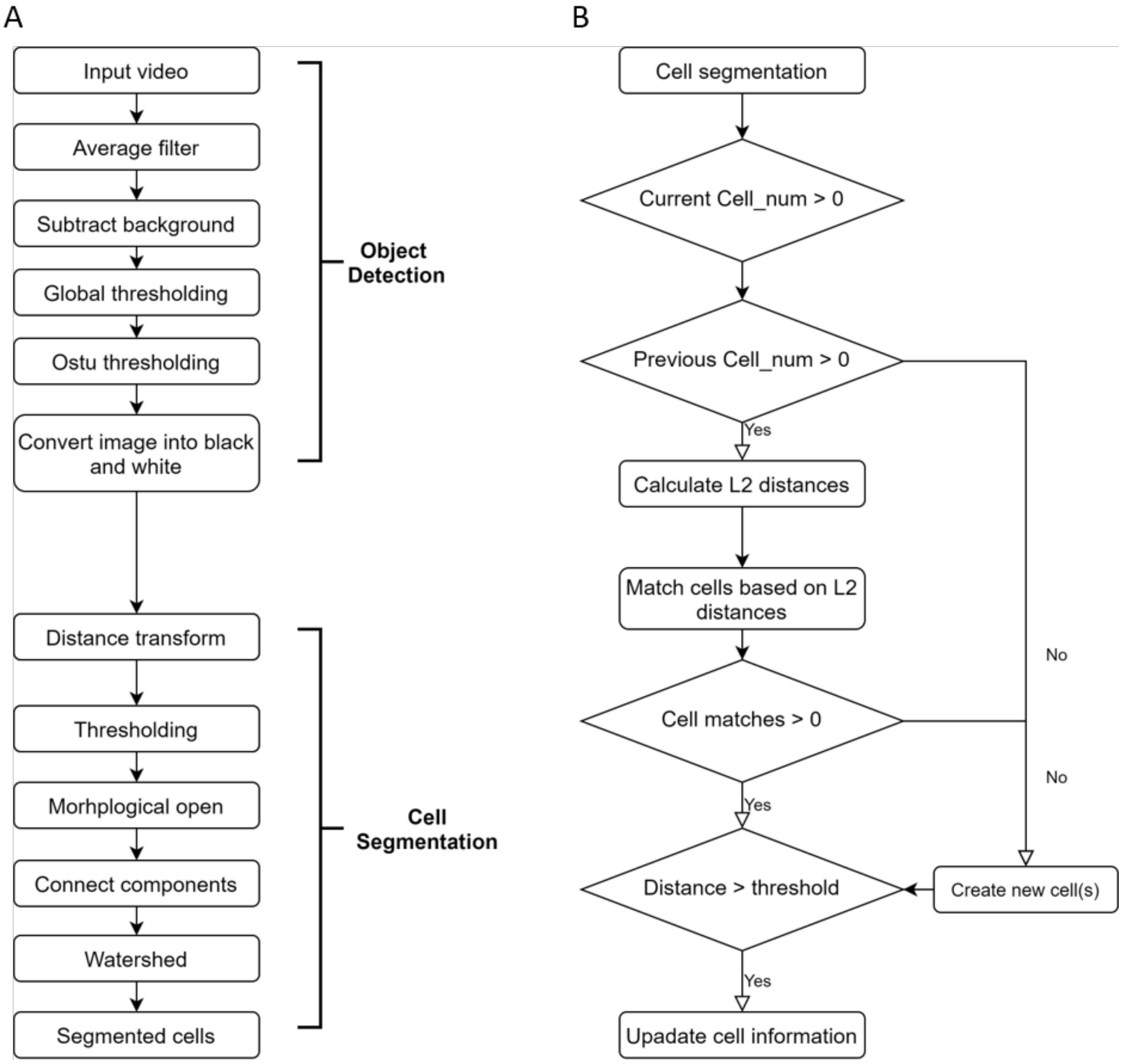

Figure 7. Flow chart of video processing algorithm. **(A)** Flow chart of the individual frame analysis. **(B)** Flow chart of cell matching algorithm.

2.2.2.1 Cell identification and segmentation

Briefly, cells are identified by setting threshold based on the differences of color intensity between cell and background in this work. As a result, when raw image data were acquired, smoothing were to be done to remove unwanted noises and prevent it from intervening with the thresholding process. Smoothing is one type of image filtering process, and it was done by convolving Gaussian filter to the image in this work. The Gaussian filter is defined as follows:

$$G(x,y) = \frac{1}{2\pi\sigma^2} e^{-\frac{x^2+y^2}{2\sigma^2}} \tag{4}$$

The expression above is an expression for a zero mean 2D gaussian distribution with variance of σ^2. x, and y represent the two dimensions of the filter. In most cases, the two dimensions of the filter have the same length, and the length is often an odd number. In this work, a gaussian filter with kernel size of 5 and variance of 1 was used, and the filter was shown below:

$$G = \frac{1}{273}\begin{vmatrix} 1 & 4 & 7 & 4 & 1 \\ 4 & 16 & 26 & 16 & 4 \\ 7 & 26 & 41 & 26 & 7 \\ 4 & 16 & 26 & 16 & 4 \\ 1 & 4 & 7 & 4 & 1 \end{vmatrix} \tag{5}$$

As mentioned earlier, the image filtering is done by implementing convolution operation. A 2D convolution is defined as below:

$$I[x,y] * k[m,n] = \sum_{y=-\infty}^{\infty} \sum_{x=-\infty}^{\infty} I[x,y] \times k[m-x, y-n] \tag{6}$$

Where I represents image and k represents kernel/filter (Gaussian filter in this case). $[x,y]$, $[m,n]$ are the coordinates for the image and the filter respectively.

Then background subtraction is done by subtracting the background image from all frames of the input video. Considering the fact that external environmental factors, such as lighting conditions, the specific microfluidic device used, etc. are consistent when videos are taken, background was considered to be stable and stationary, and thus, background subtraction is a good way to separate background from foreground. A background image was taken before cells were loaded and was smoothed by Gaussian filter before the background subtraction. Fig. 8 demonstrates background subtraction.

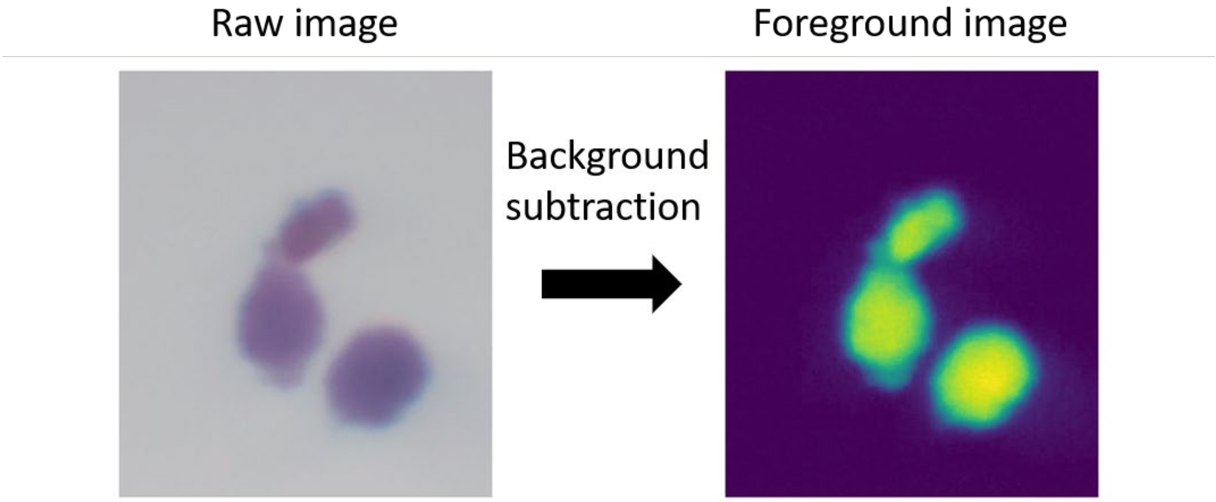

Figure 8. Demonstration of background subtraction.

The foreground is obtained by the background subtraction should contain the moving particles in the video. These moving particles contain the target cells as well as some acinar tissues that are left over from the islet isolation procedure. In general, functional islets are cell clusters with relatively large size, and thus are darker as compared to the acinar tissues. So, a global thresholding with a low threshold value was first applied to the image to filter out some of the small acinar tissues as well as some noise information. Then, Otsu thresholding was applied to narrow the selection range for the potential islets.

Otsu thresholding was an advanced method to automatically decide threshold value. Otsu's method assumes that the image contains two classes of pixels following bi-modal histogram (foreground pixels and background pixels). The method first converts the image into histogram (256-bin histogram for an 8-bit image), and calculate the cumulative probability distribution of the histogram. Then the method searches from 0 to 255 to find the exact value that minimizes the weighted-within-class variance which is given by the following equation:

$$\sigma^2{}_{sum}(t) = w_b(t)\sigma^2{}_b(t) + w_f(t)\sigma^2{}_f(t) \tag{7}$$

Where $\sigma^2{}_{sum}$, $\sigma^2{}_b$ and $\sigma^2{}_f$ represent the total variance, intra-class variance for background and intra-class variance for foreground respectively. w_b and w_f represent the weight for background and foreground respectively. t represent threshold. The weights are calculated as the cumulative sum of each class, and are represented by the function below:

$$w_b(t) = \sum_{i=0}^{t} Q[i] \tag{8}$$

$$w_f(t) = \sum_{i=t+1}^{255} Q[i] \tag{9}$$

Where $Q[i]$ represents the quantity of pixels at each bin. The variances can then be calculated as follows:

$$\sigma^2{}_b(t) = \sum_{i=0}^{t}[(i - \sum_{i=0}^{t}\frac{iQ[i]}{w_1[t]})^2\frac{Q[i]}{w_1[t]}] \tag{10}$$

$$\sigma^2{}_f(t) = \sum_{i=t+1}^{255}[(i - \sum_{i=t+1}^{255}\frac{iQ[i]}{w_1[t]})^2\frac{Q[i]}{w_1[t]}] \tag{11}$$

Fig. 9 demonstrates the Otsu thresholding:

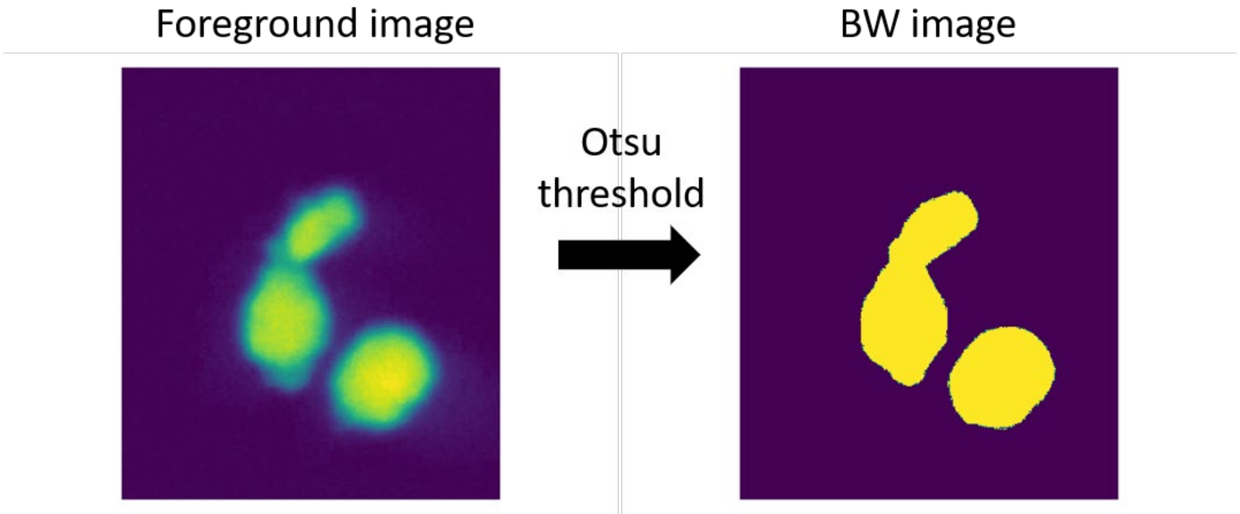

Figure 9. Demonstration of Otsu threshold.

The image was converted to black and white (BW) image after the thresholding, with black representing the background, and white representing the foreground (potential cells). The BW image was further processed with distance transform (DT). In this process, the distance between each pixel and its nearest edge was calculated. As a result, the pixels around the center of each particles had higher values while the pixels at the edge of the particles have lower values. Threshold was then applied to the transformed image, so that 'weak' connection between particles as well as particles of small sizes (which are considered to be fragments of tissues instead of islets) can be removed. This process is demonstrated by Fig. 10:

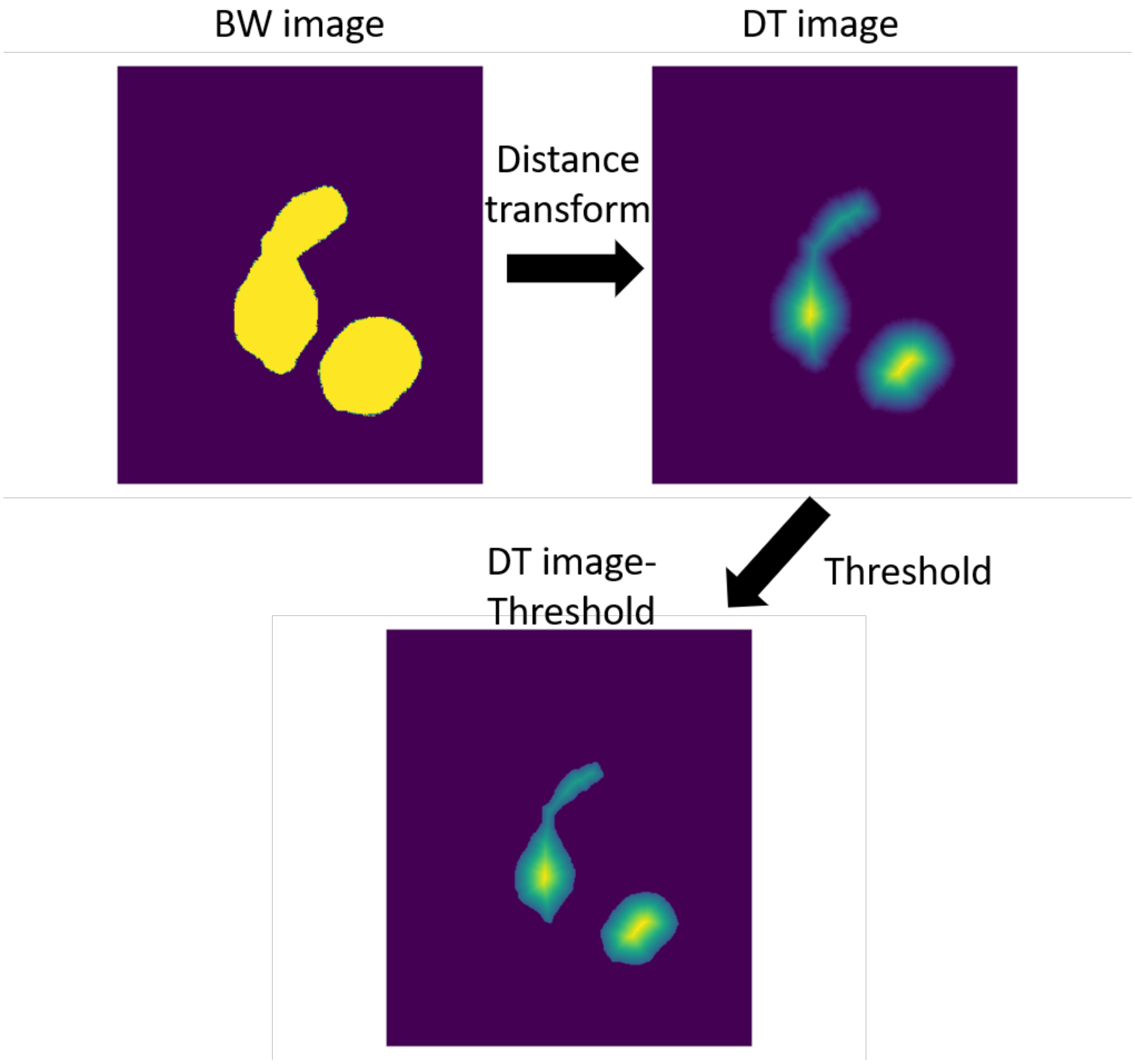

Figure 10. Demonstration of distance transform (DT). The BW image (top left) went through DT (top right) first, and then thresholding (bottom).

Morphological open was then applied to the image. Morphological open is a two-step operation that involves morphological erosion and morphological dilation. Morphological erosion is a step to 'erode' the boundary and reduce the size of an object. By doing so, the unwanted connections between cells as well as small particles can be further removed. Morphological erosion was done by convolving an ‘erosion’ kernel with the image, whose function was to set the current pixel to 1 if all the pixels under the kernel had non-zero values, and 0 otherwise. In this work, a 5 by 5 square kernel was used for the erosion operation, and the operation was repeated for 2 iterations. Morphological dilation is the opposite operation of erosion. By doing so, the objects can be expanded or ‘dilated’, such that the ‘eroded’ object can be ‘restored’ to its original size. Similar to erosion, dilation was operated by convolving a ‘dilation’ kernel with the image, whose function was to set the current pixel to 0 if all the pixels under the kernel were zero, and 1 otherwise. In this work, a 5 by 5 square kernel was used for the dilation was used and the operation was repeated for 2 iterations. Fig. 11 demonstrates the morphological open operation.

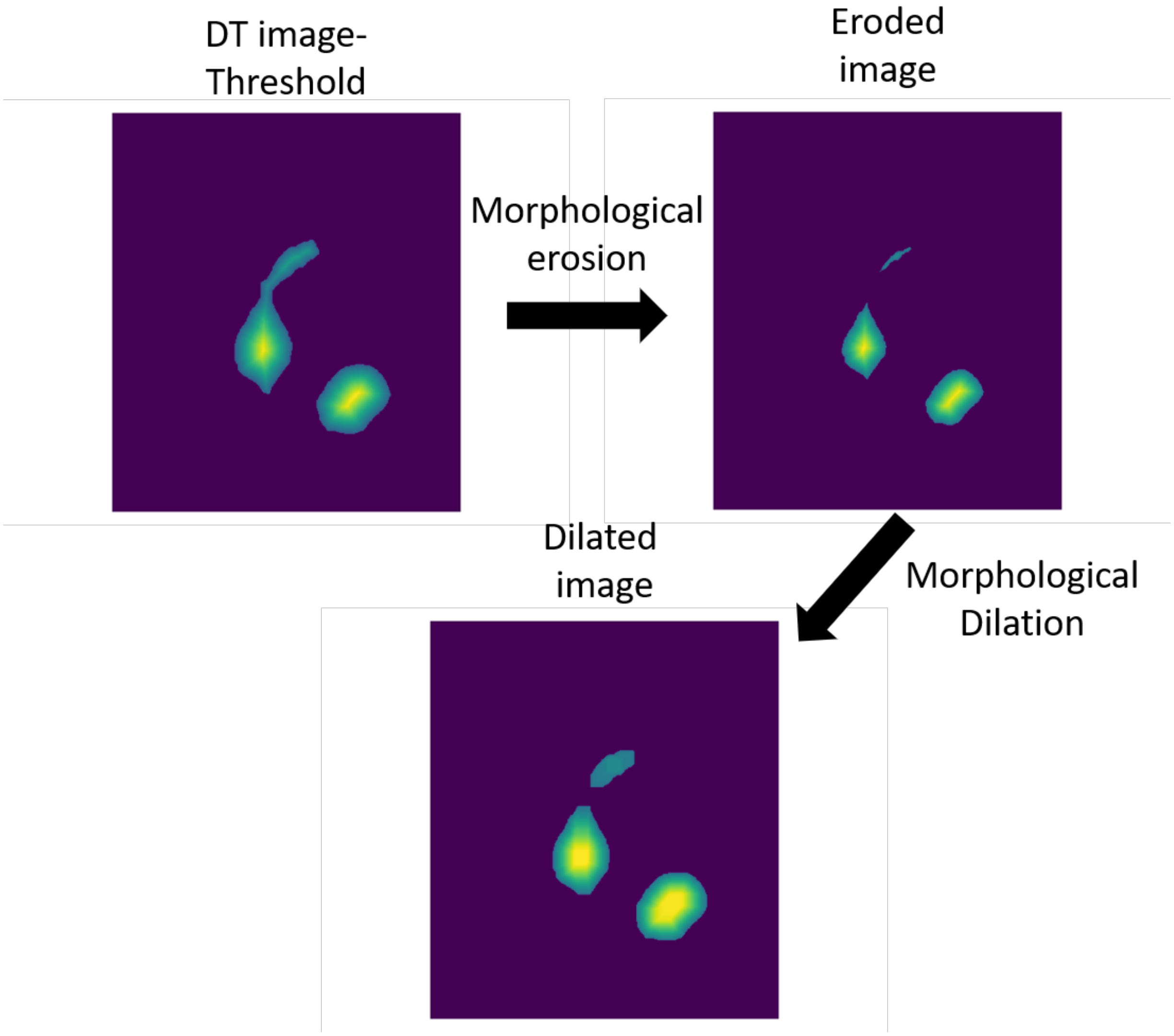

Figure 11. Demonstration of morphological operation. The DT image (top left) went through morphological erosion (top right), and then morphological dilation (bottom).

The image obtained by the morphological open process was considered to contain the centers of the cells. Finally, Watershed algorithm was applied. In this algorithm, the background from the BW image after Otsu thresholding were considered as ‘absolute background’, the cell centers from the morphological open were considered as the ‘absolute foreground’, and the rest of the pixels (unknown pixels) were grouped to the cell centers. Intuitively, this algorithm visualizes an image in terms of topography (heights and valleys), and consider the cell centers as a ‘catchment basin’ or watershed. Initially, these basins (cells centers) were filled with water, and when water started to rise, the water from different basins started to merge (in unknown pixels), and barriers/lines were created as the segmentation result. Fig. 12 demonstrates the watershed algorithm.

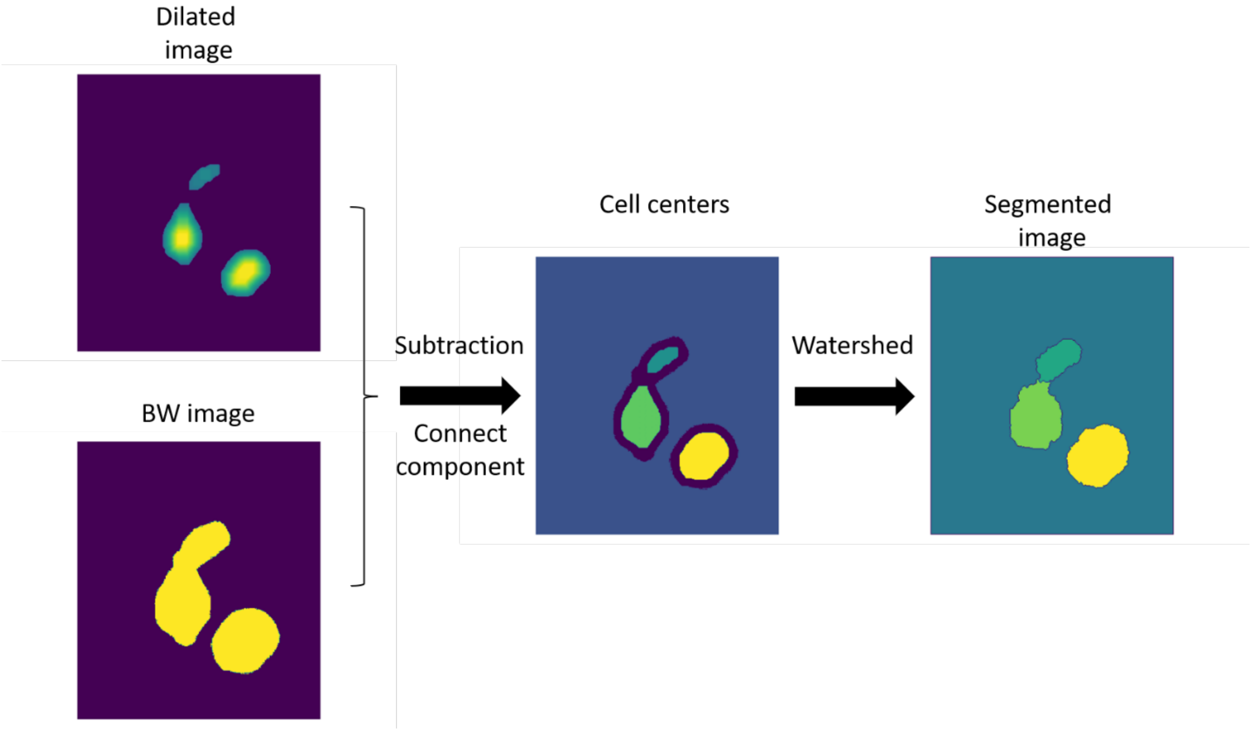

Figure 12. Demonstration of watershed algorithm. This algorithm requires both the original BW image, and the image processed by distance transform and morphological operations as input. It outputs a clustering result with each cluster representing one cell.

2.2.2.2 Cell tracking

Once the analysis of each individual frame is finished, islet matching was done make sure that every cell is counted only once. As is outlined in Fig. 7, islet tracking is done using Euclidean-distance-based approach[113]. A feature vector was formed for each detected islet. The vector includes the x-coordinate, y-coordinate, and size of the cell. Between two consecutive frames, the weighted Euclidean distance J between each cell pair is calculated using the following equation:

$$J = 1.0 \times \frac{||x_1 - x_2||_{L_2}}{min(r_1, r_2)} + 0.5 \times \frac{||y_1 - y_2 - v||_{L_2}}{min(r_1, r_2)} + 1.0 \times \frac{||a_1 - a_2||_{L_2}}{min(a_1, a_2)} \tag{11}$$

where x_1 and x_2 were the x-coordinates, y_1 and y_2 were the y-coordinates, r_1 and r_2 were the radii of the two cells, a_1 and a_2 were the areas, and v was a constant. In this matching method, cells were assumed to flow at constant velocity, which was represented by v, and v was decided by the flow rate of the liquid as well as the results from multiple trials of experiments. For each cell in the new frame, distances between the cell and all cells in the previous frame were calculated. The cells pair that have the shortest distance were matched. When the shortest distance surpassed a certain threshold, the cell was considered as a new cell. Fig. 13 demonstrates cell tracking.

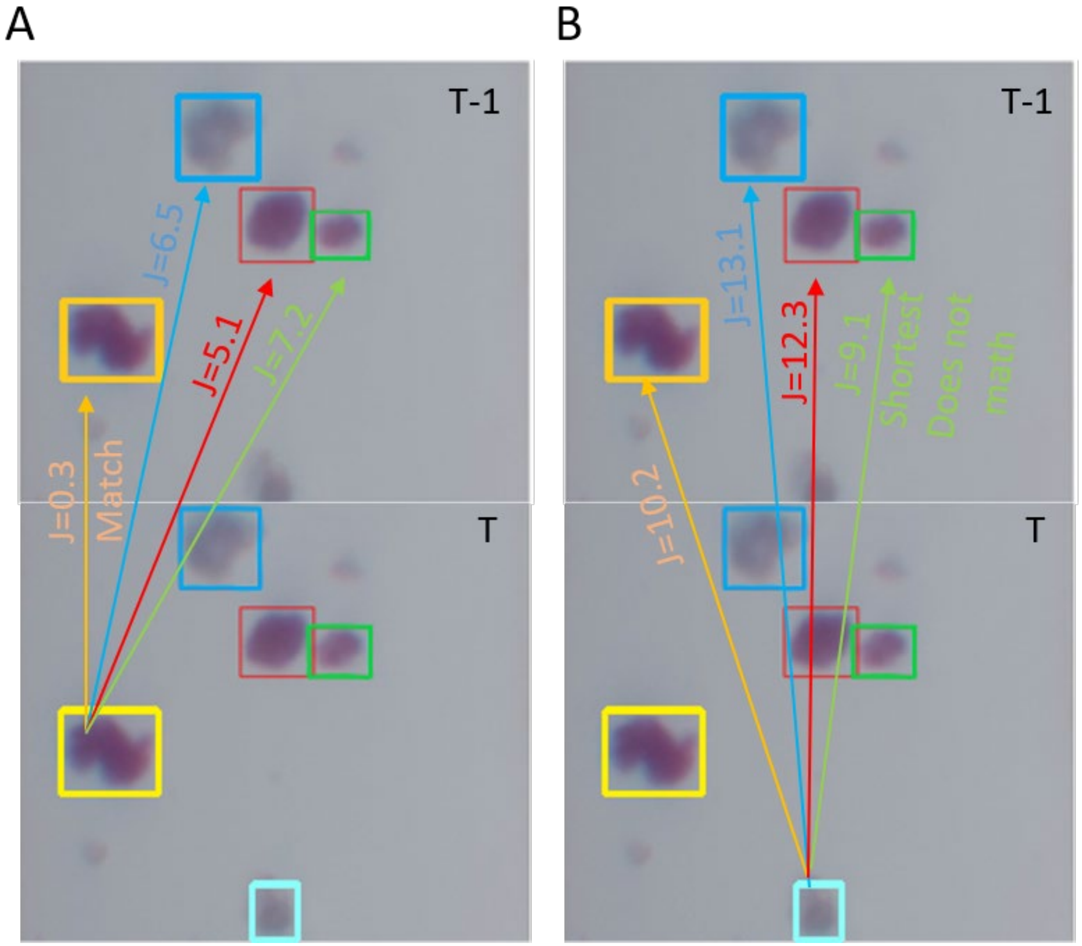

Figure 13. Demonstration of cell tracking. **(A)** Matching process demonstration of a cell that already exists in the frame at T-1. Distances between the cell in yellow rectangle in frame T and all the cells in frame T-1 were calculated. The cell pair with shortest distance (orange) matches. **(B)** Matching process demonstration of a cell that does not exist in the frame at T-1. Distances between the cell in light blue rectangle in frame T and all cells in frame T-1 were calculated. All the distances exceed a threshold. So, the cell in the light blue rectangle is new cell.

2.2.3 Feature extraction

Eventually, based on the results of the first two steps, features were extracted for analyzing mass related information.

2.2.3.1 Size, IEq and volume quantification

Equivalent spherical diameter has been widely used for size quantification of irregularly shaped particles[114]. Intuitively, it can be seen as the diameter of a perfectly circular particle that has the same area as the cell. In this study, the equivalent spherical diameter of an individual islet was defined using the following equations:

$$D_{pixel} = 2\sqrt{\frac{A_{pixel}}{\pi}} \tag{12}$$

$$D_{\mu m} = D_{pixel} \times \delta \tag{13}$$

where D_{pixel} represents the islet's equivalent diameter in pixels and A_{pixel} represents the islet's area in pixels. D_{pixel} is converted to the actual diameter measured in micrometers ($D_{\mu m}$) using a conversion factor δ, which is calculated by measuring a built-in marker (1000 µm) as is shown in Fig.6B. The calculation of δ is shown in Eq. (13). The length of the $1000\ \mu m$ marker was measured to be 460 pixels.

IEq assessment is done, as previously established, by classifying D_{pixel} into eight size ranges in µm (50-100, 101-150, 151-200, 201-250, 251-300, 301-350, 351-400, and >400). Then, IEq can be calculated by multiplying the number of islets in each group with corresponding multipliers (0.167, 0.667, 1.685, 3.499, 6.315, 10.352, 15.833, and 22.750, respectively)[106].

Under most circumstances, islets have irregular shapes. As a result, an ellipse can generally better represent the shape of an islet than a perfect circle in 2-D images[107]. Thus, volume estimation is performed based on an Ellipse-Fitting based method in this work[115]. In this method, all points on the contour of a cell were fitted to an ellipse using a least-square approximation. An ellipse can be expressed using Eq. 14:

$$\begin{gathered} F(x,y) = ax^2 + bxy + cy^2 + dx + ey + f \\ 4ac - b^2 = 1 \end{gathered} \tag{14}$$

Where (x, y) are the coordinate of the points on the ellipse, and $A = [a, b, c, d, e, f]$ is the set of parameters to be solved in order to find the best fitted ellipse. The best fitting problem can then be formulated to minimizing $||DA||^2$, with the constraint of $A^T CA = 1$. D and C are defined in Eq. (15) and Eq. (16):

$$D = \begin{bmatrix} {x_1}^2 & x_1y_1 & {y_1}^2 & x_1 & y_1 & 1 \\ {x_2}^2 & x_2y_2 & {y_1}^2 & x_2 & y_2 & 1 \\ \cdots & \cdots & \cdots & \cdots & \cdots & \cdots \\ {x_n}^2 & x_ny_n & {y_1}^2 & x_n & y_n & 1 \end{bmatrix} \tag{15}$$

$$C = \begin{bmatrix} 0 & 0 & 2 & 0 & 0 & 0 \\ 0 & -1 & 0 & 0 & 0 & 0 \\ 2 & 0 & 0 & 0 & 0 & 0 \\ 0 & 0 & 0 & 0 & 0 & 0 \\ 0 & 0 & 0 & 0 & 0 & 0 \\ 0 & 0 & 0 & 0 & 0 & 0 \end{bmatrix} \tag{16}$$

Where (x_1, y_1), (x_2, y_2), …, (x_n, y_n) represents all the points on the contour of the cell. By introducing the Lagrange multiplier λ, the problem can be transformed to solving Eq. (17):

$$D^TDA = \lambda CA \tag{17}$$

With the constraint of $A^TCA = 1$, which could be solved by finding the generalized eigen vectors. Out of the six eigen vectors, the one that corresponded to the smallest positive eigen value contained the set of parameters that defined the best fitted ellipse. This process is demonstrated in Fig. 14.

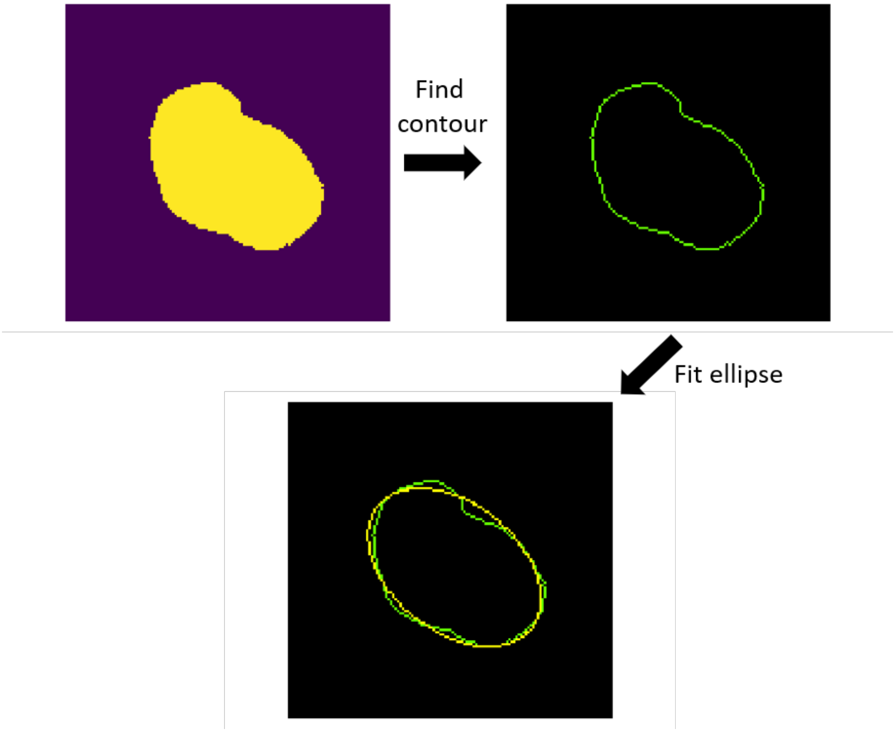

Figure 14. Demonstration of ellipse fitting.

Once the best fitted ellipse was found, the lengths of the major axis and minor axis could be obtained for each 2-D slice of each islet. One of the most common methods of converting from a 2-D to a 3-D ellipse is revolving around the minor axis and using the major axis of the 2-D ellipse as the third axis of the ellipsoid as shown in Fig. 15[107].

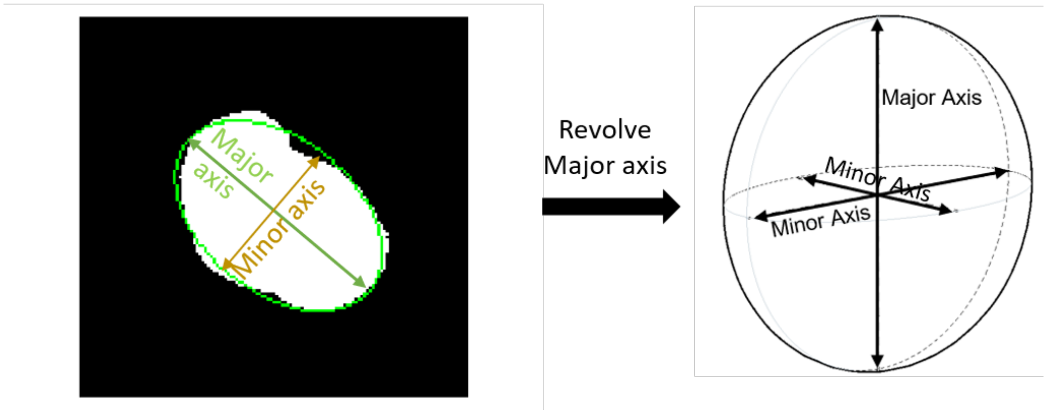

Figure 15. Demonstration of volume calculated by revolving 2D ellipse around major axis.

The volumes of islets were estimated using the following equation:

$$V_{pixel} = \frac{4}{3}\pi Ma^2 Mi \tag{17}$$

where Ma and Mi represent the long axis and short axis, respectively, of the 2-D fitted ellipse. The final volume is the average volume across each frame as is defined in the following equation:

$$\overline{V} = \frac{\sum V_{pixel}}{n} \tag{18}$$

where V_{pixel} represents the estimated volume of a cell in a single frame using pixels, and $\overline{V}_{pixel}$ represents the average estimated volume of a cell using pixels. $\overline{V}_{pixel}$ can be then converted to $\overline{V}_{\mu m^3}$ using the scaling factor δ as shown in the following equation:

$$\overline{V_{\mu m^3}} = \overline{V_{pixel}} \times \delta^3 \tag{19}$$

The Ellipsoid-Fitting-Based Volume (EFV) was compared to the volume obtained based on IEq assessment (IEqV). According to the definition of IEq, IEqV can be calculated using the following equation:

$$IEqV = IEq \times V_{150\mu m} \tag{20}$$

where IEq is the Islet Equivalent assessment obtained from the previous step, and $V_{150_{\mu m}}$ is the volume of islets with a diameter of 150 µm, which is calculated to be 1.767 x 10^6 µm^3 using the sphere volume equation.

$$V = \frac{4}{3}\pi r^3 \tag{21}$$

When estimating ellipsoid volume based on 2-D ellipse information, this work initially used Eq. (17) as discussed earlier. Yet there is another way of such estimation, which is to revolve a 2-D ellipse around its major axis, and use the minor axis as the third axis of the ellipsoid as shown in Fig. 16[116]:

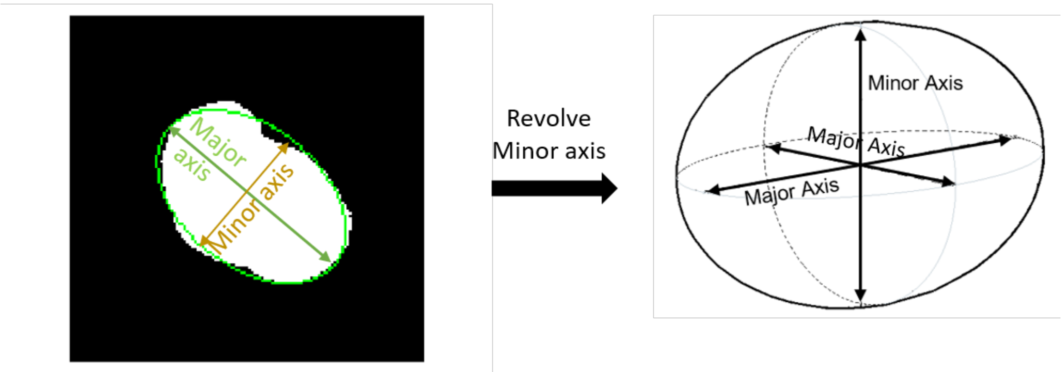

Figure 16. Demonstration of volume calculated by revolving 2D ellipse around minor axis.

The resulting equation for volume estimation is shown in Eq. (22):

$$V_{pixel} = \frac{4}{3}\pi MaMi^2 \tag{22}$$

In this work, both methods were implemented in order to see whether the choice of a different ellipsoid calculation method would have a significant impact on overall islet volume assessment.

2.2.3.2 Circularity and solidity quantification

A spherical model is generally used in the 3D representation of islets. Roundness (circularity) is used to measure the level of an islet's shape regularity [117]. Circularity is a number ranging from 0 to 1.0. Higher circularity means that the shape of the given islet is closer to a circle. In this work, average circularity was calculated using the following equations:

$$\overline{C} = \frac{\overline{A_{actual}}}{\overline{A_{estimated}}} \tag{23}$$

$$\overline{A_{estimated}} = \frac{\sum_0^n {P^2}_{actual}/(4\pi)}{n} \tag{24}$$

where $\bar{C}$ stands for average circularity, $\overline{A_{actual}}$ stands for actual islet area, $\overline{A_{estimated}}$ stands for average estimated particle area, and P_{actual} stands for actual particle perimeter. P_{actual} is obtained by counting the number of pixels on the islet's contour, which is then converted to micrometers.

In addition to circularity, we applied the concept of solidity as an indication of islet shape regularity. The solidity is defined as the ratio between the area of the actual particle and the area of the particle's convex hull:

$$Solidity = \frac{\overline{A_{convexHull}}}{\overline{A_{actual}}} \tag{25}$$

Like circularity, solidity is a number ranging from 0 to 1.0. As demonstrated in Fig. 17, the green lines represent the convex hulls of the two islets. Since both islets have an elliptical shape, they have very similar circularities; however, the islet on the left is a bit more fragmented than the one on the right, and this difference is reflected in solidity.

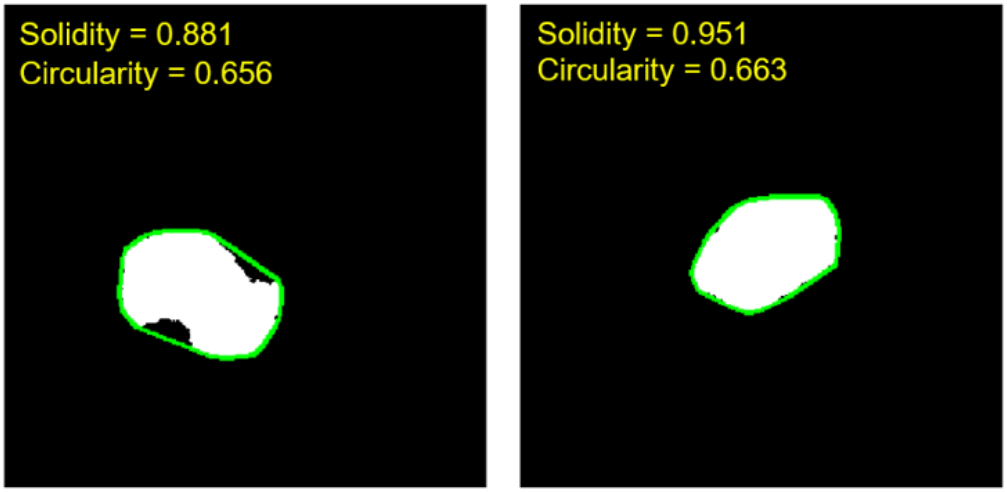

Figure 17. Demonstration of circularity and solidity calculation.

2.2.3.3 Trapped islet percentage estimation:

Trapped islet percentage is estimated using the positive area of DTZ staining of zinc in the islets and computed using Eq. (26):

$$\%DTZ^{+}ratio = \frac{Total\ dithizone\ positive\ area}{Total\ islet\ area} \tag{26}$$

The positive area normally produces a red color after DTZ staining, which can be identified based on Hue in HSV color space. In this work, pixels with Hue value between 310 to 360 (0 - 360) were identified as zinc positive areas.

Fig. 18 includes example images of trapped islets (Fig. 18A) and free islets (Fig. 18B). The images on the left were taken directly from the smartphone camera. To get better visualization, two heatmaps of HSV color space were generated. In the heatmaps, the DTZ stained areas appeared to be dark red/black, while the no-DTZ areas appeared to be bright red. The two trapped islets in Fig.5A had around 50% of the areas stained with DTZ, while the free islets in Fig.5B were almost completely stained with DTZ. The DTZ positive ratio of the two trapped islets were calculated to be 67.31% and 66.73%, and the ratio of the free islets was calculated to be 99.05%.

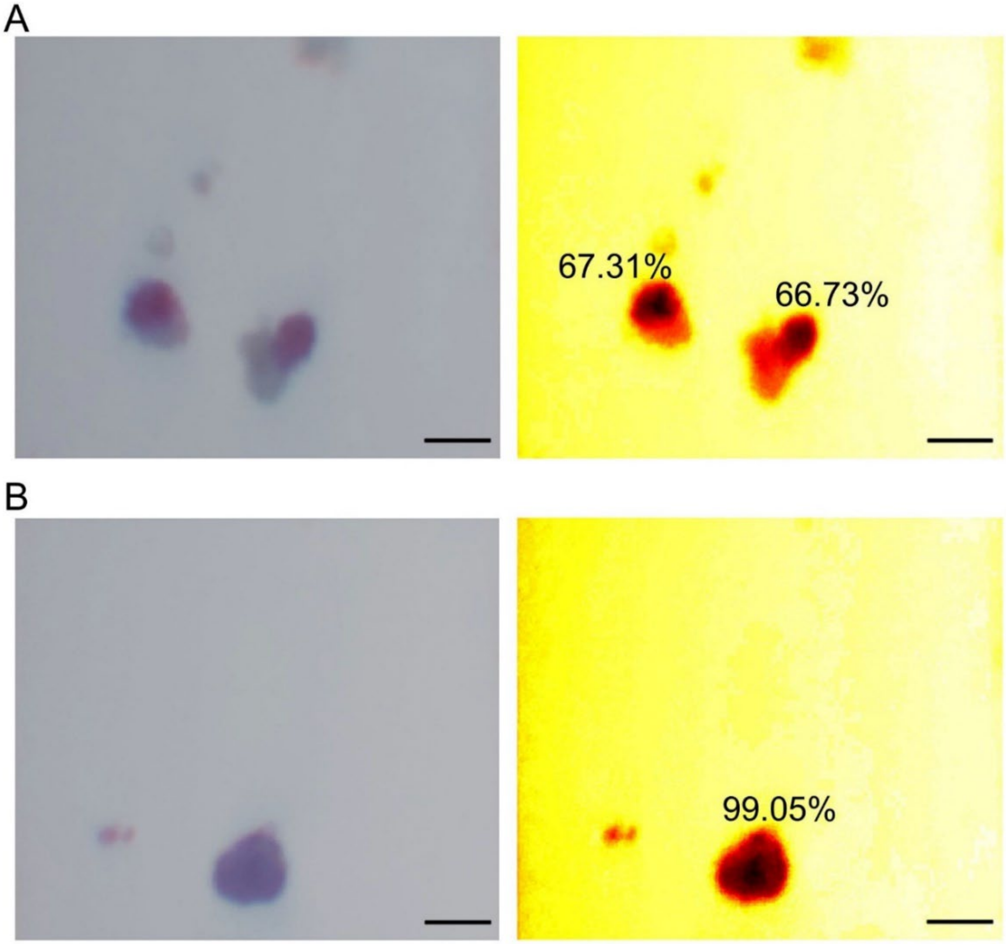

Figure 18. Demonstration of islet purity (trapped islet percentage) calculation. **(A)** Two islets trapped in aciner tissue, with purity of 67.31% and 66.73% respectively. **(B)** A free islet with purity of 99.05%.

2.2.4 Human islets preparation and manual mass quantification

Human islets were isolated according to the published protocol[118, 119]. In brief, a cadaver pancreas was obtained from organ procurement organizations (OPO) and islets were isolated at University of Virginia with donors' consent for research. The pancreas was trimmed and distended with Liberase HI (Roche Applied Science, Penzberg, Upper Bavaria, Bermany) and digested in a Ricordi chamber. The digested tissues were then purified by a continuous UIC-UB gradient protocol on a cell separator (Cobe 2991, Cobe Inc., CO) and then cultured in CMRL 1066 media with 5% human albumin (CSL Behring, King of Prussia, PA) at 37°C under 5% CO_2.

15 mM Dithizone solution (Sigma-Aldrich, St. Louis, MO) was used to differentiate islets and acinar tissues by staining the zinc ion highly concentrated in beta-cells[106]. Tissues were incubated at 37°C for 10 min and then washed twice with Phosphate-buffered saline (PBS). Manual assessment of human islets was done under microscope in a Peri dish with scales. Diameters of islets were estimated by comparing to the scales. These diameters were used to classify islets into eight size ranges as described earlier and then converted into IEq by the corresponding multipliers.

2.2.4.1 Human islets loading and video recording on-chip

The counting samples of isolated human islets were picked up manually and randomly via polyethylene tubing (PE160, Intramedic, Sollentuna, Stockholms Lan, Sweden) connected to a 1 mL syringe. The tubing was then connected to the inlet of the microfluidic channel. The islets were injected into the device via PHD ULTRA™ Syringe Pump (Harvard Apparatus, Holliston, MA) at a flow rate of 20-30 µL/min.

The captured videos (1920 x 1080; 1080p, 60fps) were recorded in .mp4 file format and then transferred to a computer for further video processing. The video processing algorithm was developed using python 3.8.1 within Spyder IDE (version 3.36). The video analysis was assembled for five functions: object detection, cell segmentation, cell tracking, feature extraction, and report generation. Fig. 2 summarizes the procedures of object detection, cell segmentation, and cell tracking.

2.3 Results and discussion

2.3.1 Human islet quantification

In the current practice of human islets isolation, about 500 µL of cell suspension, which normally contains 0.05% to 0.1% of the total islet population, is picked up manually, randomly, and repeatedly for islet mass quantification.[118, 119] Therefore, the randomness of sample size often brings variation to the results of assessments. In this study, human islet samples with different islet masses were quantified by both manual counting and the SFDIA system for comparison. Experimental results of six groups of samples, with islet number within each sample ranging from 20 to 200, were plotted as shown in Fig. 19. Across the six groups of data, the average difference between the SFDIA system and manual counting was 2.91% ± 1.50%, and the p-value for all six groups are greater than 0.05, indicating that there is no significant difference between the result generated by manual counting and SFDIA system. This means the SFDIA system is able to give accurate quantification assessments close to manual counting regardless of islet sample sizes. Additionally, manual counting showed a relatively high variation (SD = 3.1 - 5.0), while the SFDIA system was able to give consistently low variation (SD < 1). In general, for traditional manual counting, smaller sample size creates larger error in the results. The consistency of the SFDIA system successfully reduced human error and rendered the assessment results more reliable than the traditional manual counting method.

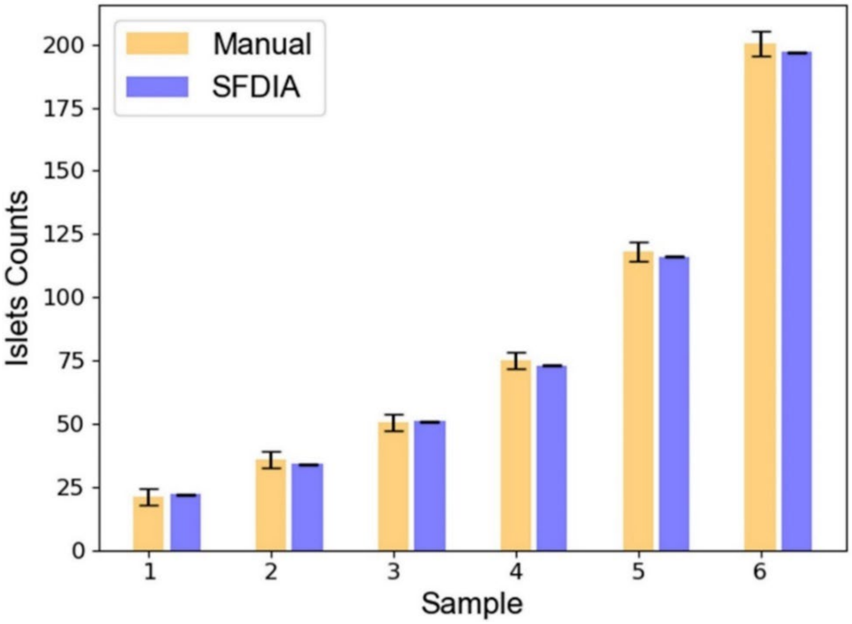

Figure 19. Comprison between manuual counting and smartphone-based counting. Six human islets samples of varied sample sizes were assessed by both manual counting and the smartphone-based system.

2.3.2 Islet size estimation

As discussed in earlier chapter, islet size is a decisive factor that contributes to the quantification of islet mass in addition to islet number. Equivalent diameters have been the most widely used parameter to represent islet size. On top, volume was also used to estimate islet size in this work.

2.3.2.1 Estimation of equivalent diameters

Since pancreatic islets do not have a perfect regular shape, islet diameters were estimated as the equivalent diameter calculated based on islet area from each frame of the recorded video. Distribution of human islet diameters are plotted in Fig. 20.

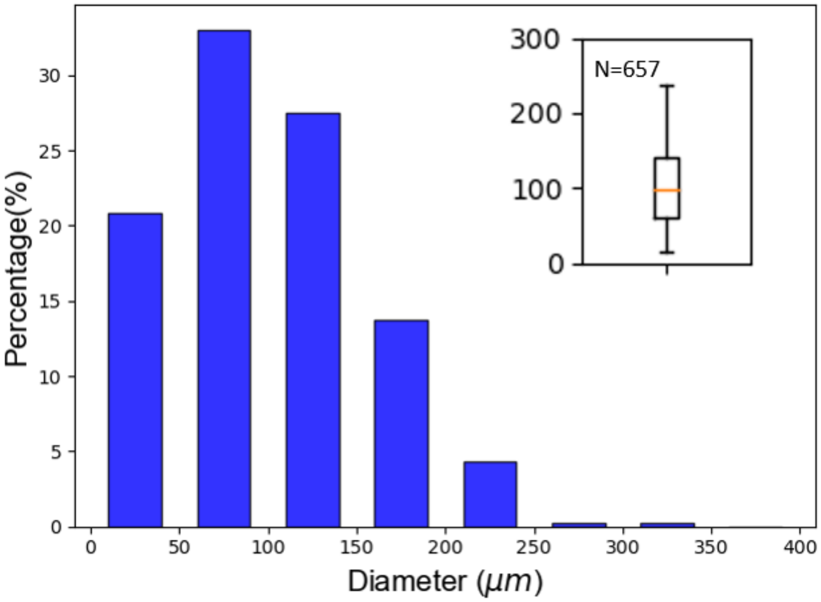

Figure 20. Distribution of islet diameter. The mean diameter of the islet sample is 99.87 ± 53.91 µm.

As shown in the figure, the islet samples we tested had an average diameter of 99.88 ± 53.91 µm and a maximum of 337.67 µm. The majority of the islets (> 60% of the population) had diameters between 50 µm and 150 µm. The diameter obtained by the SFDIA system is the equivalent diameter calculated from islet area, while manual assessments often use the length of the major axis as the diameter. As a result, the diameter obtained by the SFDIA system can be slightly smaller but more reliable than that estimated by manual assessment.

2.3.2.2 Estimation of volume

As mentioned in earlier chapter, the volume estimation in this work was done using ellipsoid-fitting-based estimation method. This volume (EFV) was compared to the volume obtained using IEq estimation method (IEqV). The result is plotted in Fig. 21:

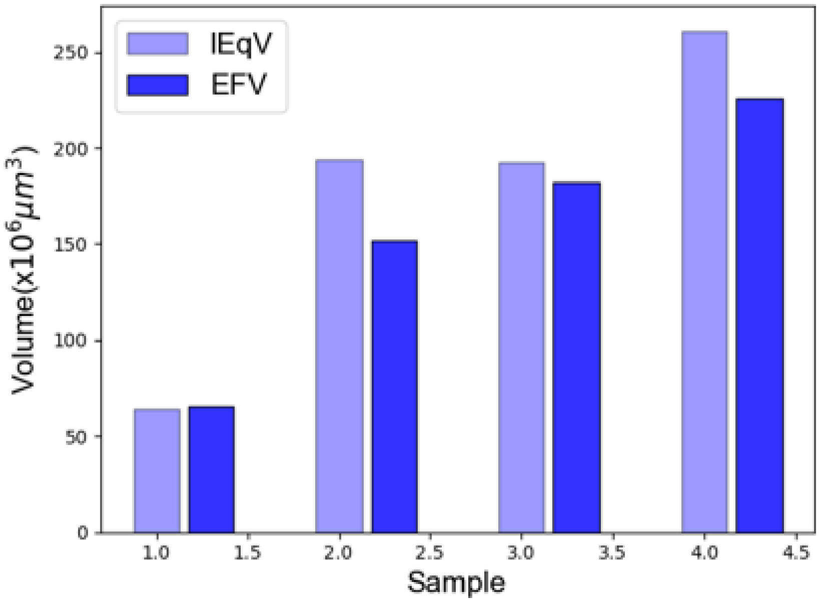

Figure 21. Comparison between volume calculated from traditional IEq assessment method (IEqV) and the one obtained from smartphone system (EFV).

As shown in the figure, in samples, sample 3 and sample 4, IEqV was higher than EFV, while in sample 1, the two had similar values. Meanwhile, it is worth noticing that sample 2 and sample 3 had very similar IEqV's while there was a notable difference between their EFV's. These differences are likely to be caused by the way IEqV is calculated, where islets are first grouped by their diameter, and then the number of islets within each group is multiplied by the IEq conversion factor. On one hand, IEq estimation was done based on the islets' longer axis, meaning that the estimation result tends to be higher than the actual size. This explains that the fact that IEqV tends to be higher than EFV. On the other hand, it is worth noticing that sample 2 and sample 3 had very similar IEqV's while there was a notable difference between their EFV's. This is mainly caused by the way IEqV is calculated, wherein islets are first grouped by their diameter, and then the number of islets within each group is multiplied by the IEq conversion factor. As a result, IEqV tends to ignore small size variation and causes error.

2.3.2.3 Comparison of two volume estimation methods

As discussed in the earlier chapter, two methods of islet volume estimation were utilized for comparison: V_{major} used the major axis as the third axis of the ellipse, while V_{minor} used the minor axis as the third axis. The comparison between the two calculation methods was shown in Fig. 22.

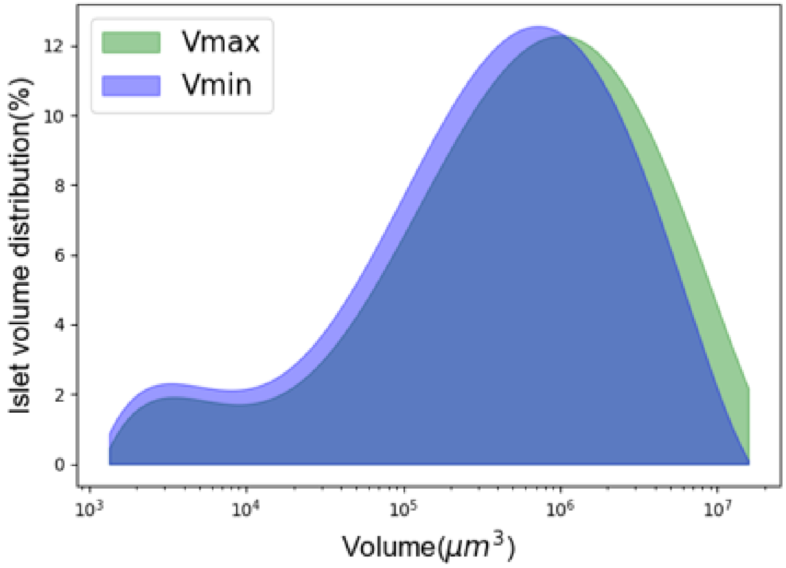

Figure 22. Distribution curves of volume calculated from two different methods (revolving 2D ellipse around major axis and minor axis).

As shown, the curve of V_{major} was slightly to the right of V_{mionr} as expected. However, the two curves largely overlapped, indicating that the two methods generated similar results in terms of islet volume estimation. The result from this experiment demonstrates that the choice of the third axis does not significantly affect the overall islet volume estimation using the ellipsoid fitting model. The islet volume estimation from our system can potentially be a better representation of actual islet volume than traditional IEq-derived islet volume and thus provides more detailed information to clinicians when preparing for islet transplants.

2.3.3 Islet morphology estimation

Islet fragmentation is often caused by chemical and mechanical stress during islet isolation and post-isolation culture[109]. This is a key parameter in evaluation of islet quality and has also been considered as an important factor in post-transplant graft survival rates. Therefore, the accurate assessment of human islet fragmentation prior to transplantation is important for improving clinical outcomes. The concept of circularity has been widely used as a measurement of islet fragmentation in islet assessments[117]. An ellipse/ellipsoid model is considered to be a better estimation of islet size and volume than a circular model, since circularity alone may not be enough to quantify shape regularity. In this study, two different parameters, circularity and solidity, were calculated to describe islet morphological features. Fig. 23 shows the result for circularity estimation.

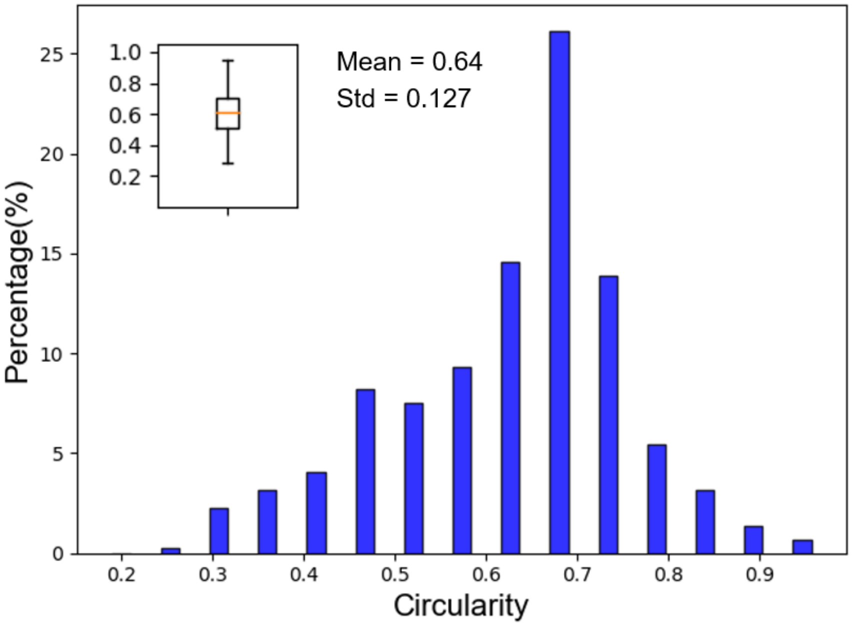

Figure 23. Islets circularity distribution. The islet sample has an average circularity of 0.591 ± 0.127.

As shown in the figure, the human islet samples had an average circularity of 0.4 with a standard deviation of 0.127. The distribution of the circularity is slightly left skewed, with the majority of islets (~83% of total islets located in the range of 0.4 to 0.7. the majority of islets (~83% of total islets) presented a circularity range of 0.4 to 0.7. Fig. 24 shows the result for solidity estimation.

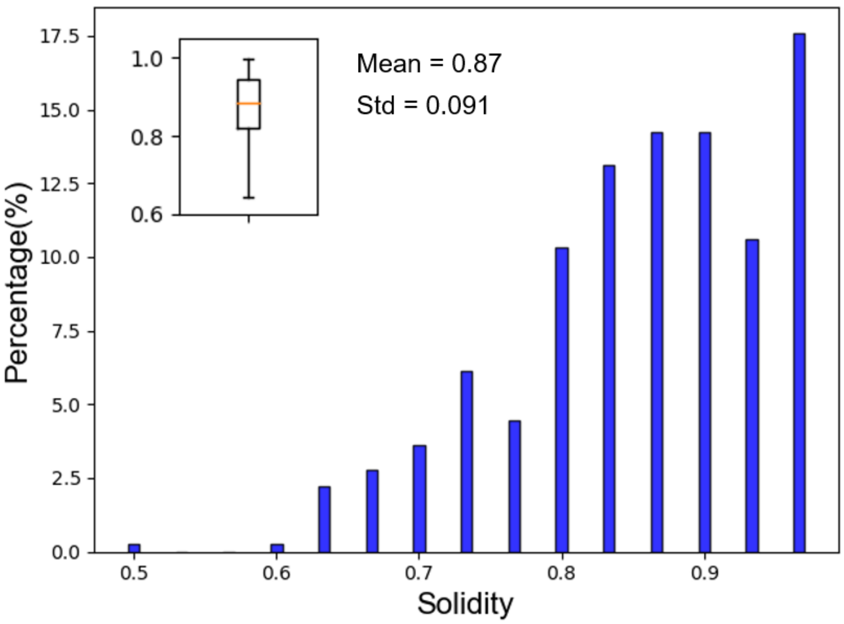

Figure 24. Islets solidity distribution. The islet sample has an average solidity of 0.853 ± 0.107.

As shown in the figure, the solidity of the human islet samples had an average of 0.87 with a standard deviation of 0.091. The distribution of the solidity is extremely left skewed, with the majority of islets (~70% of total islets) located in the range of 0.8 to 1. The high solidity values among our islet samples demonstrate that very few of the islets in this preparation were fragmented. These results indicate that the shapes of most islets in our samples are closer to ellipses rather than perfect circles, implying that islet solidity can be used as an improved quantification method for describing islet morphology (roundness, shape, and fragmentation).

2.3.4 Islet purity estimation

Despite the recent progress made in the field of human islet transplantation as a treatment of T1D, low purity of islet products is still a major issue affecting the success rate of islet transplantation. The degree of competition for oxygen and other nutrients between islet and non-islet tissues within transplanted allografts is determined by the islet cell percentage. The conventional method to estimate the purity of isolated islets was done by DTZ staining and manually counting DTZ-positive islets under a light microscope. The operator-dependent nature of this process and the use of islet count as a unit can lead to significant overestimation of purity at the end of the procedure[120, 121]. The software we developed automatically analyzed the trapped islet percentage based on area data acquired from image processing, which provided a more accurate estimation of the purity of islet products in islet preparation.

In this work, we had two groups of islets, middle-layer and top-layer human islets, for the assessment of islet purity. In general, islets isolated from the top layer have less acinar tissues that the ones from middle layer. As a result, they usually vary significantly on both morphology and tissue composition. Fig. 25 shows the estimation result of purity as well as circularity and solidity of the middle-layer islet samples.

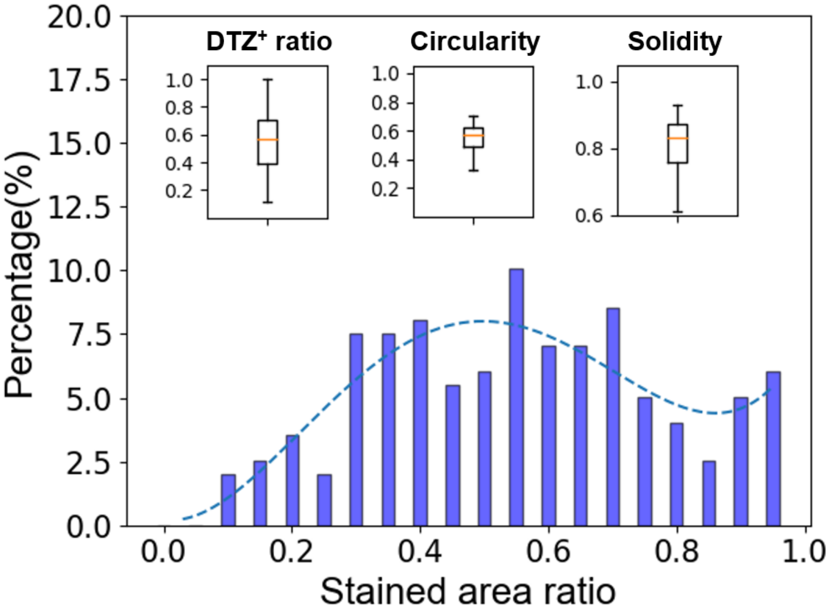

Figure 25. Trapped islet percentage and morphology assessment of islets from middle layer. The islet sample has an average DTZ$^+$ ratio of 0.576 ± 0.223, average circularity of 0.534 ± 0.102, and average solidity of 0.793 ± 0.102.

As shown, the average circularity of the sample was 0.53 with a standard deviation of 0.102. The average solidity was 0.79 with a standard deviation of 0.102. The average purity of the middle-layer islet sample was 0.576 with a standard deviation of 0.223. The distribution to purity was slightly left skewed distribution, The distribution curve was skewed to the left, with ~72% of total islets having purity between 0.3 and 0.7. Fig. 26 shows the estimation result of purity as well as circularity and solidity of the top-layer islet samples.

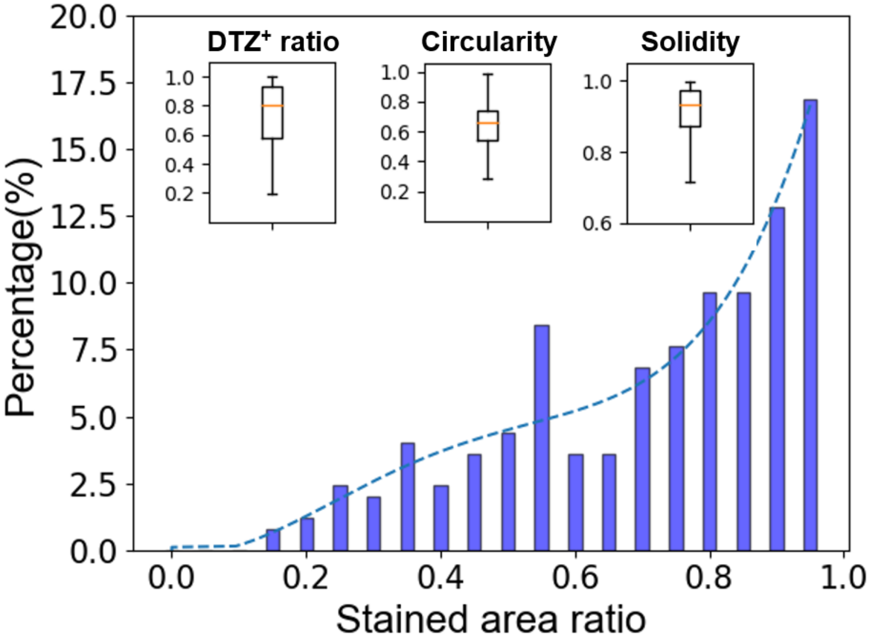

Figure 26. Trapped islet percentage and morphology assessment of islets from top layer. The islet sample has an average DTZ^+ ratio of 0.735 ± 0.213, average circularity of 0.635 ± 0.139, and average solidity of 0.853 ± 0.107.

As shown, the average circularity of the sample was 0.64 with a standard deviation of 0.139. The average solidity was 0.85 with a standard deviation of 0.107. The average purity of the middle-layer islet sample was 0.735 with a standard deviation of 0.213. The distribution to the purity was extremely left skewed, with the majority purity (~67% of total islets) above 0.7. When comparing the islets from the two preparations, it's obvious that the top-layer islets had higher purity and were less fragmented in morphology. With that said, with our video processing program, we not only obtained results consistent with typical expectations from human islet preparation, but were also able to provide more detailed and reliable information on islet quality (useful to clinicians) than purity estimations from standard manual quantification.

2.3.5 Conclusion

In this project, we developed a novel and dynamic smartphone-based digital imaging system integrated with microfluidic technology for pancreatic islet mass quantification. The software program provides the capability to track multiple moving islets, and separate closely attached islets. Our SFDIA system generated little variances during the counting process across multiple experiments, showing that it has advantages in consistency as compared to conventional manual counting method. In addition, the system was able to estimate size using ellipsoid model, and return additional islet parameters including volume, circularity, solidity, and trapped islet percentage, which are impossible to be directly obtained using conventional method. Using our low-cost and portable system, reliable islet parameters can be easily obtained during the preparation of islet biologics.

CHAPTER 3. Smartphone-Fluidic Fluorescence Imaging System for Studying Islet Physiology

3.1 Introduction

The smartphone system that incorporates the function of a brightfield microscope can acquire information on islet mass and islet morphology. However, the islet morphology can only provide a rough estimate of islet function. To gain more precise quantification on islet function, analysis on the islet metabolism procedure is required.

3.1.1 Islet metabolism

The islet function is often determined by its capability to secrete insulin in response to glucose. The metabolism process of glucose is shown in Fig. 27 [122]. The pancreatic islets, specifically the beta cells, first take up glucose from the bloodstream. Glucose is taken into these cells through a type of protein in the cell membrane called a glucose transporter. When glucose enters the cell, it first goes through the glycolysis process, which occurs in the cytoplasm of cells. This process breaks down one molecule of glucose (which has six carbons) into two molecules of pyruvate (each with three carbons). During this process, two molecules of ATP are used, but four molecules are produced, resulting in a net gain of two ATP molecules. Additionally, two molecules of NAD+ are reduced to NADH. Once glycolysis is complete, the two pyruvate molecules are transported into the mitochondria, where they each undergo a process called decarboxylation. In this process, one carbon is removed from each pyruvate molecule in the form of carbon dioxide, and the remaining two-carbon compound is combined with Coenzyme A to form acetyl-CoA. This process also produces one NADH molecule for each pyruvate. The next step is the Krebs Cycle, also known as the Citric Acid Cycle. Each acetyl-CoA enters this cycle, where it is further broken down, releasing more carbon dioxide and transferring electrons to carrier molecules, NAD+ and FAD, forming NADH and FADH2, respectively. For each glucose molecule, the Krebs cycle spins twice (once for each acetyl-CoA) and generates 2 ATP molecules, 6 NADH molecules, and 2 FADH2 molecules. Finally, NADH and FADH2 carry electrons to the electron transport chain in the inner mitochondrial membrane. These electrons are passed through a series of proteins, which pump hydrogen ions into the intermembrane space, creating a gradient. This gradient is then used to produce ATP in a process called oxidative phosphorylation. Oxygen is the final electron acceptor in this chain and combines with electrons and hydrogen ions to form water. The exact number of ATP molecules produced in this step can vary, but it is typically estimated to be about 32 to 34 ATP molecules per glucose molecule. When the resulting ATP is released from the mitochondria due to the metabolism process, increase in the ATP/ADP ratio within the cell leads to the closure of ATP-sensitive potassium channels (K_{ATP}) present on the cell membrane. When these channels are open, potassium ions leak out of the cell, maintaining a negative resting membrane potential. However, when they close due to high ATP levels, potassium ions can no longer leave the cell, which alters the cell's membrane potential, causing it to become more positive (depolarization). The depolarization of the cell membrane triggers the opening of voltage-dependent calcium channels (VDCC). This means that the channels open in response to the change in electrical charge across the cell membrane. When these channels open, calcium ions rush into the cell. The influx of calcium ions then triggers the exocytosis (release) of insulin-containing vesicles. Insulin is stored in these vesicles within the cell, and when the vesicles fuse with the cell membrane, insulin is released into the bloodstream.

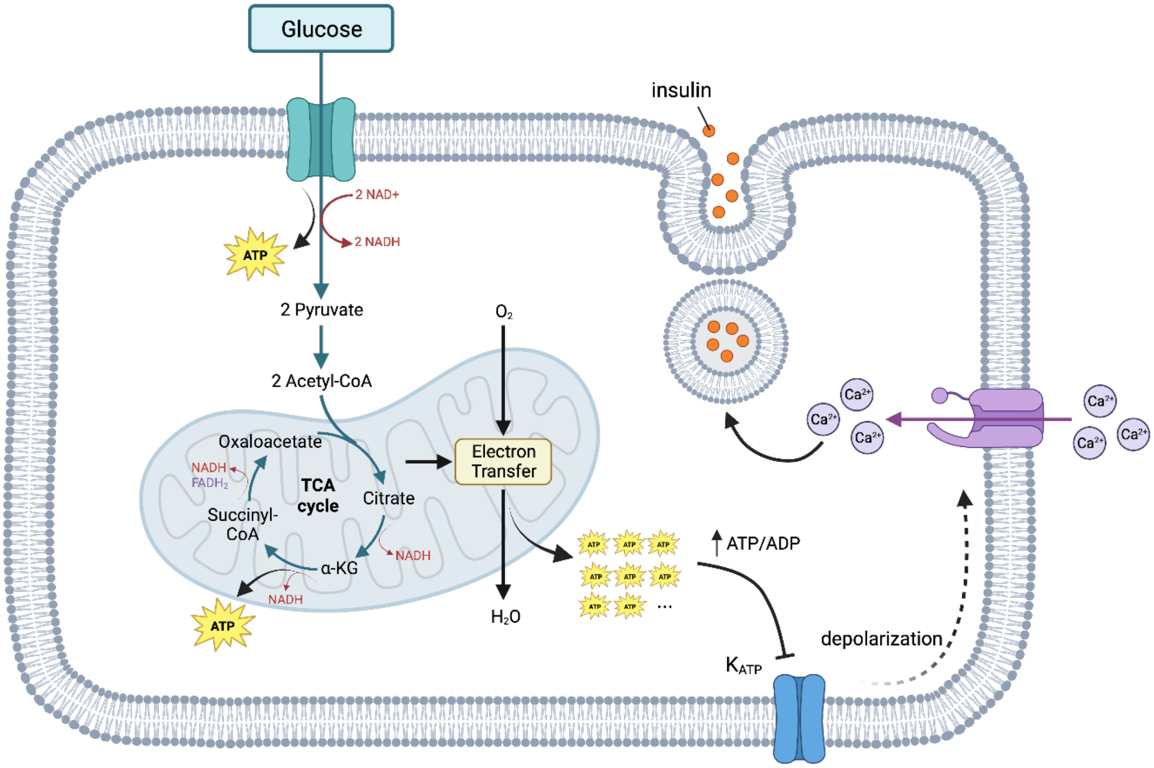

Figure 27. The process of islet metabolism.

3.1.2 The Glucose Stimulated Insulin Secretion Assay

Conventionally, the static Glucose Stimulated Insulin Secretion (GSIS) assay was used to determine the functionality of human islet. This assay has been the golden standard to evaluate islet function for a long time. In this assay, islets are pre-incubated in a low-glucose medium (usually 2 mM) to stabilize their basal insulin secretion, and are then exposed to/stimulated by high glucose solution (usually 16 mM). These glucose concentrations are designed to mimic the physiological range of blood glucose levels. The supernatant is collected at the end of the pre-incubation, and at a specific amount of time after the stimulation, and Enzyme-Linked Immunosorbent Assay (ELISA) can be performed on the samples to determine the concentration of insulin prior and post stimulation. The comparison of the results can indicate the functionality of isolated islets.

Overall, the GSIS assay provides valuable information about the functional state of pancreatic beta cells and their ability to respond to changes in blood glucose levels. However, as an assay based on static incubation, the GSIS assay cannot capture long-term changes of insulin, nor does it have the ability to generate dynamic information of islet metabolism.

3.1.3 Islet Perifusion

Islet perifusion is a method to study the function of pancreatic islets in a dynamic, controlled environment that mimics the in vivo conditions more closely than standard static incubation methods[123]. In an islet perifusion system, isolated islets are placed in a special chamber that allows for the continuous flow of medium over the islets. This 'perifusion' can mimic the blood flow in the body and can be modified to deliver various stimulants or inhibitors to the islets in a controlled manner, allowing the measurement of the islet response to these stimuli in real time. In the traditional experimental setup for islet perifusion system, islets are incubated in the buffer solution with basal glucose initially. The glucose level is then rapidly increased to a high level to elicit insulin secretion which mimics the postprandial rise in blood glucose levels. The buffer solution is continuously perfused through the chamber for a certain amount of time to maintain the elevated glucose concentration and allow for the sustained exposure of the islets to the high glucose level. Eventually, the glucose concentration in the buffer solution is lowered back to the basal level to simulate the return to fasting or normal blood glucose levels. During the experiment, the buffer solution collected at regular intervals is analyzed for insulin concentration using ELISA similar to the GSIS assay. As compared to the GSIS assay, islet perifusion technique can more closely mimics the physiological insulin release pattern in response to fluctuating blood glucose levels, and provides valuable information on the kinetics, frequency, and magnitude of insulin secretion under various conditions[123].

3.1.3.1 Microfluidic islet perifusion system

Islet perifusion method has played an important role for in vitro study of islets. Microfluidics, because of its capability to mimic the in vivo environment due to its microscale, has been a popular choice as the platform for islet perfusion.

In 2009, our lab created an islet perifusion system based on microfluidic technology[124]. In this system, a microfluidic device was designed with a big chamber in the middle for the incubation of islets. The inlet to the microfluidic was connected to a peristatic pump which could perfuse stimulation constantly at a specific flow rate. The outlet of the microfluidic device was connected to a liquid collection system which could collect supernatant for hormones analysis over time. The islets incubated in the microfluidic device were stained with Flouorescein Isothiocyanate (FITC), and the microfluidic device was placed under a fluorescence microscope during the experiment, such that the fluorescence signal overtime from the islets can be captured, which can provide information on top of hormones measurement to monitor islets responses to different stimuli. The work in 2010 validated the microfluidic islet perifusion system on multiple fluorescence indicators [112]. Another work in 2016 incorporated a surface-tension-based pumpless design into the perifusion system, which eliminated the requirement for peristatic pump and greatly simplify the system setup[125].

3.1.3.2 Fluorescence dyes in islet perifusion

Fluorescent dyes that bind to calcium are the most often used probes in the microfluidic perifusion system. As mentioned in previous section, the plasma membrane depolarization caused by glucose metabolism can lead to Ca^{2+} influx, which eventually leads to the secretion of insulin. As a result, intracellular Ca^{2+} concentration is an important indicator of glucose induced insulin secretion. One example of the Ca^{2+} dyes that are often used in islet perifusion system is the Fluo-4[124]. This is a derivative of the fluo-3 dye and can be excited by light around 494nm and emit green fluorescence at approximately 516 nm when it bounds to the calcium ion.

In addition, dyes can be taken up by active mitochondria with intact membrane potential. One example is the Rhodamine-123. Rhodamine-123 is a cationic dye that can be excited by light around 488 nm, and emits fluorescence in the orange-red range (525 nm). It can passively diffuse across cell membranes and preferentially accumulate in mitochondria due to the negative mitochondrial membrane potential. This means that extent of Rhodamine 123 accumulation in mitochondria is directly proportional to the mitochondrial membrane potential[126]. Such accumulation can be affected due to the mitochondria activity during glucose metabolism, and thus, Rhodamine-123 can also be used to monitor the glucose induced insulin secretion process of islet beta cells.

Despite the fact that these fluorescent dyes have been widely used in the study of islet functionality, it still has some limitations. For example, small molecular dyes may lack specificity and can bind nonspecifically to various cellular structures or exhibit off-target interactions[127, 128]. Also, some small molecular dyes may exhibit cytotoxic effects, particularly at higher concentrations or prolonged exposure[129], which makes it no applicable in long-term imaging studies or in-vivo studies.

3.1.3.3 Genetically Encoded Fluorescence Protein Bio-Indicator in islet perifusion

Due to the limitations of small molecular dyes, researchers started to explore the possibility of using Genetically Encoded Fluorescence Protein Indicator (GEFPI) in the study of islet functionality. Genetically encoded fluorescence protein indicators are proteins that have been genetically modified to incorporate a fluorescent protein domain. These proteins are typically derived from naturally occurring fluorescent proteins, such as green fluorescent protein (GFP), and engineered to exhibit specific properties. The genetic modification allows these indicators to be produced within living cells through gene expression. By fusing the indicator protein to a target protein or incorporating it into a specific cellular compartment, researchers can track the localization, expression, or activity of the target protein in real-time. An example of the sensor is the ZIBG2 sensor modified from GFP[130]. This is a Zinc sensor that can effectively target to the extracellular size of the plasma membrane and can be used to monitor glucose-induced dynamic Zn^{2+} secretion from pancreatic islets[130]. Another example is the GCamP6m, which is also a family of GFP indicator. This sensor is a Calcium sensor, which is developed by combining a circularly permuted GFP, a calmodulin (CaM) domain, and a calcium-binding M13 peptide[131]. Similar to the Fluo-4 and Fura-2 sensor, the GCamP6m sensor is an indicator of Ca^{2+}, and can be used to monitor the Ca^{2+} caused by the islet metabolism, and thus, analyze the islet functionality.

3.1.3.4 Other stimuli in islet perifusion

Other than glucose, other stimuli are also used in islet perifusion system to test the functionality of islets. Some of the examples are Potassium Chloride, Tolbutamide, and Diazoxide. When high concentration KCl is supplied to the islets, it increases the extracellular concentration of K+, causing the aggregation of positive charge inside the cell membrane, and leads to depolarization of the membrane. As mentioned in previous section, this can further cause Ca^{2+} influx and results in insulin secretion. In most cases, KCl represents an artificial condition and may not fully replicate the physiological regulation of insulin secretion in vivo. However, it is often used along with other stimuli to test the intrinsic capacity of islet cells to respond to depolarizing stimuli and release insulin. Tolbutamide is a medication that belongs to the class of drugs known as sulfonylureas[132]. It is primarily used in the management of type 2 diabetes mellitus to help control blood sugar levels. It functions by binding to the sulfonylurea receptor on the beta cells of the pancreas, which leads to the closure of K_{ATP} channels, and further trigger the secretion of insulin. Diazoxide, to the opposite, is a medication that raises blood sugar by slowing the release of insulin from the pancreas[133]. It functions by opening the K_{ATP} channels and suppresses the depolarization of cell membrane caused by the metabolism of glucose.

3.2 Methodology

3.2.1 Design of the Smartphone-Fluidic Fluorescence Digital Imaging Analysis system

The smartphone imaging system consists of a smartphone, and a set of detachable lenses for magnification as described earlier[134]. In addition, a set of fluorescence filters were integrated into the system (Thorlabs, Newton, NJ). The fluorescence filters, including an excitation filter, an emission filter, and dichroic mirror, were held in a dichroic cube (Thorlabs, Newton, NJ), and were inserted between the objective lens and the ocular lens as shown in Fig. 28.

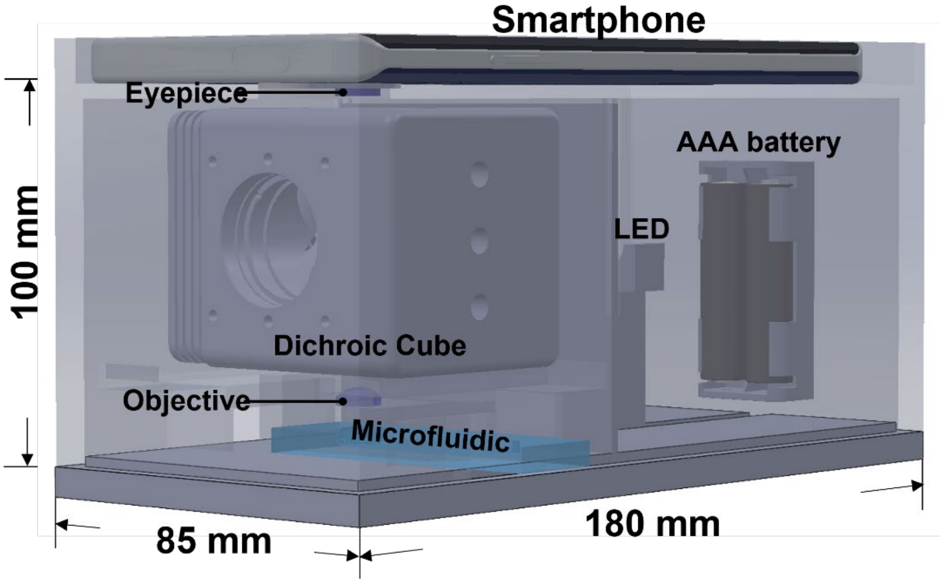

Figure 28. Design of the smartphone-based fluorescnece imaging system.

A white LED (Thorlabs, Newton, NJ) powered by 2 AAA batteries (Duracell) was placed to the right of the excitation filter to provide illumination. The light went past the excitation filter which eliminate all the light band except for the excitation light. The light then got reflected by the dichroic mirror, and casted on the sample. The fluorescence marker in the sample got excited and emitted the emission light, which went pass the dichroic mirror and got captured by the smartphone camera. Fig. 29 shows the light path of the system.

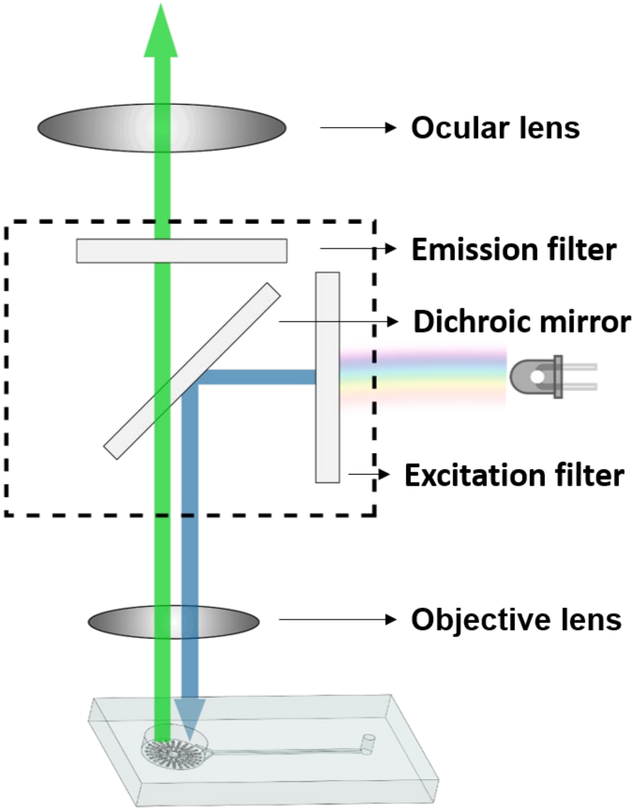

Figure 29. Optical principle of the smartphone-based fluroescence system.

To make the system truly portable and simplify the experimental procedures for researchers to perform, the microfluidic biochip for islet imaging was designed based on our previously reported surface tension driven pumpless device[125]. The principle of the design could be depicted by Young-Laplace equation, which describes the pressure difference across the interface of two static fluids (air and the liquid within the droplet at inlet/outlet) due to surface tension. The equation is as shown below:

$$\Delta P = \gamma(\frac{1}{R_1} + \frac{1}{R_2}) \quad (27)$$

Where ΔP is the pressure difference between the two interfaces, R_1 and R_2 are the principal radii of the curvature of the interface, and γ is the surface tension of the fluid. When considering the droplet to be a spherical drop, $R_1 = R_2$, which can simplify the equation to the following:

$$\Delta P = \frac{2\gamma}{R} \tag{28}$$

This indicates that a small droplet would have a bigger net pressure (difference between the atmospheric pressure and the internal pressure of the droplet). If two chambers with different sizes are connected by a channel, and the liquid is loaded at the smaller chamber, it will be driven by surface tension to the larger chamber.

The design of the microfluidic device used in this work is shown in Fig. 30. This is a two-layer PDMS device. The device was fabricated using the photo-lithography technique as mentioned in the previous chapter. The device has a 1mm inlet, a 10mm outlet, and a 34.25 mm long channel connecting the two. The channel was designed to be 0.5mm wide and 0.4 mm tall, such that most of the islets would not be trapped in the channel. The outlet also served as the islet incubation chamber, with small microwells (500 µm in diameter) sitting at the bottom to trap islets for observation. An extruded structure as placed near the outlet (islet incubation chamber) to minimize the liquid turbulence generated by flow and to prevent islets from moving.

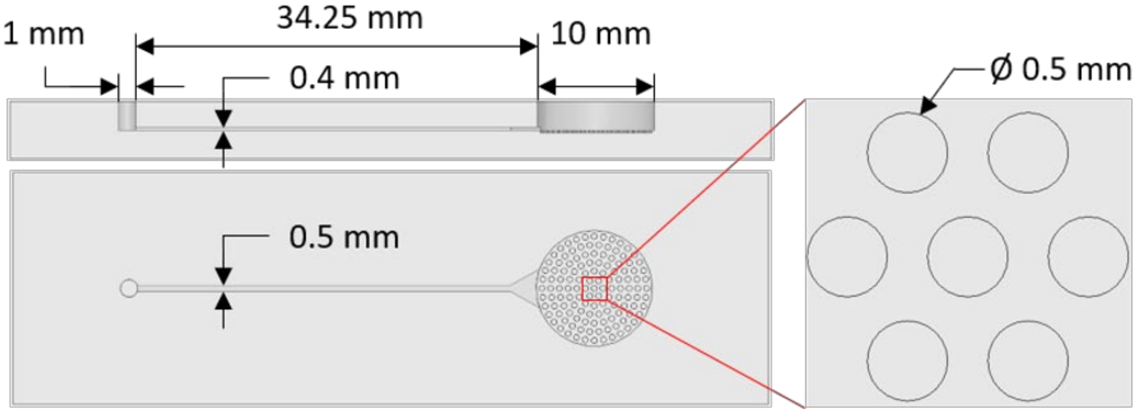

Figure 30. Design of the microfluidic device. The two images on the left are the front and side view of the device. The image on the right is an amplified view of the cell-loading wells.

To further validate the microfluidic design, a COMSOL Multiphysics model was carried out using Laminar Flow and Transport of Diluted Species method (Fig. 31A). The Navier-Stokers equations were utilized in the application to characterize the momentum transport of the fluid with the conservation of mass and the surface tension. A sweep function of concentrations with set parameters of 8, 14, and 20 mM were applied in the inlet droplet, while a concentration of 2 mM was defined inside of the device. The diffusion coefficient of glucose was set to be 9.59×10^{-10} m^2/s[135]. A moving triangular mesh and automatic remeshing were used to achieve accurate deformation of the droplet at the inlet. The simulation result showed that for all three concentrations, glucose could be delivered from inlet to the cell loading chamber within 4 sec (Fig. 31B).

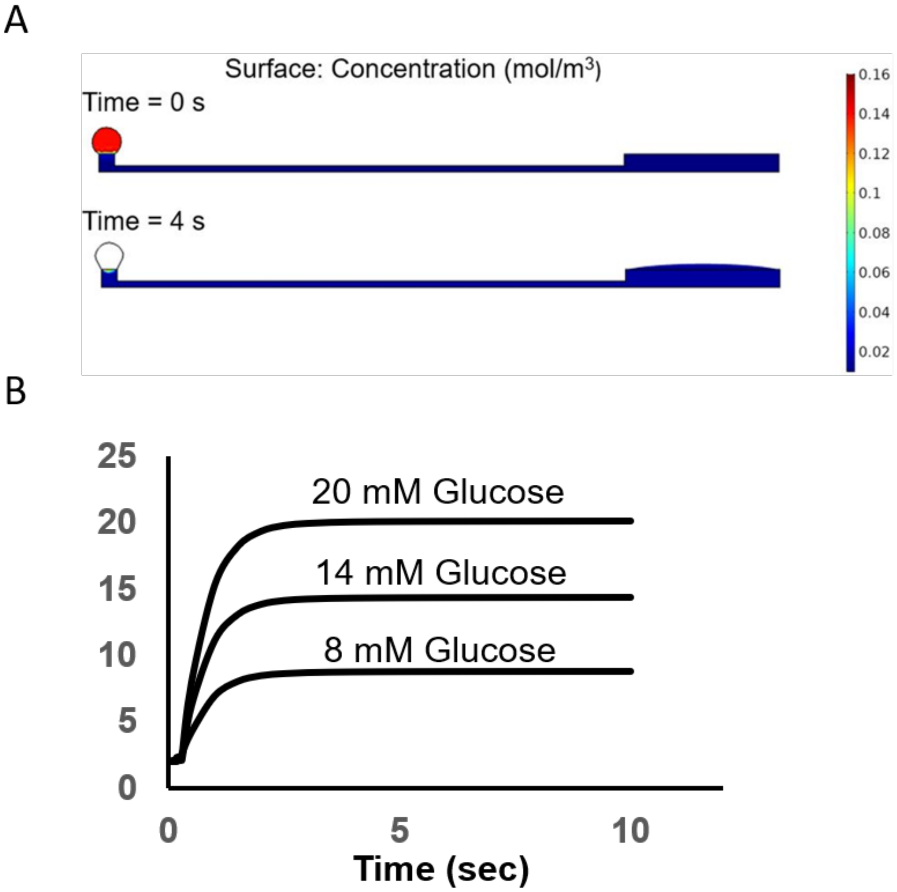

Figure 31. Simulation of liquid diffusion in the microfluidic device. **(A)** Simulation setup in COMSOL. **(B)** Simulation result of glucose concentration vs. time.

3.2.2 Mouse islet isolation and culture

In this work, the islets used were isolated from the C57/B6 mouse of 8-10-week-old. In the isolation procedure, the mouse pancreata was perfused with 0.375 mg/mL collagenase P (Roche

Diagnostic GmbH, Mannheim, Germany) and was then digested for 12 min at 37°C. The digested pancreata were shaken vigorously for 15 s and further purified through discontinuous Ficoll gradient. The purified islets were cultured in 95% air and 5% CO2 at 37°C with RPMI-GlutaMAX-1640 (Gibco, Amarillo, TX) supplemented with 10% fetal bovine serum (Corning, Corning, NY), All procedures were approved by the Animal Care and Use Committee at the University of Virginia.

3.2.3 Buffer solution preparation

Krebs Ringer Buffer (KRB) was used for the preparation of solutions for different stimuli and fluorescence dyes. The buffer was made by mixing 129 mM, NaCl, 5 mM $NaHCO_3$, 4.7 mM KCl, 1.2 mM KH_2PO_4, 1 mM $CaCl_2.2H_2O$, 1.2 mM $MgSO_4.7H_2O$, 10 mM HEPES, and 5% FBS at pH 7.35-7.40.

3.2.4 Fluorescence imaging of islets

In this work, two fluorescence dyes (Fluo-4-AM and Rhodamine-123) and one genetically encoded fluorescence protein bio-indicator (GCaMP6m) were used to validate the

Fluo-4-AM (Thermo Fisher Scientific, Waltham, MA) was prepared in DMSO and diluted to a final concentration of 5 μM in Krebs-Ringer (KR) buffer with 2 mM glucose (KR2). Rhodamine-123 (Thermo Fisher Scientific, Waltham, MA) was prepared in 100% ethanol and diluted to a final concentration of 2 μM in KR2. The islets were incubated in the KR2 buffer with Fluo-4 or Rhodamine-123 for 30 min at 37°C before loading into the microfluidic device.

The genetically encoded protein sensor for calcium was delivered into islets using adeno-associated virus (AAV). To generate the virus, the sensor was first cloned into a pAAV viral transfer plasmid. The product construct was then co-transfected with pAdDeltaF6 and pAAV2/9n packing plasmids in HEK 293T cells. The crude virus was collected after four days of expression. A density gradient ultracentrifugation was performed to purify the virus. Titer of the virus was determined using qPCR-based methodology adapted from Addgene[136]. Islets were handpicked into each 96-well with 100 μL complete medium and 10 μL of AAV (titer of 1x1014 GC/ml) were then added for a 20-hour incubation in 37°C.

A GFP filter set (452-488 nm /506-545 nm, Iridian spectral technology, Ottawa, ON, Canada) was used to observe Fluo-4 fluorescence dye and the GEFPI. The smartphone camera was set to

200 ISO and 1/10 shutter time, and images were captured at 15 s intervals. The chamber was filled with KR2 buffer initially, and the fluorescence-labelled islets were then carefully loaded into the open top chamber in the microfluidic device using a 20 µL pipette. KRB containing varying glucose concentrations (2, 14, or 20 mM) and KCL (30 mM) were introduced to islets through the inlet. Tolbutamide (Sigma-Aldrich, St. Louis, MO) and Diazoxide (Sigma-Aldrich, St. Louis, MO) were prepared in KR2 buffer with a final concentration of 250 µM and 200 µM, respectively.

A YFP filter set (Iridian spectral technology, Ottawa, ON, Canada) was used to observe the Rhodamine-123. The filter set had an excitation band of 489-505 nm, and an emission band of 524-546 nm. The camera setting used for Rhodamine-123 was identical to the ones used for Fluo-4 and the GEFPI.

3.2.5 Software development for islet imaging

The video processing software was developed using python 3.9.5 (Python Software Foundation, Wilmington, DE) and OpenCV. The software was designed such that the user can select multiple Regions of Interest (ROIs). The acquired video first went through background subtraction. Average values of the green channel within each ROIs were then calculated to represent the fluorescence intensity. The results were plotted as fluorescence intensity vs. time for review by the user.

3.3 Results and discussion

3.3.1 Imaging resolution validation of optical system

A resolution target (Edmund Optics, Barrington, NJ) was used to validate the resolution of the imaging system. Fig. 32A shows the validation result.

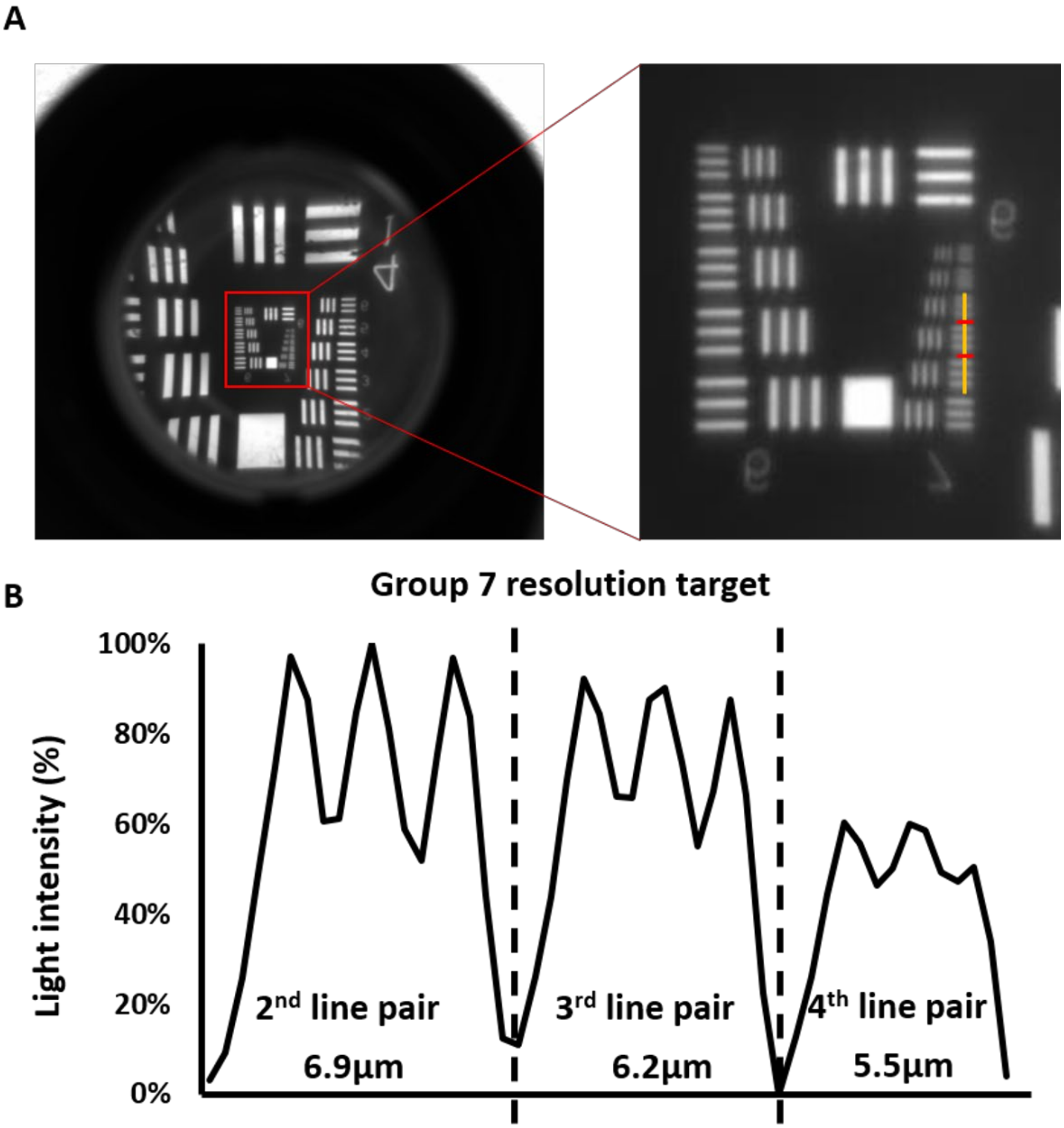

Figure 32. Validation of the magnification system. **(A)** Images of the resolution targets. The lowest resolved groups (Group 7) are highlighted using red box in the image on the left**,** and the image on the right is the zoom -in image of the highlighted area with a yellow vertical line cut in the middle of the horizontal line pairs. **(B)** The corresponding cross-sectional plot of the intensity along the yellow vertical line.

All the lines up until the 3rd line pair (6.2 µm) in group 7 could be clearly distinguished. Starting from the 4th line pair (5.5 µm) in group 7, the contrast between the bright and dark line could no longer be well-identified. Fig. 32B plotted the light intensity along the yellow line. The curve quantified the level of contrast of the 2nd – 4th line pairs in group 7, and the average difference between the peak values in bright lines and the bottom values in dark lines descended from ~20% to ~10%. Both Fig. 32A and Fig. 32B showed that the 3rd line pair in group 7 was a good representation of the maximum resolvable resolution, which was 6.2 µm. In Fig. 33, the resolution validation result of imaging system with not magnification was presented. The result indicated that the maximum resolvable resolution was ~99 µm, meaning that the magnification setup mentioned in chapter 2.1 brought a ~15 times enhancement on spatial resolution. Given that islets had diameters larger 50 µm in most cases, such enhancement ensured that the imaging system has enough resolution for islets imaging.

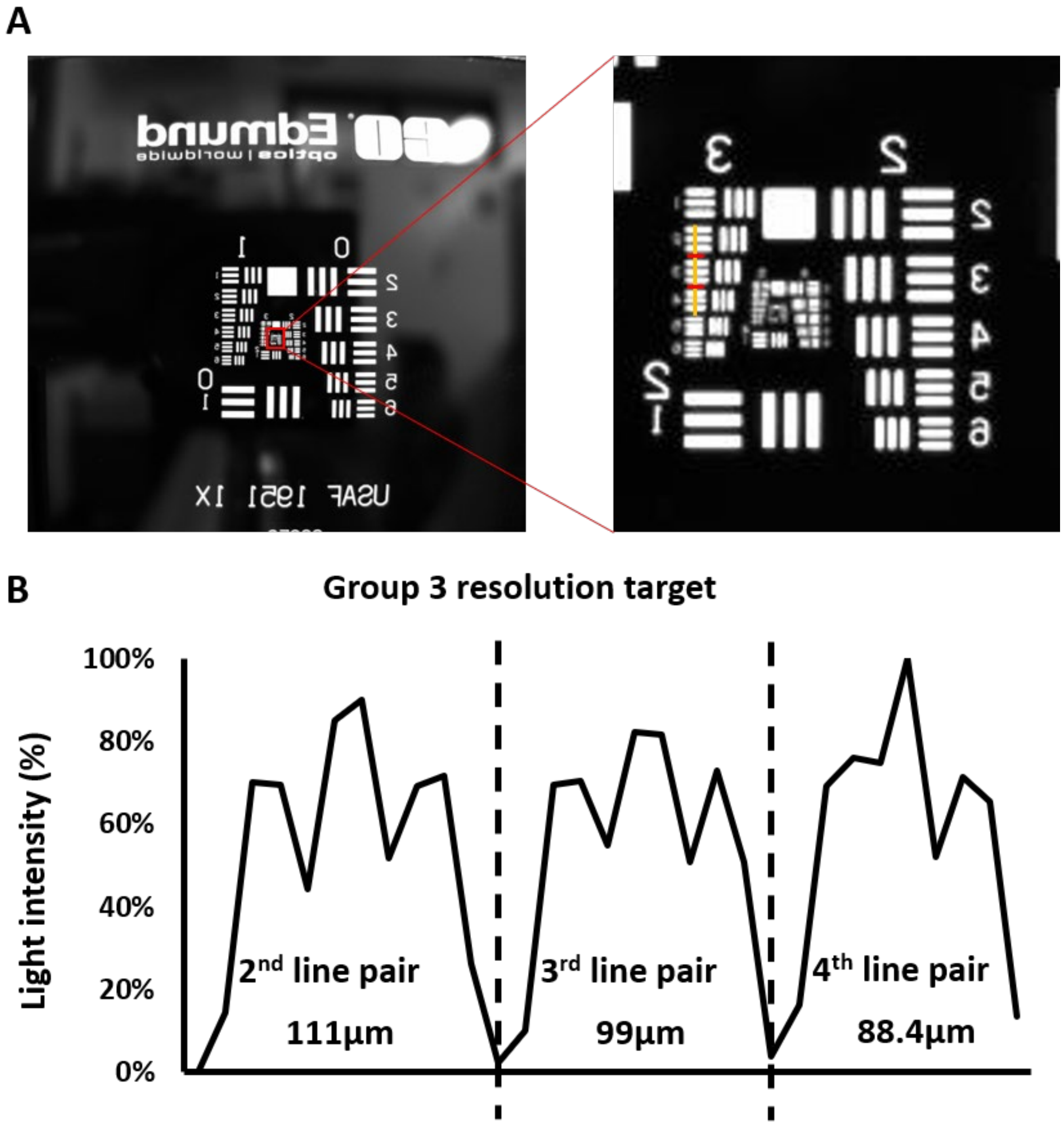

Figure 33. Validation of the optical system with no magnification. **(A)** Images of the resolution targets. The lowest resolved groups (Group 3) are highlighted using red box in the image on the left**,** and the image on the right is the zoom - in image of the highlighted area with a yellow vertical line cut in the middle of the horizontal line pairs. **(B)** The corresponding cross-sectional plot of the intensity along the yellow vertical line.

3.3.2 Intracellular insulin stimulator-secretion coupling factors in response to stimuli

Beta-cell insulin secretion stimulated by glucose is governed by glucose metabolism, electrical activity, ion signaling, and hormone exocytosis. As mentioned in previous chapter, glucose enters beta-cells via the $GluT_2$ transporter, and glycolysis leads to the generation of pyruvate. Pyruvate then enters mitochondria and generates ATP through the TCA cycle. The increased ATP facilitates the closure of ATP-sensitive potassium channels (K_{ATP} channels) and depolarization of the plasma membrane that triggers Ca^{2+} influx through VDCC and induces exocytosis of insulin, C-peptide, and proinsulin. The processes display complex biphasic and pulsatile kinetic profiles. Chemical dyes, fluorescence, and confocal imaging are often employed to study beta-cell intracellular activities such as calcium influx, mitochondrial potential changes, zin release kinetics, ROS production, and many others. In this study, we used Fluo-4 and Rhodamin-123 to monitor cellular calcium influx and mitochondrial potential, respectively.

3.3.2.1 The effects of photo-bleach and shear stress

The photo-bleach in fluorescence imaging caused by the overwhelming exposure can lead to loss of fluorescence signals and affect the analysis results. Also, the shear stress generated from fluid flow in a microfluidic channel may induce calcium ion influx in pancreatic beta-cells[137]. Therefore, we seeded the islets in 2mM glucose initially, and added 10 μL of 2mM glucose at 5 min and 20 min. We monitored the intracellular fluorescence calcium signals over 30 min and the result is shown in Fig. 34. The intensity curve was almost flat, indicating that the photo-bleach effects were neglectable. Minor fluctuations could be observed at 5 min and 20 min when flow was delivered, but the fluctuations were very minimal (< 3%), meaning that the shear stress from the pumpless flow delivery did not have significant impact on the fluorescence signal acquisition.

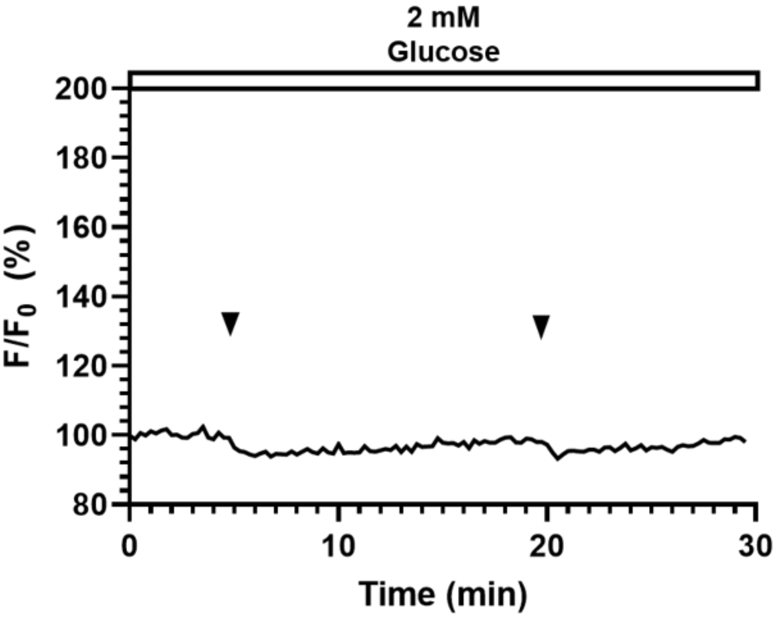

Figure 34. Representative tracings of [Ca^{2+}]$_i$ in mouse islets following continuous addition of 2 mM glucose (Fluo-4).

3.3.2.2 Response of fluo-4 labeled islets to glucose stimulation

Fluo-4 is one of the small molecular dyes that is widely used to monitor the metabolism process of islets. Fluo-4 is a fluorescence dye that can bind to calcium ion and emit fluorescence. It has an excitation wavelength of 494 nm and emission wavelength of 506nm. Fig. 35 shows the representative responses of starved islets stimulated with 8mM glucose starting from 5 min, and 20mM glucose starting from 20 min. The fluorescence signal was increased to 158.2% (164.7% ± 10.8) in response to 8 mM glucose, and 165.0% (163.1% ± 15.8) in response to 20 mM glucose. Importantly, the system can clearly detect a typical biphasic calcium pattern under glucose stimulation. When comparing the two responses, the two peaks had similar height, yet while the second one (20 mM) managed to maintain a high level, the first response (8 mM) started to decrease within ~2min and reached to 119.2% (114.5% ± 12.0) before the second stimulus was added. These results suggested that delivery of stimuli to islets can be achieved with the proper concentrations through the surface tension driven liquid delivery process.

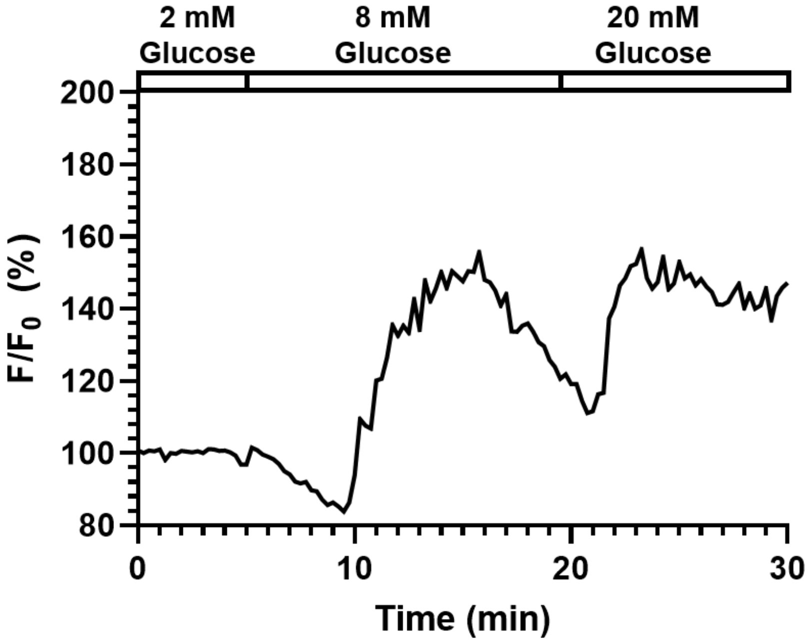

Figure 35. Representative tracings of $[Ca^{2+}]_i$ in mouse islets following glucose stimulation at varying concentrations (8 and 20 mM) (Fluo-4).

Fig. 36 shows the representative responses of starved islets stimulated with 14mM glucose starting from 5 min, and 30mM KCl starting from 20 min. The fluorescence intensity first experienced a slight drop to 85.2% (86.8% ± 2.9) corresponding to phase 0, and then started to quickly increase until reaching the highest value of 167.6% (157.0% ± 9.5). The fluorescence intensity maintained a high level with a slight drop, until KCl stimulation at 20 min, when the fluorescence intensity further increased to 197.81% (183.5% ± 17.0). This is a clear biphasic pattern, with the second peak significantly higher than the first one. When high concentration KCl was used to stimulate the islets, the increase level of extracellular potassium ion concentration would lead to the depolarization of cell membrane, and cause the voltage-gated calcium channel to open to the and eventually result in the increase of insulin secretion. With the experimental setup used in this work (14 mM glucose and 30mM KCl), the response from KCl should be much higher than the one from glucose. The result observed from the smartphone system matches the expectation of a glucose-KCl stimulation assay. The fact that the small drop in phase 0 can be detected by the system shows that the system has enough fluorescence intensity resolution.

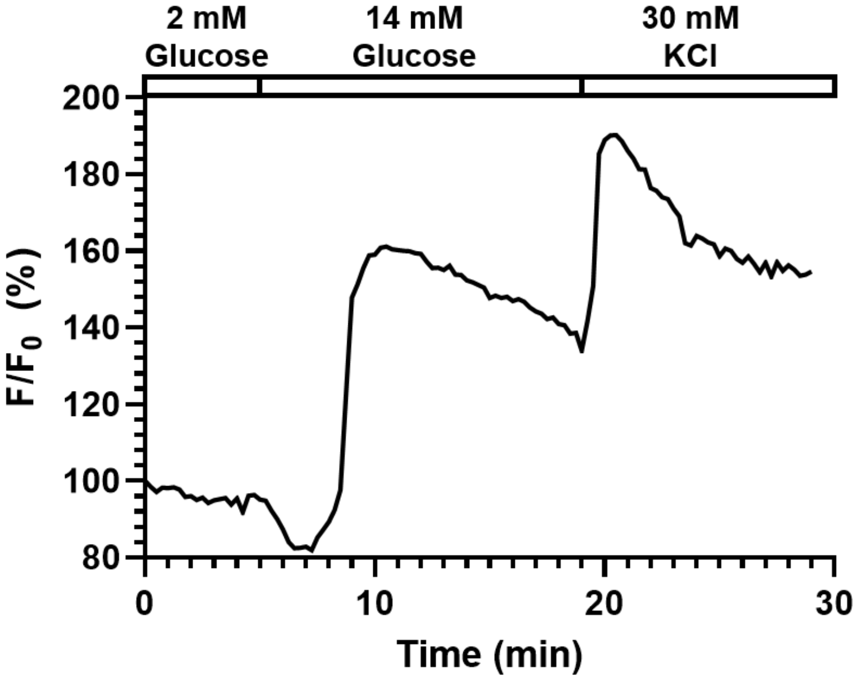

Figure 36. Representative tracings of [Ca^{2+}]$_i$ in mouse islets following 14 mM glucose and 30 mM KCl stimulation (Fluo-4).

3.3.2.3 Response of fluo-4 labeled islets to other stimuli

Diazoxide and Tolbutamide are two drugs that are often used to manage blood glucose for diabetes patients. In this work, both the drugs were used to stimulate islets.

Fig. 37 shows the representative responses of starved islets stimulated with 14 mM glucose starting from 5 min, and 250 µM Diazoxide starting from 20 min. The fluorescence intensity first increased to 133.8% (145.3% ± 14.7) after the glucose stimulation. It then dropped to 108.8% (114.4% ± 13.2) 2 min after 250 µM Diazoxide was added, and continued dropping at a relatively slower rate afterward. Diazoxide functions as a potassium channel opener. When islets were stimulated by Diazoxide, the closure of potassium channel caused by glucose intake would be countered, and thus, the cell membrane polarization would be prevented. As a result, the voltage-gated calcium channel would be closed, and the amount insulin secretion would be decreased. The result observed from the smartphone system matches this expectation.

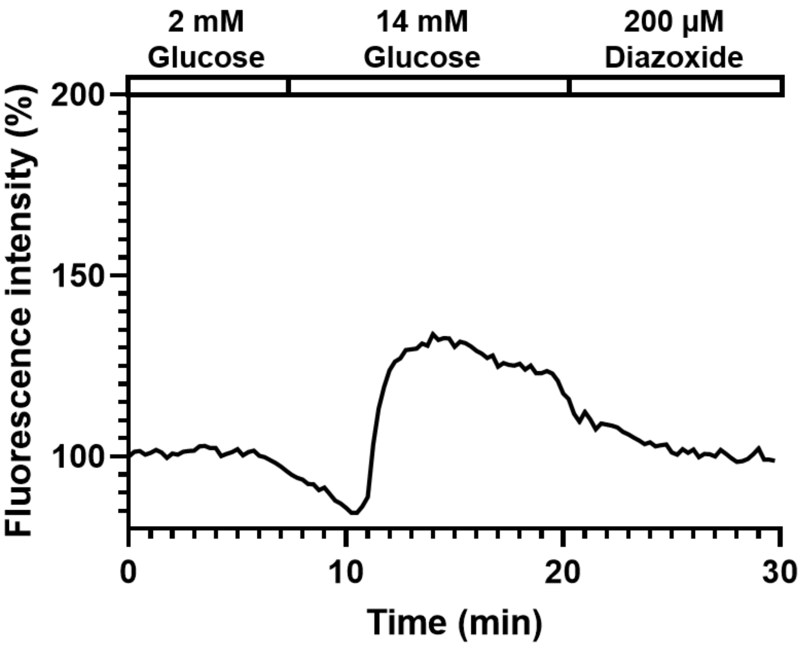

Figure 37. Representative tracings of $[Ca^{2+}]_i$ in mouse islets following 14 mM glucose and 200 µM Diazoxide stimulation (Fluo-4).

Fig. 38 shows the representative responses of starved islets stimulated 14 mM Tolbutamide starting at 5 min. The fluorescence intensity increased to 151.8% (141.2% ± 17.0) in response to 200 µM Tolbutamide. Tolbutamide functions as a potassium channel closer. When islets were stimulated by Tolbutamide, the potassium channel would close even when there were no intracellular ATP level changes. As a result, the voltage-gated calcium channel would be open which would lead to calcium inflow and insulin secretion. The result observed from the smartphone matched this expectation.

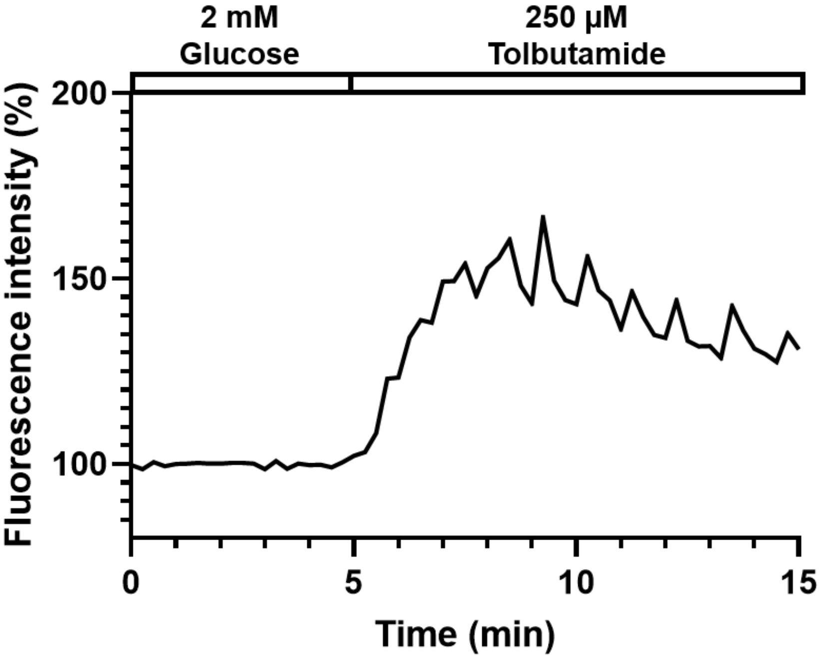

Figure 38. Representative tracings of $[Ca^{2+}]_i$ in mouse islets following 250 μM Tolbutamide stimulation (Fluo-4).

3.3.2.4 Response of Rhodamine-123 labeled islets to other glucose

Another small molecular dye (Rhodamine-123) with a different excitation/emission wavelength (507 nm/ 529 nm) was also used to test the smartphone system in this work. Rhodamine-123 was a positively charged molecule that could accumulate in the mitochondria and be used to monitor mitochondrial activity driven by its membrane potential.

Fig. 39 shows a representative response of Rhodamine-123-labeled starved islets stimulated with 14 mM glucose at 5 min. The fluorescence intensity dropped to 89.2% (88.5% ± 2.8) right after the stimulation was added. When glucose was added to the islets, the increased metabolism process would cause the potential of inner mitochondrial membrane to turn negative, and result in the intake of Rhodamine-123. As a result, the fluorescence intensity would decrease. The result observed from the smartphone matched this expectation.

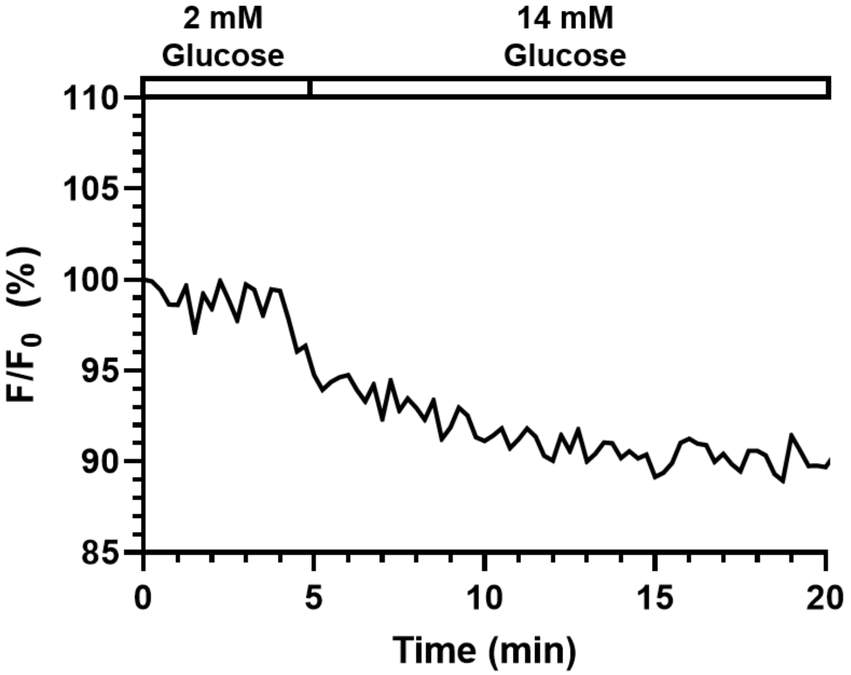

Figure 39. Representative tracings of Ψmito in mouse islets following 14 mM glucose stimulation (Rhodamine-123).

3.3.3 Fluorescence imaging of islets labelled with GEFPIs

One of the challenges in islet biology is to visualize biomolecules in their natural environment in real-time and in a non-invasive fashion, so as to gain insight into their physiological behaviors and highlight alterations in pathological settings. Genetically Encoded Fluorescence Protein Indicators (GEFPIs) constitute a class of imaging agents that enable visualization of biological processes and events directly in situ, preserving the native biological context and providing detailed insight into their localization and dynamics in cells. In this work, a calcium GEFPI was expressed in islet cells and then imaged using the smartphone system.

3.3.3.1 The effects of photo-bleach and shear stress

For reasons similar to the Fluo-4 labeled islets, a test was done to make sure that the neither photo-bleach effect nor the shear stress generated from fluid flow would affect the fluorescence observation during the experiment. Similar to the test we did for the Flu-4-labeled islets, we added 2mM glucose at 5 min and 20 min, and monitored the islets calcium signal for 30 min. The result is shown in Fig. 40. Similar to the result from Fluo-4 labeled islets, the curve was nearly flat, and almost no fluctuation could be observed at 5 min and 20 min. This indicates that neither the photo-bleach, nor the shear stress would affect the observation of calcium signal during the experiment.

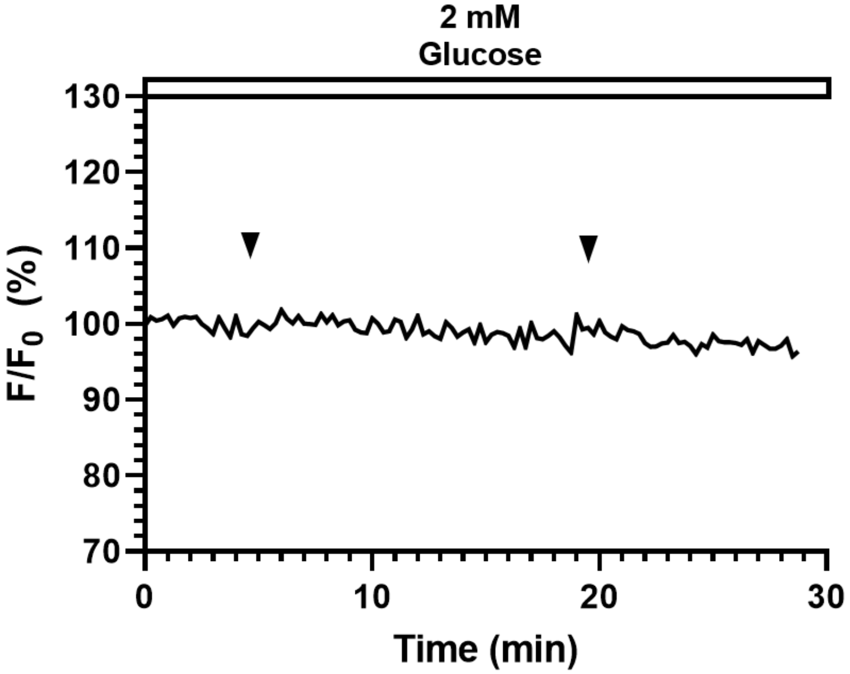

Figure 40. Representative tracings of $[Ca^{2+}]_i$ in mouse islets following continuous addition of 2 mM glucose (GEFPI).

3.3.3.2 Response of GEFPI-labeled islets to glucose stimulation

Fig. 41 shows a representative response of GEFPI-labeled starved islets stimulated by 14 mM glucose at 5 min. The fluorescence intensity first experienced a minor drop after the glucose stimulation, and then quickly increased to 110.0% (113.1% ± 4.8). Overall, the fluorescence intensity of biosensor was lower than that of fluo-4, and the increase in response to glucose stimulation was also smaller, but the smartphone system managed to capture the signal emitted by the biosensor and identify the difference between pre- and post- glucose stimulation.

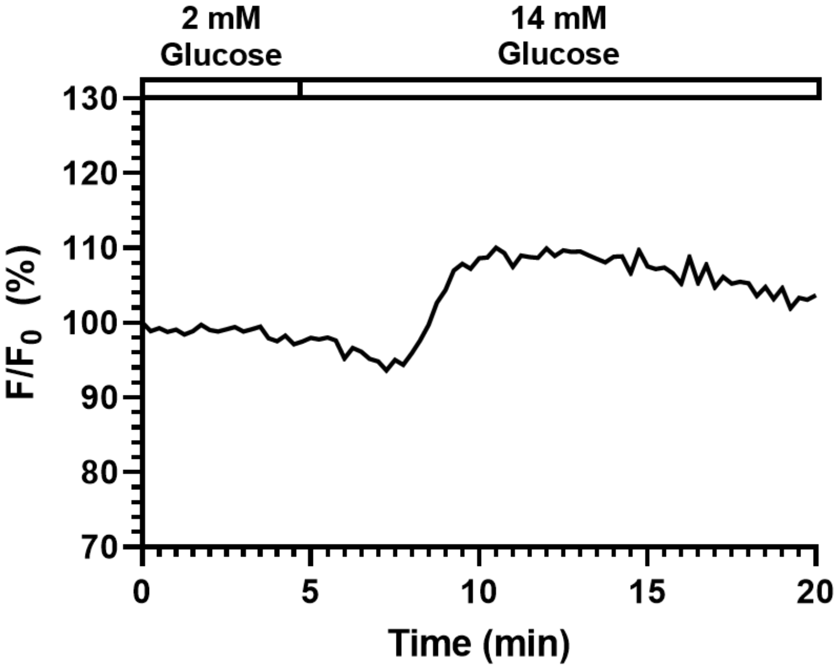

Figure 41. Representative tracings of $[Ca^{2+}]_i$ in mouse islets following 14 mM glucose stimulation (GEFPI).

3.3.3.3 Response of GEFPI-labeled islets to other stimuli

We also tested the GEFPI-labeled islets with Diazoxide and Tolbutamide. Fig. 42 shows a representative response of GEFPI-labeled starved islets stimulated by 14 mM glucose at 5 min and 250 µM Diazoxide at 20 min. The fluorescence intensity first climbed to 116.9% (115.9% ± 2.3) after the 14 mM glucose stimulation at 5min, and quickly decreased to 83.1% (87.9% ± 7.6) 2 min after the Diazoxide was added.

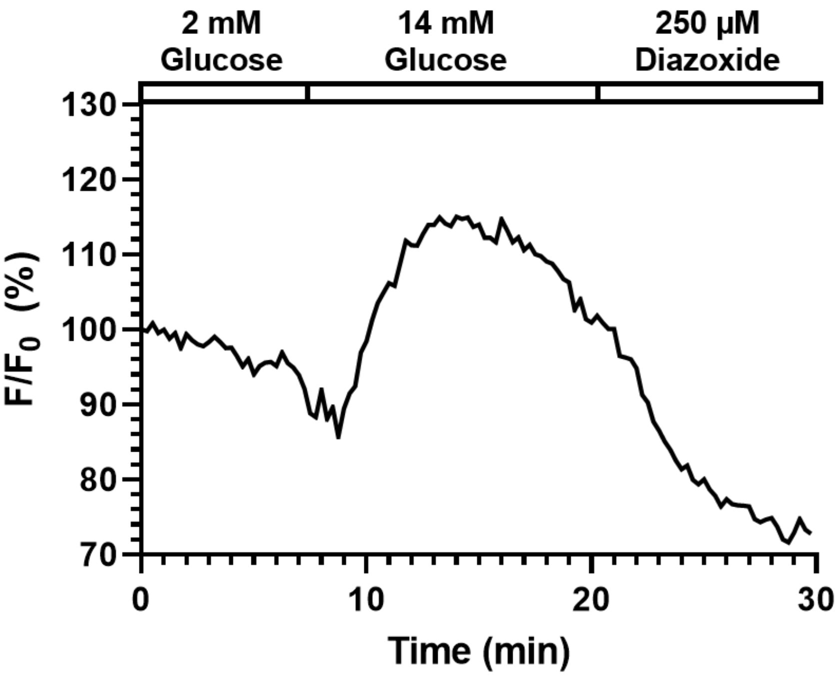

Figure 42. Representative tracings of $[Ca^{2+}]_i$ in mouse islets following 14 mM glucose and 200 µM Diazoxide stimulation (GEFPI).

Fig. 43 shows a representative response of GEFPI-labeled starved islets stimulated by 200 µM Tolbutamide at 5 min. The fluorescence intensity increased to 116.4% (115.1% ± 2.1) after the 14 mM glucose stimulation at 5min, and quickly decreased to 83.1% (87.9% ± 7.6) 2 min after the Diazoxide was added.

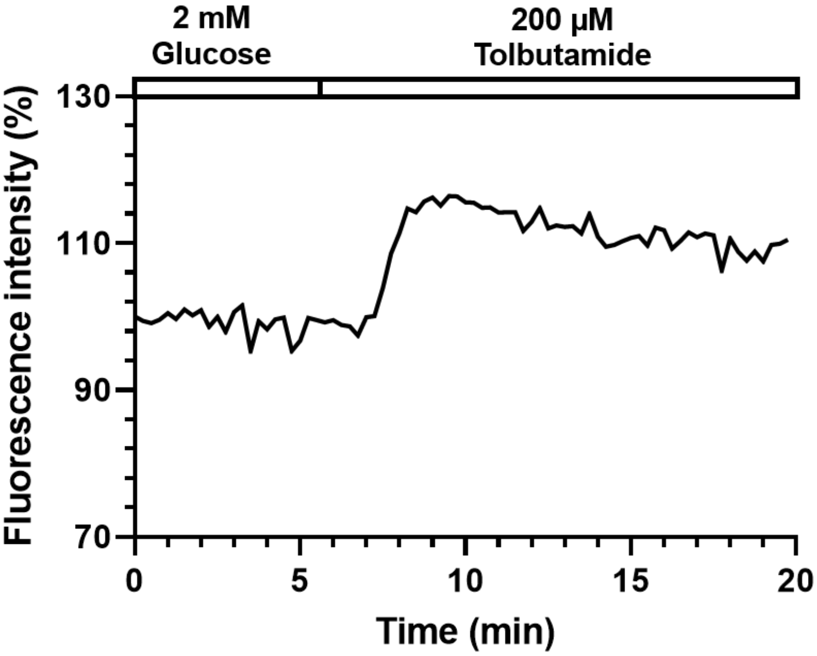

Figure 43. Representative tracings of $[Ca^{2+}]_i$ in mouse islets following 250 µM Tolbutamide stimulation (GEFPI).

Similar to glucose, the responses to these two stimuli were relatively smaller than that of Fluo-4. However, the results still matched our expectation.

3.3.4 Conclusion

In this project, we developed a novel smartphone-microfluidic fluorescence imaging system to study the physiology of islet beta-cells. By trapping islets in a customized surface tension driven pumpless microfluidic device, we managed to use the smartphone camera to visualize mouse islets labelled with various fluorescence indicators and detected physiological insulin stimulator-secretion coupling factors. These were in response to different stimuli/inhibitors with decent fluorescence signaling and signal vs. noise ratio. We also achieved adequate resolution of single islet insulin secretion. When compared to conventional fluorescence-microscope microfluidic perfusion systems, the portable system allowed an easier setup and a much lower cost. One limitation with the current system setup is that current setup can only work with one fluorescence spectrum at a time. However, this problem can be resolved in the future by implementing filter switch functionality into the system with the help of a motorized filter wheel.

In conclusion, the presented smartphone-microfluidic imaging system reveals a possible implementation of portable, low-cost fluorescence imaging to study the insulin secretion kinetics of islet beta-cells. One future direction of this work will incorporate the concepts of big data and machine learning to transform the system into a front-end device for islet data gathering, while embedding a fully trained analysis model such that the system can generate assistive results on cell functionality.

CHAPTER 4. Smartphone-based Imaging Systems for Blood Creatinine Measurement

4.1 Introduction

4.1.1 Kidney function Assessment

Kidney is vital organ in our body, which possesses the responsibility for filtering out waste and excess substances from the blood while regulating the balance of electrolytes and the production of red blood cells. However, it is susceptible to damage from high blood sugar levels and other diabetes-related complications[138]. As a result, assessing kidney function becomes essential in managing diabetes and preventing the progression of kidney disease.

Creatinine is a chemical waste molecule that is produced during normal muscle metabolism. It is generated from creatine, a molecule involved in energy production in muscles[139]. Creatinine is primarily filtered by the kidneys and excreted in urine, making it a useful marker for assessing kidney function[140]. In clinical practice, creatinine is commonly measured in blood samples to evaluate kidney health and monitor renal function, Elevated levels of creatinine in the blood may indicate impaired kidney function.

4.1.1.1 Clinical measurement for creatinine

In clinical practices, creatinine can be measured from blood samples or urine samples[141]. Blood creatinine measurement involves an evaluation of blood samples taken from a vein in patient arms. The normal range for blood creatinine is 0.74 to 1.35 mg/dL for me and 0.59 to 1.04mg/dL for women. Urine creatinine measurement on the other side, involves the evaluation of urine samples over 24 hours. The normal range for urine creatinine is 20-320 mg/dL for men and 20-275 mg/dL for women. Compared to urine test, blood creatinine test has the advantages like low time consumption and low operation cost since it only requires one single blood sample, low variations and etc.[141]

Jaffe reaction was first introduced by Max Jaffe in 1953[142]. It is a colorimetric reaction that involves mixing the sample containing creatinine with an alkaline solution (usually sodium hydroxide) and picric acid. The alkaline environment converts creatinine to creatinine picrate, resulting in the formation of the colored complex named the Janovsky Complex as shown below:

$$\text{Creatinine + Picric Acid} \xrightarrow{OH^-} \textbf{Janovsky Complex}$$

Throughout the reaction the color changes from yellow (picric acid) to red (Janovski complex). By detecting the intensity of color or optical density (absorption) at 520 nm[143], creatinine concentration can be calculated. Because of the simplicity of creatinine, it is inexpensive, has a very low time and operation cost, and can be easily adapted to automated analysis. As a result, it is very widely used and has been the golden standard for laboratory creatinine measurement. However, Jaffe reaction is known to have low accuracy and insufficient sensitivity[144, 145]. Moreover, some blood factors/organic compounds like glucose, ascorbic acid can induce similar reaction, which makes Jaffe reaction very susceptible to interference.

In recent years, enzymatic assays have emerged as an alternative method for creatinine measurement. As shown below, the reaction mainly involves turning creatinine into creatine and then sarcosine through creatininase and creatinase, and letting sarcosine react with sarcosine oxidase to form hydrogen peroxide (H_2O_2). H_2O_2 can be used as a fluorescence indicator of the creatinine concentration[146].

$$\begin{aligned}
&\text{Creatinine} \xrightleftharpoons{\text{Creatininase}} \textbf{Creatine}\\
&\text{Creatine} \xrightarrow{\text{Creatinase}} \textbf{Sarcosine} + \text{Urea}\\
&\text{Sarcosine} \xrightarrow[\text{Oxidase}]{\text{Sarcosine}} \mathbf{H_2O_2} + \text{HCHO} + \text{Glycine}\\
&H_2O_2 \xrightarrow[\text{UltraRed}]{\text{Amplex}} \textbf{Fluorescence signal}
\end{aligned}$$

Compared to Jaffe reaction, it has better sensitivity and accuracy. More importantly, the enzymatic reaction is more specific to creatinine, meaning that it is more resistant to resistant to interferences[147].

4.1.1.2 Point-of-care creatinine test

Due to the high expense and time consumption of clinical creatinine test, researchers have start to explore the possibility of point-of-care (POC) creatinine test. There have been some successful attempts on the development of a POC creatinine test, but most the researchers chose to build the test based on Jaffe reaction due to its simplicity and low cost, and the test were developed for unary samples only. A study in 2016 introduced a point-of-care device for unary creatinine test using a multi-layer microfluidic device. The device uses a gravitational-capillary valve to control the fluid flow and used a specialized digital camera to capture the color change from Jaffe reaction to measure creatinine[148]. A study in 2022 reported using a paper microfluidic device with the help a raspberry-pi-based digital imaging system to determine Albumin to creatinine ratio in human urine[149].

4.2 Methodology

4.2.1 Fabrication of channel structure on paper

A photo-lithography-based method was used to fabricate channel structure on paper. The process was very similar to the photo-lithography technique for microfluidic device fabrication described in chapter 2.2.1. The design was made in AutoCAD within a circle of 10 cm radius and was printed on transparent film with high resolution. The channel structures were printed on Whatman filter paper (Sigma-Aldrich, St. Louis, MO). The paper was cut to a 10cm radius such that it could match the size of the silicon wafer and was attached on top of the wafer. The 2050 SU-8 (Microchem, Wstborough, MA) was used as the photo-resist, and they were spun on the filter paper for 40 sec at 500 rpm to spread evenly. The filter paper was then pre-baked at 90 °C for 30 min, exposed to UV light for 90 sec, and post-baked at 90 °C for another 30 min. Finally, the filter paper was rinsed in the SU-8 developer, Acetone, and alcohol for 1 h respectively.

4.2.2 Design of paper-microfluidic device

In the project, a paper-microfluidic device was designed to measure creatinine concentration in whole blood. The creatinine measurement assay used for the paper-based device was Jaffe reaction. As mentioned earlier, Jaffe reaction was a colorimetric reaction. The concentration of creatinine was determined how much the color changed from yellow to orange. Since such color change could not be detected in whole blood, blood separation needed to be done prior to the Jaffe reaction assay. As a result, the paper-based device was designed to be a two-layer device that mainly consisted of two regions: the blood separation regions and the reaction region. The bottom layer was made by Grade 3 Whatman filter paper (Cytiva, Marlborough, MA). It was designed to have a 4 mm diameter round chamber for reaction, followed by a 2 mm by 8 mm channel to guide the flow of the liquid. This structure was printed on the filter paper using photo-lithography method. The top layer was made by MF1 Whatman blood separator (Cytiva, Marlborough, MA) which could separate serum from whole blood. It was designed to have a 10mm by 10 mm square area for sample loading, followed by a 2 mm by 34 mm bridge that connected it the reaction zone. The two layers was connected by a 2 mm by 10 mm MF1 blood separator with 5 mm overlapping area with each layer. Fig. 44 shows the overall design of the paper microfluidic device.

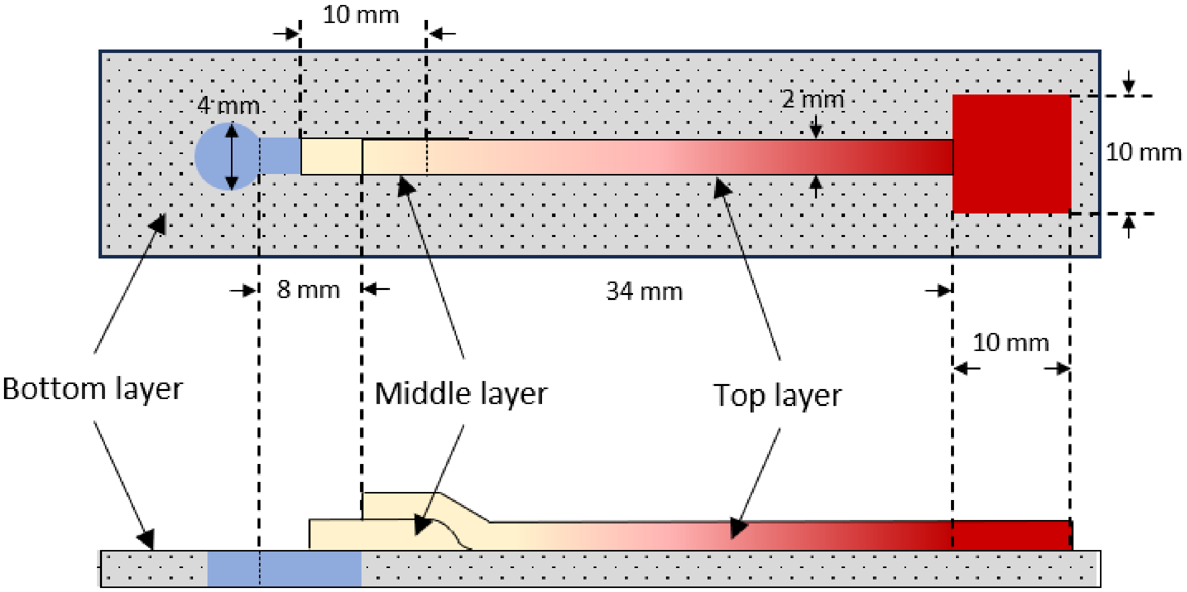

Figure 44. Design of the paper microfluidic device.

4.2.3 Jaffe-reaction-based creatinine assay

As mentioned in the previous chapter, the Jaffe-reaction-based creatinine assay involves letting sample react with Picric Acid under alkaline condition. Picric Acid used in this work was saturated Picric Acid solution (1.3%). It was prepared by adding 0.6 g Picric Acid powder (Thermo Fisher Scientific, Waltham, MA) to 50 mL distilled water. The prepared solution was stored at 4 °C fridge, and would be heated to room temperature every time before the experiment. 1N Sodium Hydroxide solution (Thermo Fisher Scientific, Waltham, MA) was used to create the alkaline environment for the reaction. The stock creatinine solution was prepared by dissolving 50 mg creatinine powder (Thermo Fisher Scientific, Waltham, MA) in 50mL distilled water and stored in 4 °C fridge.

When validating the assay in 96-well plate, standard creatinine samples with concentration of 0.4, 0.8, 1.2, 1.6, 2.4, 3.2, 4.8, 6.4, 9.6, 12.8 and 16 mg/dL were prepared. These samples were created by mixing 100 mg/dL stock creatinine solution of 0.4, 0.8, 1.2, 1.6, 2.4, 3.2, 4.8, 6.4, 9.6, 12.8 and 16 with water of 99.6, 99.2, 98.8, 98.4, 97.6, 96.8, 95.2, 93.6, 90.4, 87.2 and 84. When conducting the experiment, the 15 µL sample would be mixed with 15 µL Sodium Hydroxide first, and added to the well along with 30 µL Picric Acid. Images of the 96 well plate would be taken 5 min later. The images would be transformed from RGB color space to HSV, and the H value would be used to quantify color change.

When validating Jaffe reaction on paper-based device, standard creatinine samples were made by mixing high-concentration creatinine solution with whole blood. The whole blood was taken from mice heart. Under healthy condition, mice serum creatinine concentration can be as low as 0.0565 mg/dL, which is much lower than the serum creatinine concentration of healthy human (0.7 to 1.3 mg/dL for men, 0.6-1.1 mg/dL for women). The creatinine concentration of the whole blood sample would be validated using the enzymatic-based fluorescence assay (detail of the assay will be introduced later) to make sure that the concentration is lower than 0.1 mg/dL. To make standard creatinine samples, the 48 µL of the whole blood sample were mixed with 2 µL of creatinine sample with concentration of 12.5 mg/dL, 25 mg/dL, 50 mg/dL and 100 mg/dL such that the mixed blood samples had creatinine concentration of 0.5 mg/dL, 1 mg/dL, 2 mg/dL, and 4 mg/dL. The 100 mg/dL creatinine samples were made by dissolving 50 mg creatinine powder in 50 mL saline solution to avoid Hemolysis during the experiment. The 50 mg/dL, 25 mg/dL, and 12.5 mg/dL solution were created by applying gradient dilution to the 100 mg/dL creatinine sample. Likewise, the Picric Acid solution was made by dissolving 0.6 g Picric Acid powder in 50 mL saline solution. The bottom layer of the paper device would be soaked in the 1 N Sodium Hydroxide solution for 1 h, and assembled with the rest after the device is dry. The assembled paper device would be contained in a 3-D printed cassette (Fig. 45).

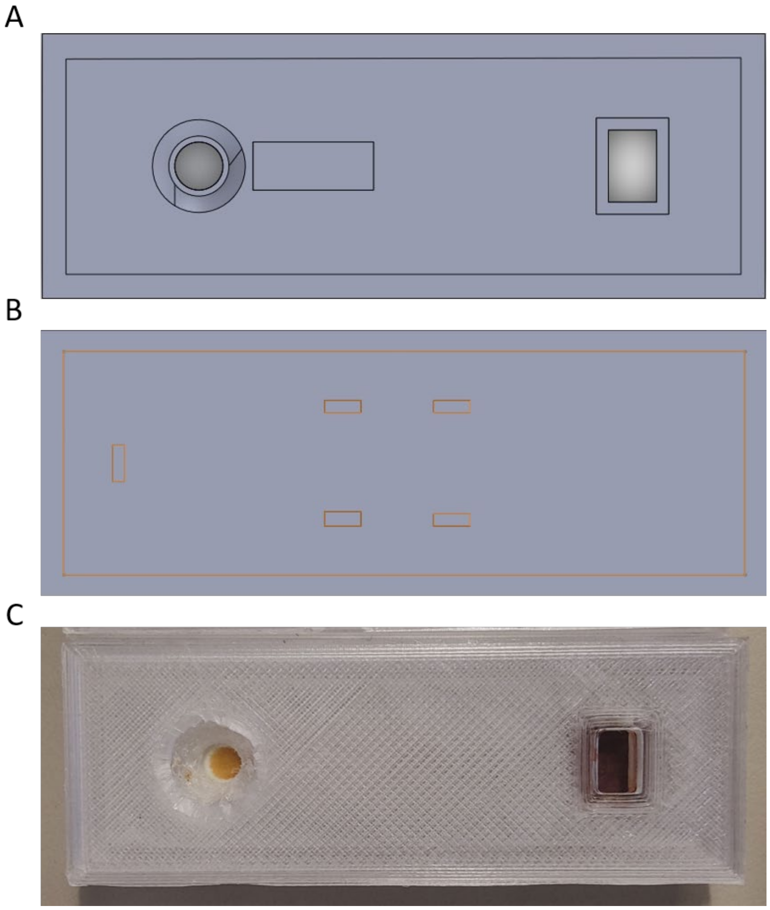

Figure 45. Design of the cassette that is used to hold the paper microfluidic device. **(A)** Lid of the cassette. **(B)** Bottom of the cassette. **(C)** Image of the assembled cassette (with paper microfluidic device loaded in it) taken by smartphone camera.

During the experiment, 50 μL whole blood sample would be pre-mixed with the 30 μL Picric Acid solution, and then added to the inlet of the paper-based device. 15 min after the sample was added, the image of the reaction zone would be taken for analysis. The image would be transformed from RGB channel to HSV channel, and the H value would be used to quantify the color change.

4.2.4 Enzyme-based fluorescence creatinine assay

As mentioned in the previous chapter, the enzyme-based creatinine reaction involves transforming creatinine into creatinine and then sarcosine using creatininase and creatinase respectively, and oxidize sarcosine into Hydrogen Peroxide afterward. Fluorescence signal can be detected when Hydrogen Peroxide is mixed with OxiRed, and the strength of the fluorescence intensity has a linear relationship with the concentration of the Hydrogen Peroxide

The enzyme-based fluorescence assay was developed based on the Creatinine Assay Kit from Abcam (Abcam, Cambridge, UK). The creatinine sample, creatininase, creatinase, and the sarcosine oxidase were all supplied in powder. They were dissolved in 100 µL, 220 µL, 220 µL, 220 µL assay buffer (Tri-HCL buffered NaCl solution containing Bovine serum albumin, bovine gamma globulins, Tween 40 and diethylenetriaminepentaacetic) respectively to make the stock solutions, and stored at -20 °C.

In the assay, serum was separated from the whole blood sample by centrifuging at 1000 g for min. The reaction reagent was prepared by mixing creatininase, creatinase, of sarcosine oxidase, of OxiRed prob (dissolved in DMSO) and assay buffer at ratio of 1:1:1:1:21. In addition to the regular reaction reagent, another also needed to be made for background control. It was done by mixing creatinase, sarcosine oxidase, OxiRed prob and assay buffer at ratio of 1:1:1:22. As compared to the regular reaction reagent, creatininase was excluded from the background control. The purpose of this was to find out the concentration of the Hydrogen Peroxide that are not generated by creatinine through the enzymatic reaction. Standard creatinine samples were made by first diluting the 10 µL of stock solution (100 nmol/L) in 990 µL assay buffer to get 1nmol/L creatinine solution, and then mixing the 0 µL, 6 µL, 12 µL, 18 µL, 24 µL, and 30 µL of 1nmol/L solution with 150 µL, 144 µL, 138 µL, 132 µL, 126 µL, and 120 µL assay buffer respectively. The concentration of the standard creatinine samples would then be 0.45 mg/dL, 0.9 mg/dL, 1.35 mg/dL, 1.8 mg/dL, and 2.25 mg/dL. The enzyme-based fluorescence assay has very high sensitivity, such that the fluorescence intensity of samples with normal creatinine concentration (0.6 mg/dL – 1.3 mg/dL) would exceed the detection range of the fluorescence imaging system. As a result, both the creatinine standards and the serum sample would be diluted by 10 using assay buffer before the experiment. During the experiment, each sample would first be mixed with the regular reaction reagent and the background control reagent respectively. Different from the original assay, 10 µL of sample was mixed with 10 µL of reaction agent in a 3-D printed multi-well plate (details will be introduced in the next paragraph). The plate was then incubated at 37 °C for 1 h. The fluorescence images would be taken at 538 nm/587 nm, and the fluorescence intensity would be used to quantify the creatinine concentration. The final concentration of a sample would be the creatinine concentration of the regular sample subtracted by the one of the background controls.

4.2.5 Design of fluorescence imaging system

The fluorescence imaging system used in this project was similar to the one used in the previous project (Fig. 28) except that no magnification lenses were needed for the smartphone camera to image the multi-well plate.

A specifically designed multi-well plate was inserted to the bottom of the smartphone case (Fig. 46). The plate had a dimension of 75 mm by 20 mm. It contained 3 x 10 wells. The 3 wells in each row can be used to measure one sample, with two being used for duplicate of the regular reading, and one being used for background control reading. The dimension of the well was 4 mm in diameter and 6 mm in depth, meaning that the volume of then well was ~75 µL, which was enough for a 20 µL sample. The bottom of the plate had features for alignment, which would match the alignment features on the bottom of the smartphone case. These features were to make sure that the positions of the wells in the image taken by the camera were consistent.

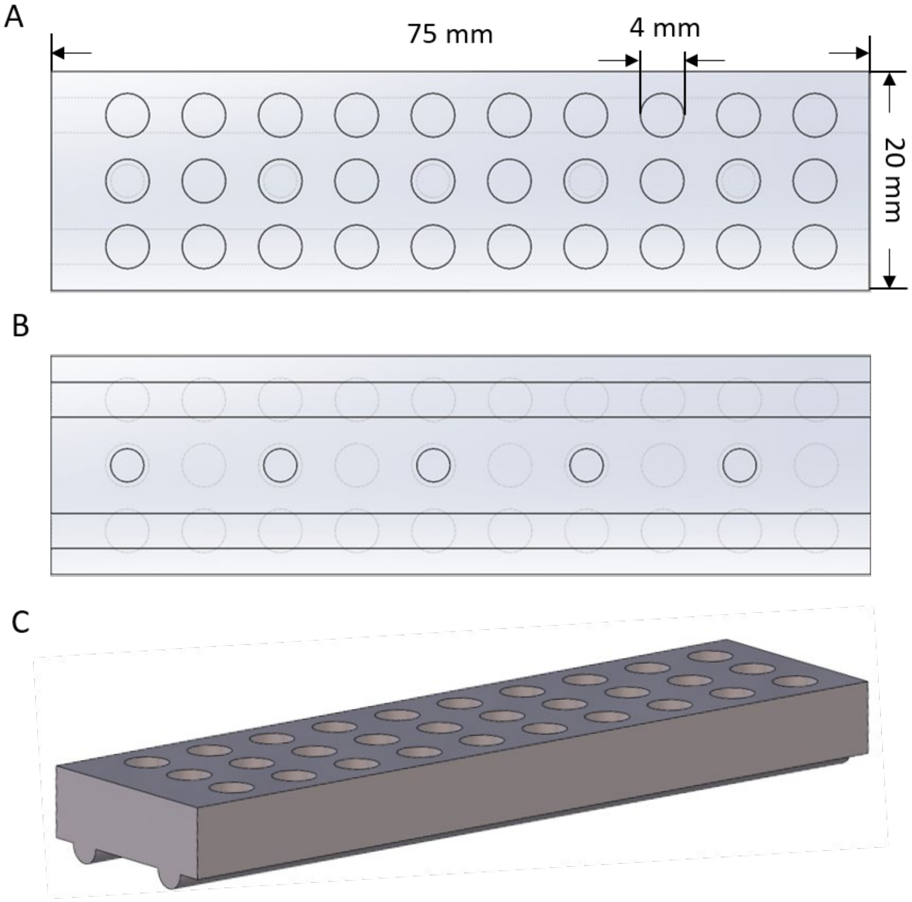

Figure 46. Design of the specifically designed multi-well device. **(A)** Top view of the device. **(B)** Bottom view of the device. **(C)** Overall design of the device.

When analyzing the image, since the fluorescence of the samples were close to orange color, the intensity on red channel was used to represent the strength of fluorescence signal. Thresholding plus k-mean clustering was used to identify and locate wells in the image. Linear regression would be applied to the readings of the standard samples. The fitted line from the linear regression would then be used to calculate the creatinine concentration of unknown samples.

4.3 Result

4.3.1 Result of Jaffe-reaction-based assay

4.3.1.1 Assay validation in 96 well plate

Jaffe-rection-based assay was first tested and validated in 96 well plate. Fig. 47 A shows a representative Jaffe reaction result. When concentration was 0 mg/dL, the color of the well was bright yellow. When concentration increased, the color gradually changed from yellow to orange. Hue in HSV color space was used to quantify this color change as shown in Fig. 47 B. Overall, a straight line could well represent the relationship between the Hue value and the creatinine, with an R^2 of 0.963 and standard error (SE) of 0.0052.

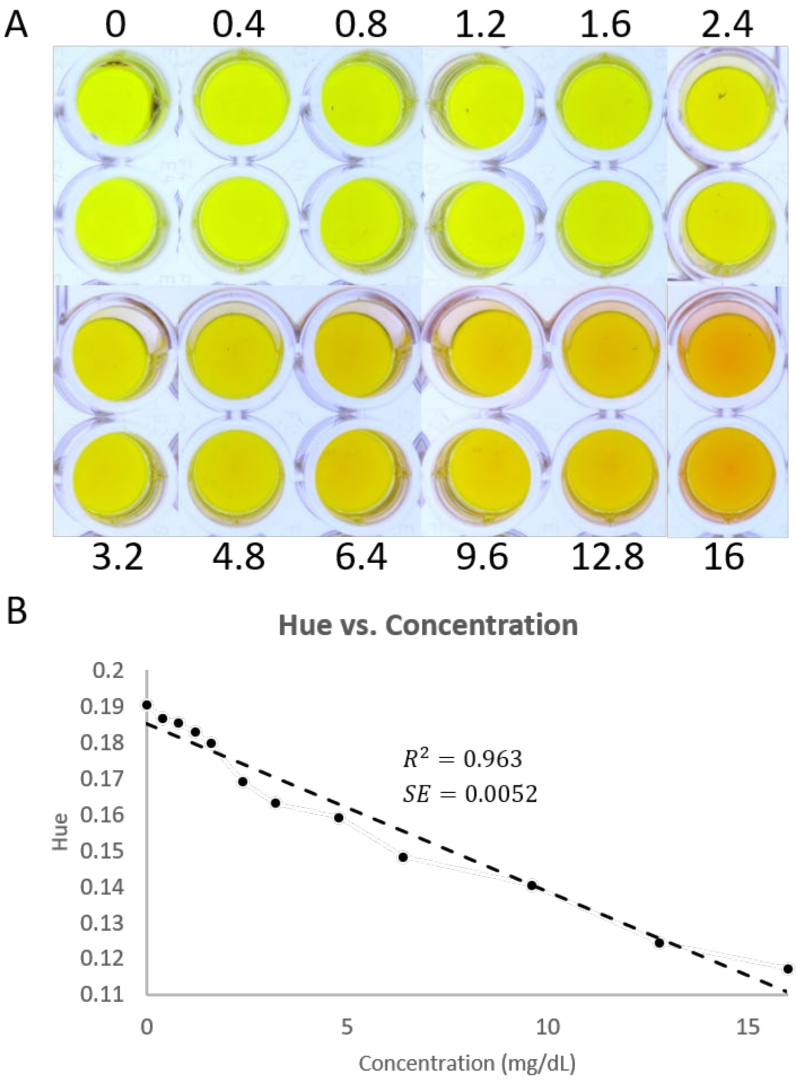

Figure 47. Validation of Jaffe reaction in 96 well plate. **(A)** Image of Jaffe reaction result of standard samples. **(B)** Plot of Hue vs. concentration of the standard samples. A straight line was fitted to the data points.

4.3.1.2 Assay validation on paper using creatinine standards

Jaffe-rection-based assay was then validated on Whatman filter paper using standard samples. First, we validated the assay on paper with only well structure. From the aspect of user friendly, Sodium Hydroxide and Picric Acid should be pre-coated on the paper device, such that the users only need to add the sample when they use it. In Fig. 48, Picric Acid and Sodium Hydroxide was pre-mixed and dropped onto the paper. When the paper dried, samples were added to the paper. As shown in the figure, a negative linear pattern can be observed between Hue value and creatinine concentration. However, the R square value was only 0.771, with a SE of 0.0043, suggesting the linear relationship was relatively low. When looking at samples with lower concentrations (concentration lower than 5 mg/dL), the linear relationship becomes even lower, with the hue values displaying a high degree of variability. One potential cause to such result was that the function of Picric Acid was affected after mixing with Sodium Hydroxide for a long time because of its acidity.

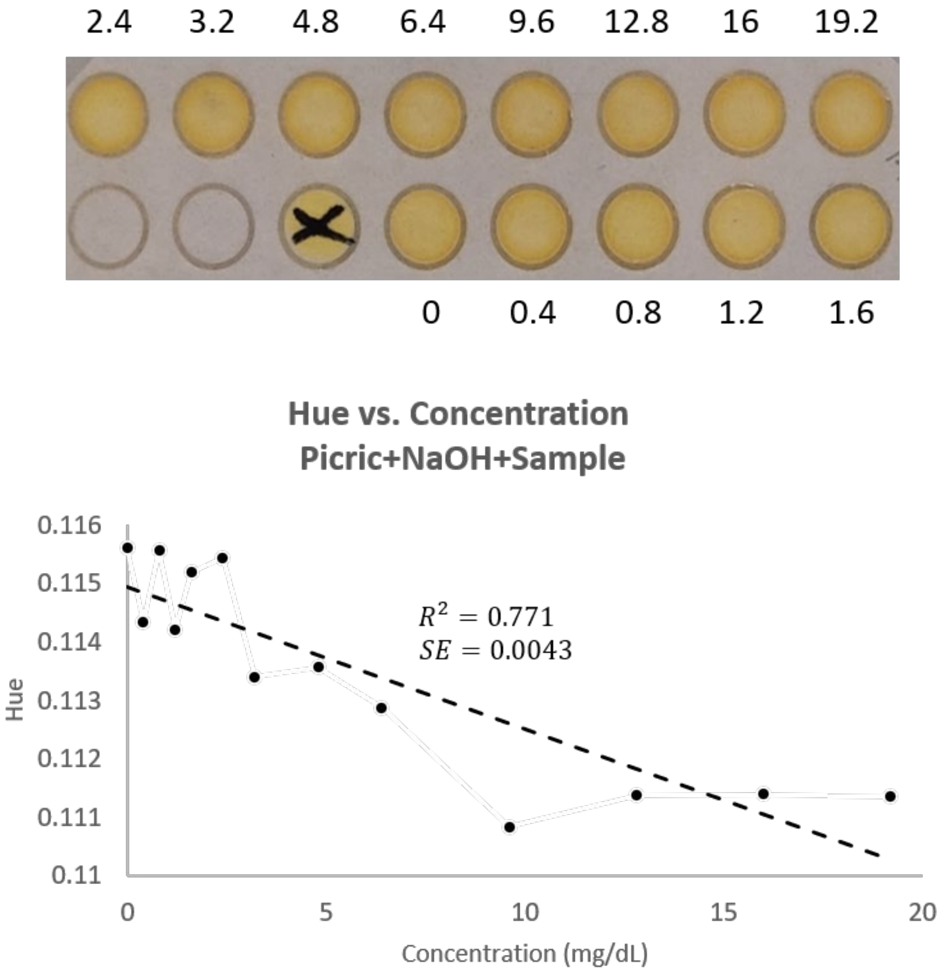

Figure 48. Validation of Jaffe reaction on Whatman filter paper. Picric acid, Sodium Hydroxide, and creatinine samples were added sequentially to the paper. **(A)** Image of Jaffe reaction result of standard samples. **(B)** Plot of Hue vs. concentration of the standard samples. A straight line was fitted to the data points.

To avoid Picric Acid and Sodium Hydroxide from long-time mixing, Sodium Hydroxide was pre-coated onto the paper by dipping the paper in Sodium Hydroxide for 1 h. Picric Acid was pre-mixed with the sample, and then dropped onto the paper (Fig. 49). As shown in the figure, the Hue value and the creatinine concentration had a much better linear relationship. The R square was increased to 0.974. The SE was 0.0017 which was much smaller. However, with concentration of 0 mg/dL, 0.4 mg/dL and 0.8 mg/dL, the Hue value still exhibited a relatively random pattern. This indicated that the assay might still not work very well for low concentration samples (< 1 mg/dL).

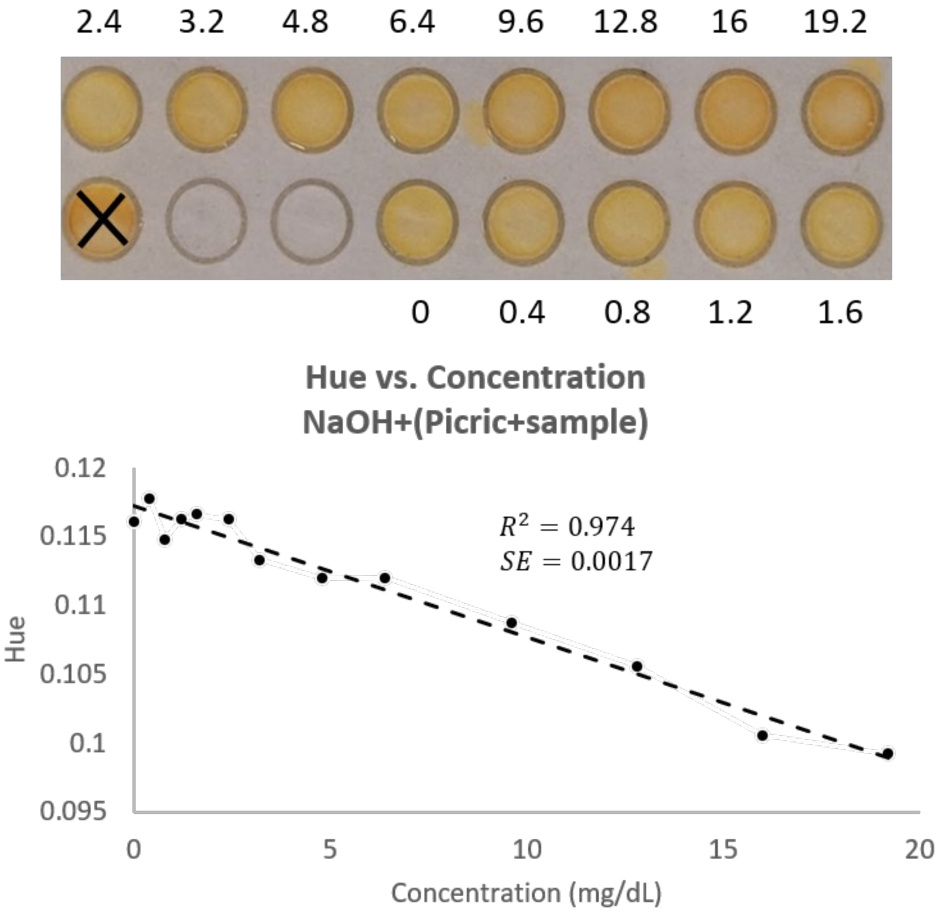

Figure 49. Validation of Jaffe reaction on Whatman filter paper. Sodium Hydroxide was pre-coated on the paper. The mix of Picric acid and creatinine samples were then added to the paper. **(A)** Image of Jaffe reaction result of standard samples. **(B)** Plot of Hue vs. concentration of the standard samples. A straight line was fitted to the data points.

To further validate whether blood separation membrane or long-distance liquid diffusion would have any effect on the Jaffe-reaction assay, a similar test was done using the multi-layer paper device (Fig. 50). As shown in the figure, the R square value of the linear regression is 0.987, with a SE of 0.00034. This indicated that there was a strong linear relationship between Hue value and creatinine concentration, meaning blood separation membrane or long-distance liquid diffusion do not have effect on Jaffe-reaction assay.

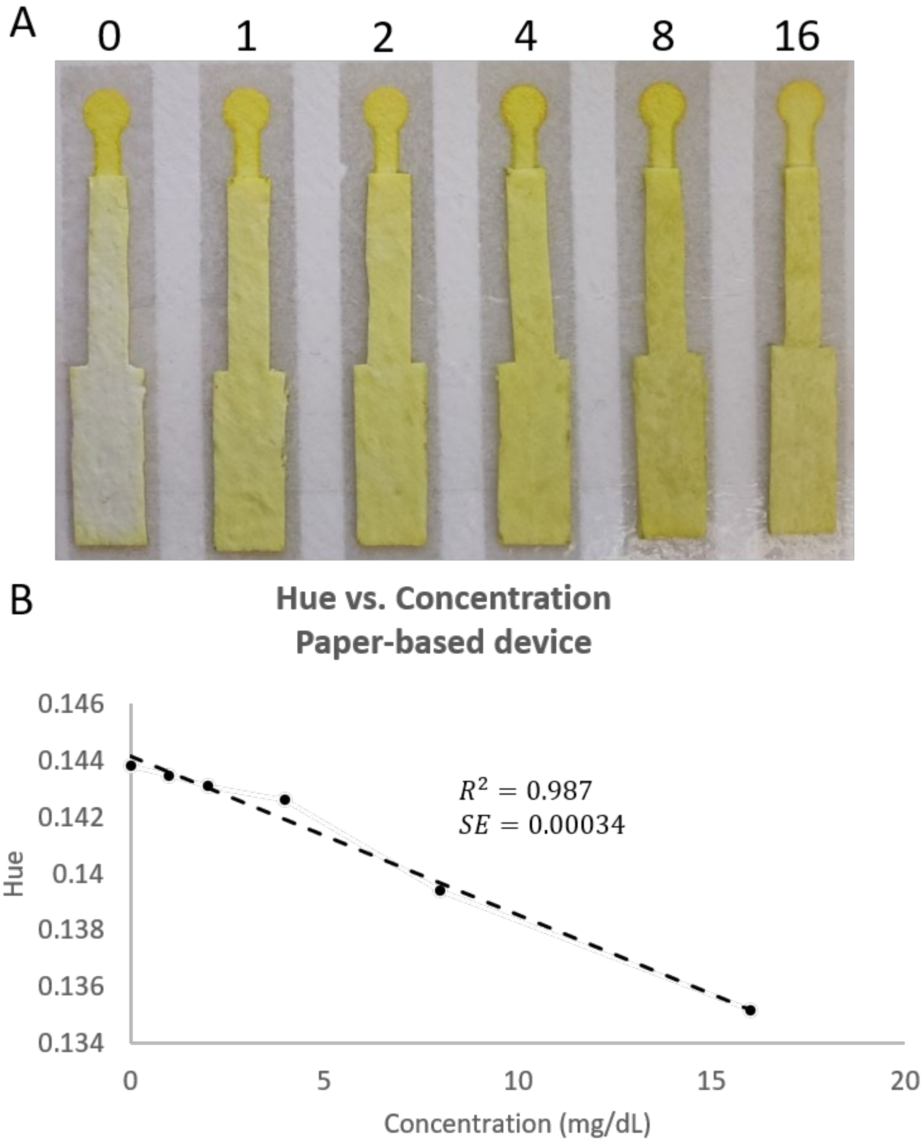

Figure 50. Validation of the effect of blood separation membrane and long-distance diffusion on Jaffe reaction. **(A)** Image of Jaffe reaction result of standard samples. **(B)** Plot of Hue vs. concentration of the standard samples. A straight line was fitted to the data points.

4.3.1.3 Assay validation on paper using whole blood samples

Fig. 51 shows the validation result of whole blood samples on the paper-based device. Overall, the blood separation membrane trapped most of the red blood cells, and the separated serum along with Picric Acid successfully diffused to the reaction well on the bottom layer. The hue value and the creatinine concentration exhibited a linear relationship, with R square of 0.952, and SE of 0.0012. Compared to the validation result with standard samples, the color of the reaction result for whole blood was darker (closer to orange). This was caused by the fact that serum separated from normally had yellow color. This could cause the color of the sample with high concentration to saturate, which could explain the fact that the hue value of high concentration sample (16 mg/dL) was higher than expected.

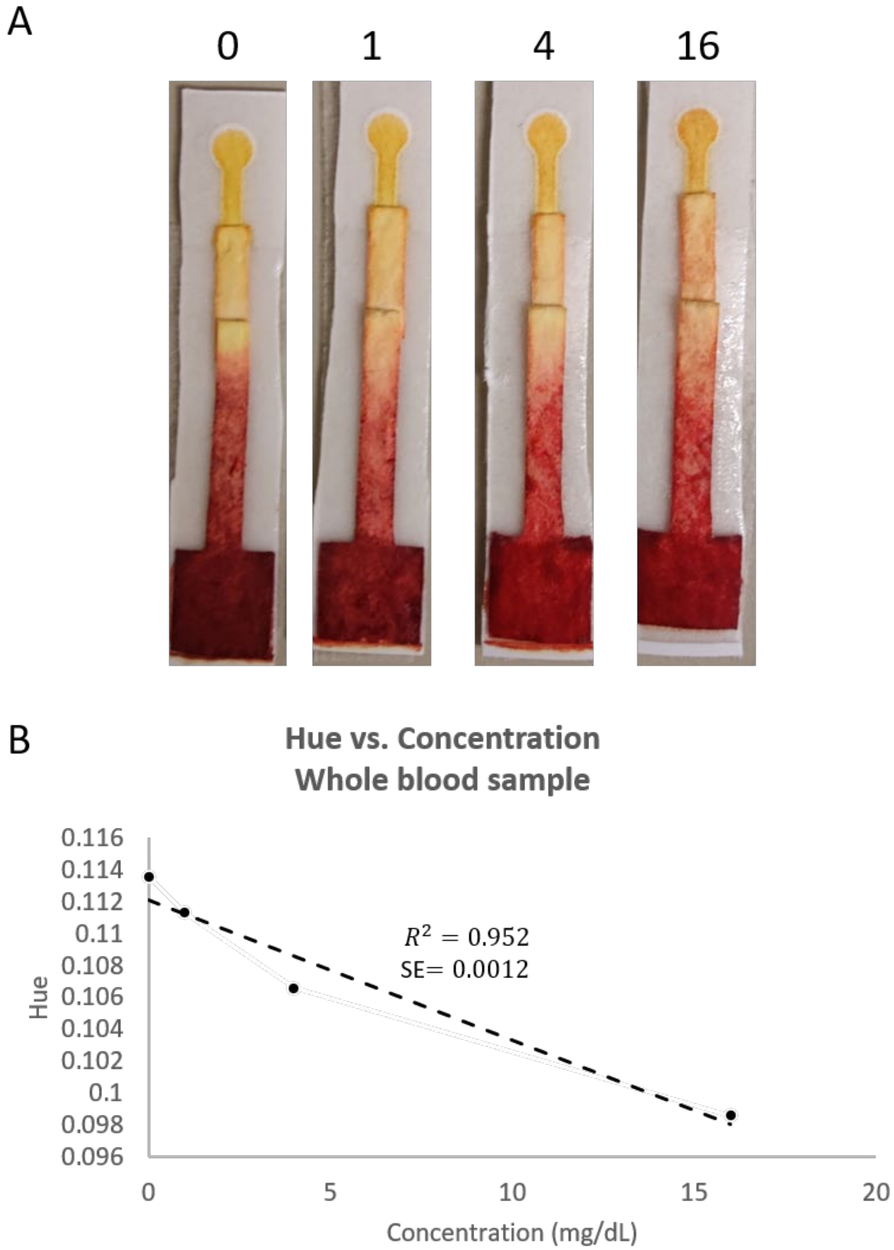

Figure 51. Validation of paper microfluidic device using whole blood samples. **(A)** Image of testing result of standard samples. **(B)** Plot of Hue vs. concentration of the standard samples. A straight line was fitted to the data points.

4.3.2 Result of Enzyme-based fluorescence assay

Fig. 52 shows a representative result on performing the enzyme-based fluorescence assay on standard samples. As shown in the figure, the fluorescence intensity increased when creatinine concentration was higher, and there was a strong linear relationship between the two with a R square value of 0.993.

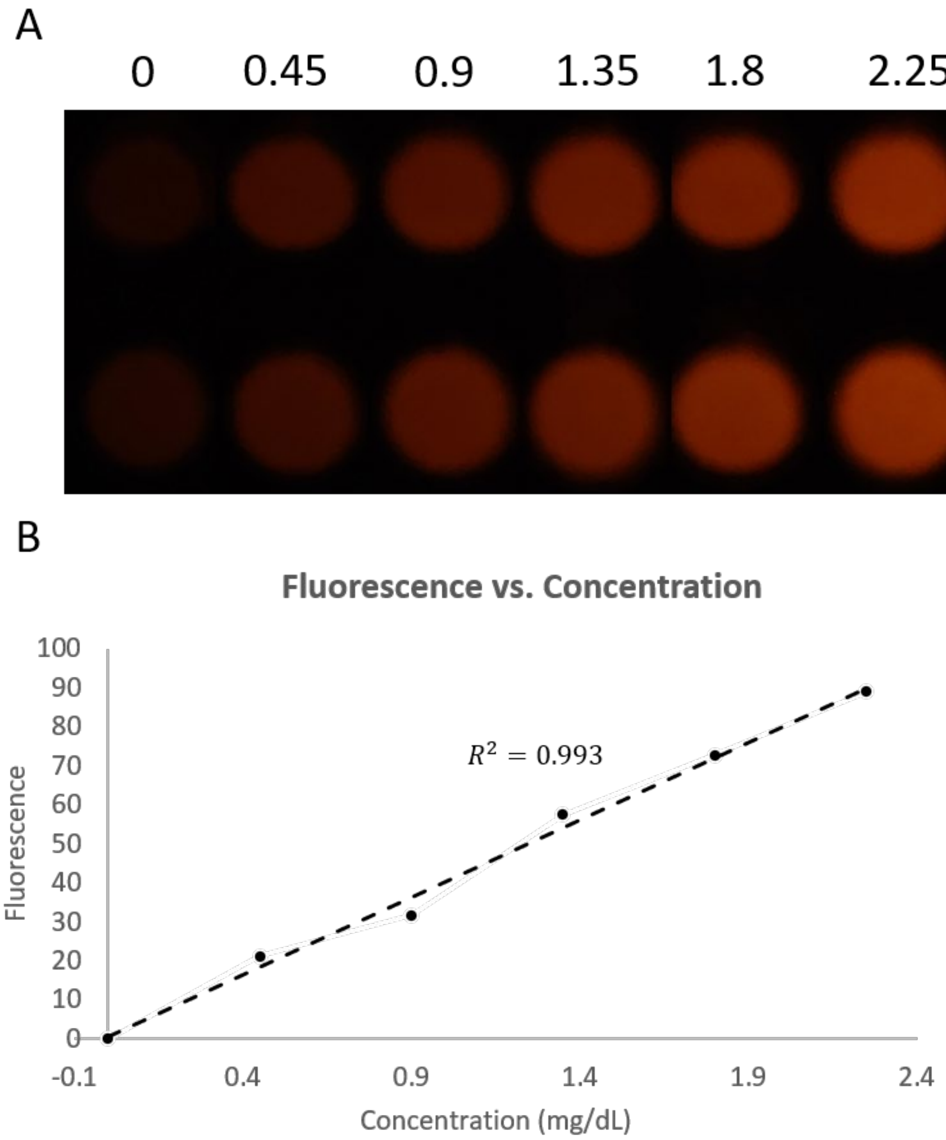

Figure 52. Representative result of enzymatic fluorescence assay for creatinine measurement. **(A)** Fluorescence image of enzymatic assay result of standard samples. **(B)** Plot of fluorescence vs. concentration of the standard samples. A straight line was fitted to the data points.

30 human samples were then used to validate the enzyme-based fluorescence assay. The results measured by the enzyme-based fluorescence assay were compared to the clinical data (Fig. 53).

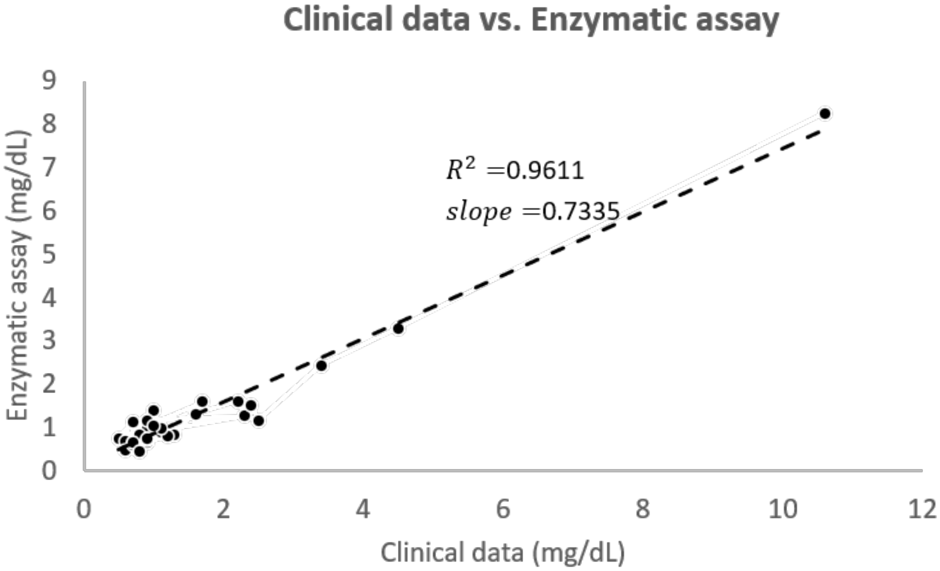

Figure 53. Validation of enzymatic fluorescence creatinine assay on human samples.

As shown in the figure, the enzymatic assay's result and the clinical data were linearly correlated, with an R square value of 0.9611. However, the enzymatic assay's readings were mostly lower than the clinical data (slope of the fitted line was 0.7335). This could be explained by the fact that clinical data were collected using Jaffe reaction, and Jaffe reaction has been reported to have higher readings and is vulnerable to interferences.

4.3.3 Conclusion

In this project, we attempted to build two assays for easy and fast serum creatinine measurement. The first assay was built based on Jaffe reaction. We successfully implemented the assay on paper-based device, which makes it possible for POC testing. We validated the assay using artificial whole blood samples (mix of mice whole blood samples and high concentration creatinine solution), and the results showed strong correlation between concentration and color changes. The second assay was built based on enzyme-based fluorescence assay. Due to the complexity of the reaction, we only managed to perform the assay using a smartphone-based fluorescence imaging system with a specifically designed multi-well plate. However, the assay exhibited a much higher sensitivity as compared to Jaffe-reaction-based assay. Also, we validated the assay on 30 human samples. Although the readings from the enzymatic assay were mostly lower than the clinical data, the two sets of readings were strongly linearly correlated.

Both the assays are still in the early development stage. For Jaffe-reaction-based assay, more optimization still needs to be done to increase the sensitivity for samples with low concentration (< 1 mg/dL). Also, the assay needs to be validated on more mice whole blood samples, and eventually validated on human samples. The Enzyme-based fluorescence assay on the other side, also needs to be validated on more human samples. Also, more efforts can be put to look into the potential of implementing the assay on paper-based device to achieve POC testing.

CHAPTER 5. Conclusion, Discussion and Future Direction

In this thesis, we described three projects. In the first project, we built a smartphone-fluidic digital imaging (SFDIA) system to assess the islets mass in preparation for islet transplantation. The system managed to generate islet quantity results as well as parameters beyond traditional mass quantification (volume, purity and morphology). Several limitations of the system still need to be mentioned**.** First, due to the relatively low resolution and recording frame rate of the smartphone camera, a consistent fluid flow is required for our video processing to assure a reliable reading of islet parameters. Therefore, the system requires the use of an external pump system to deliver consistent fluid flow through the microfluidic channel. To upgrade the current system and overcome this issue, a customized camera is favorable. With the upgrade, it is also possible to simplify the experimental setup by removing the external power source for fluid delivery and utilize a pumpless microfluidic system as we introduced previously for islet function tests. Another limitation of our methodology is that the imaging is captured in 2D, but the islet mass parameters are dependent on the 3D structure of the islets. Although our system is simple and has significant advantages over traditional manual counting in acquiring the most useful parameters from islet samples, we believe that a 3D scanning and modeling approach can further improve the accuracy.

In the second project, we integrate fluorescence imaging capability into the SFDIA system. As a result, we managed to use the system to study insulin secretion kinetics of islet beta-cells with easy operations and low cost. One limitation with the current system setup is that the current setup can only work with one fluorescence spectrum at a time. However, this problem can be resolved in the future by implementing filter switch functionality into the system with the help of a motorized filter wheel. Another limitation was that result generated from the system was not a quantification result that can be easily understood. This result still needs to be interpreted by experts to reflect the functionality of islets. So, another future direction for the project will be to incorporate the concepts of big data and machine learning to transform the system into a front-end device for islet data gathering, while embedding a fully trained analysis model such that the system can generate assistive results on cell functionality.

In the third project, we tried to different methods to measure creatinine concentration at low cost and time consumption. We built a paper-based POC device based on Jaffe reaction, and implemented an enzymatic fluorescence assay with the help of the SFDIA system. Although we have had some successful validation on both methods, we still need to validate them with more samples. For the Jaffe-reaction-based method, more optimization needs to be done to increase the sensitivity for samples with low concentration (< 1 mg/dL). For the enzyme-based fluorescence assay, attempts need to be made to migrate the assay onto paper-based device to achieve POC testing.

REFERENCES

1. Katsarou, A., et al., *Type 1 diabetes mellitus.* Nat Rev Dis Primers, 2017. **3**: p. 17016.
2. Nolan, C., et al., *The structure of bovine proinsulin.* J Biol Chem, 1971. **246**(9): p. 2780-95.
3. Vasiljevic, J., et al., *The making of insulin in health and disease.* Diabetologia, 2020. **63**(10): p. 1981-1989.
4. Berger, C. and D. Zdzieblo, *Glucose transporters in pancreatic islets.* Pflugers Arch, 2020. **472**(9): p. 1249-1272.
5. Atkinson, M.A., G.S. Eisenbarth, and A.W. Michels, *Type 1 diabetes.* Lancet, 2014. **383**(9911): p. 69-82.
6. Chatterjee, S., K. Khunti, and M.J. Davies, *Type 2 diabetes.* Lancet, 2017. **389**(10085): p. 2239-2251.
7. *By the Numbers: Diabetes in America*, C.f.D.C.a. Prevention, Editor. 2022.
8. *Type 1 diabetes*. 2023; Available from: https://www.mayoclinic.org/diseases-conditions/type-1-diabetes/diagnosis-treatment/drc-20353017.
9. *Just Diagnosed With Type 1 Diabetes*. 2023; Available from: https://www.cdc.gov/diabetes/basics/diabetes-type-1-diagnosis.html.
10. Pathak, V., et al., *Therapies for Type 1 Diabetes: Current Scenario and Future Perspectives.* Clin Med Insights Endocrinol Diabetes, 2019. **12**: p. 1179551419844521.
11. Vajo, Z., J. Fawcett, and W.C. Duckworth, *Recombinant DNA technology in the treatment of diabetes: insulin analogs.* Endocr Rev, 2001. **22**(5): p. 706-17.
12. Cobelli, C., E. Renard, and B. Kovatchev, *Artificial pancreas: past, present, future.* Diabetes, 2011. **60**(11): p. 2672-82.
13. Funnell, M.M., *Overcoming barriers to the initiation of insulin therapy.* Clinical Diabetes, 2007. **25**(1): p. 36-39.
14. Mullard, A., *FDA approves first cell therapy for type 1 diabetes.* Nat Rev Drug Discov, 2023. **22**(8): p. 611.
15. McCallion, O., et al., *Regulatory T-cell therapy approaches.* Clin Exp Immunol, 2023. **211**(2): p. 96-107.
16. Shapiro, A.M., M. Pokrywczynska, and C. Ricordi, *Clinical pancreatic islet transplantation.* Nat Rev Endocrinol, 2017. **13**(5): p. 268-277.
17. Carter, J.D., et al., *A practical guide to rodent islet isolation and assessment.* Biol Proced Online, 2009. **11**: p. 3-31.
18. Ricordi, C. and T.B. Strom, *Clinical islet transplantation: advances and immunological challenges.* Nat Rev Immunol, 2004. **4**(4): p. 259-68.
19. Yeo, C.J., *Shackelford's surgery of the alimentary tract, e-book*. 2017: Elsevier Health Sciences.
20. Hricik, D.E., *Steroid-free immunosuppression in kidney transplantation: an editorial review.* Am J Transplant, 2002. **2**(1): p. 19-24.
21. Ryan, E.A., et al., *Five-year follow-up after clinical islet transplantation.* Diabetes, 2005. **54**(7): p. 2060-9.
22. Qi, M., et al., *Five-year follow-up of patients with type 1 diabetes transplanted with allogeneic islets: the UIC experience.* Acta Diabetol, 2014. **51**(5): p. 833-43.

23. Shapiro, A.M., et al., *International trial of the Edmonton protocol for islet transplantation.* N Engl J Med, 2006. **355**(13): p. 1318-30.
24. Hering, B.J., et al., *Phase 3 Trial of Transplantation of Human Islets in Type 1 Diabetes Complicated by Severe Hypoglycemia.* Diabetes Care, 2016. **39**(7): p. 1230-40.
25. Li, M. and S. Ikehara, *Stem cell treatment for type 1 diabetes.* Front Cell Dev Biol, 2014. **2**: p. 9.
26. Gravesen, P., J. Branebjerg, and O.S. Jensen, *Microfluidics-a review.* Journal of micromechanics and microengineering, 1993. **3**(4): p. 168.
27. Beebe, D.J., G.A. Mensing, and G.M. Walker, *Physics and applications of microfluidics in biology.* Annu Rev Biomed Eng, 2002. **4**: p. 261-86.
28. Lee, C.-S., *Grand challenges in microfluidics: a call for biological and engineering action*. 2020, Frontiers Media SA. p. 583035.
29. Bae, C.W., et al., *Fully Stretchable Capillary Microfluidics-Integrated Nanoporous Gold Electrochemical Sensor for Wearable Continuous Glucose Monitoring.* ACS Appl Mater Interfaces, 2019. **11**(16): p. 14567-14575.
30. Khizar, S., et al., *Magnetic nanoparticles in microfluidic and sensing: From transport to detection.* Electrophoresis, 2020. **41**(13-14): p. 1206-1224.
31. Shembekar, N., et al., *Single-Cell Droplet Microfluidic Screening for Antibodies Specifically Binding to Target Cells.* Cell Rep, 2018. **22**(8): p. 2206-2215.
32. Huh, D., et al., *Reconstituting organ-level lung functions on a chip.* Science, 2010. **328**(5986): p. 1662-8.
33. Sia, S.K. and G.M. Whitesides, *Microfluidic devices fabricated in poly(dimethylsiloxane) for biological studies.* Electrophoresis, 2003. **24**(21): p. 3563-76.
34. Gao, B., et al., *Emerging paper microfluidic devices.* Analyst, 2019. **144**(22): p. 6497-6511.
35. Yang, Y., et al., *Paper-Based Microfluidic Devices: Emerging Themes and Applications.* Anal Chem, 2017. **89**(1): p. 71-91.
36. Bhakta, S.A., et al., *Determination of nitrite in saliva using microfluidic paper-based analytical devices.* Anal Chim Acta, 2014. **809**: p. 117-22.
37. Li, X., K. Scida, and R.M. Crooks, *Detection of hepatitis B virus DNA with a paper electrochemical sensor.* Anal Chem, 2015. **87**(17): p. 9009-15.
38. Kang, B.-H., M. Park, and K.-H. Jeong, *Colorimetric Schirmer strip for tear glucose detection.* BioChip Journal, 2017. **11**: p. 294-299.
39. Chowdury, M.A. and F. Khalid, *Application of microfluidic paper-based analytical device (muPAD) to detect COVID-19 in energy deprived countries.* Int J Energy Res, 2021. **45**(12): p. 18275-18280.
40. Mustafa, F., R.Y.A. Hassan, and S. Andreescu, *Multifunctional Nanotechnology-Enabled Sensors for Rapid Capture and Detection of Pathogens.* Sensors (Basel), 2017. **17**(9).
41. Tang, R., et al., *A fully disposable and integrated paper-based device for nucleic acid extraction, amplification and detection.* Lab Chip, 2017. **17**(7): p. 1270-1279.
42. Xia, Y., J. Si, and Z. Li, *Fabrication techniques for microfluidic paper-based analytical devices and their applications for biological testing: A review.* Biosensors and Bioelectronics, 2016. **77**: p. 774-789.
43. Anushka, A. Bandopadhyay, and P.K. Das, *Paper based microfluidic devices: a review of fabrication techniques and applications.* Eur Phys J Spec Top, 2023. **232**(6): p. 781-815.
44. Nie, J., et al., *One-step patterning of hollow microstructures in paper by laser cutting to create microfluidic analytical devices.* Analyst, 2013. **138**(2): p. 671-6.

45. Altundemir, S., A.K. Uguz, and K. Ulgen, *A review on wax printed microfluidic paper-based devices for international health.* Biomicrofluidics, 2017. **11**(4): p. 041501.
46. Ballerini, D.R., X. Li, and W. Shen, *Patterned paper and alternative materials as substrates for low-cost microfluidic diagnostics.* Microfluidics and nanofluidics, 2012. **13**: p. 769-787.
47. Songjaroen, T., et al., *Novel, simple and low-cost alternative method for fabrication of paper-based microfluidics by wax dipping.* Talanta, 2011. **85**(5): p. 2587-93.
48. Jiang, Z., et al., *Extrusion 3D Printing of Polymeric Materials with Advanced Properties.* Adv Sci (Weinh), 2020. **7**(17): p. 2001379.
49. Abe, K., et al., *Inkjet-printed paperfluidic immuno-chemical sensing device.* Anal Bioanal Chem, 2010. **398**(2): p. 885-93.
50. Martinez, A.W., et al., *FLASH: a rapid method for prototyping paper-based microfluidic devices.* Lab Chip, 2008. **8**(12): p. 2146-50.
51. He, Q., et al., *Method for fabrication of paper-based microfluidic devices by alkylsilane self-assembling and UV/O3-patterning.* Anal Chem, 2013. **85**(3): p. 1327-31.
52. *Whatman blood separators for lateral flow immunoassay*. Available from: https://www.cytivalifesciences.com/en/us/solutions/lab-filtration/knowledge-center/blood-separators.
53. Songjaroen, T., et al., *Blood separation on microfluidic paper-based analytical devices.* Lab Chip, 2012. **12**(18): p. 3392-8.
54. Laofor, C. and V. Peansupap, *Defect detection and quantification system to support subjective visual quality inspection via a digital image processing: A tiling work case study.* Automation in Construction, 2012. **24**: p. 160-174.
55. Danti, A., J.Y. Kulkarni, and P. Hiremath, *An image processing approach to detect lanes, pot holes and recognize road signs in Indian roads.* International Journal of Modeling and Optimization, 2012. **2**(6): p. 658.
56. Saladi, S. and N.A. Prabha, *A Comprehensive Review: Segmentation of MRI Images-Brain Tumor.* International Journal of Imaging Systems and Technology, 2016. **26**(4): p. 295-304.
57. Madabhushi, A. and G. Lee, *Image analysis and machine learning in digital pathology: Challenges and opportunities.* Med Image Anal, 2016. **33**: p. 170-175.
58. McCracken, K.E. and J.Y. Yoon, *Recent approaches for optical smartphone sensing in resource-limited settings: a brief review.* Analytical Methods, 2016. **8**(36): p. 6591-6601.
59. Lee, S.A., et al., *Color capable sub-pixel resolving optofluidic microscope and its application to blood cell imaging for malaria diagnosis.* PLoS One, 2011. **6**(10): p. e26127.
60. Gmyr, V., et al., *Automated Digital Image Analysis of Islet Cell Mass Using Nikon's Inverted Eclipse Ti Microscope and Software to Improve Engraftment May Help to Advance the Therapeutic Efficacy and Accessibility of Islet Transplantation Across Centers.* Cell Transplantation, 2015. **24**(1): p. 1-9.
61. Manos, A., T. Hazan, and I. Klein, *Walking Direction Estimation Using Smartphone Sensors: A Deep Network-Based Framework.* Ieee Transactions on Instrumentation and Measurement, 2022. **71**.
62. Banik, S., et al., *Recent trends in smartphone-based detection for biomedical applications: a review.* Anal Bioanal Chem, 2021. **413**(9): p. 2389-2406.
63. Atchison, D.A., *Objective refraction.* Optometry: Science, Techniques and Clinical Management. Second Edition. Butterworth Heinemann Elsevier, 2009. **13**: p. 187-208.

64. Helmenstine, A. *Fluorescence Definition and Examples*. 2023; Available from: https://sciencenotes.org/fluorescence-definition-and-examples/.
65. Herzenberg, L.A., R.G. Sweet, and L.A. Herzenberg, *Fluorescence-activated cell sorting.* Sci Am, 1976. **234**(3): p. 108-17.
66. Odell, I.D. and D. Cook, *Immunofluorescence techniques.* The Journal of investigative dermatology, 2013. **133**(1): p. e4.
67. Wang, X. and Y. Lai. *Three basic types of fluorescence microscopy and recent improvement*. in *E3S Web of Conferences*. 2021. EDP Sciences.
68. Chandel, R. and G. Gupta, *Image filtering algorithms and techniques: A review.* International Journal of Advanced Research in Computer Science and Software Engineering, 2013. **3**(10).
69. Ziou, D. and S. Tabbone, *Edge detection techniques-an overview.* Pattern Recognition and Image Analysis C/C of Raspoznavaniye Obrazov I Analiz Izobrazhenii, 1998. **8**: p. 537-559.
70. Lyvers, E.P. and O.R. Mitchell, *Precision Edge Contrast and Orientation Estimation.* Ieee Transactions on Pattern Analysis and Machine Intelligence, 1988. **10**(6): p. 927-937.
71. Prewitt, J.M., *Object enhancement and extraction.* Picture processing and Psychopictorics, 1970. **10**(1): p. 15-19.
72. Canny, J., *A Computational Approach to Edge-Detection.* Ieee Transactions on Pattern Analysis and Machine Intelligence, 1986. **8**(6): p. 679-698.
73. Nussbaumer, H.J. and H.J. Nussbaumer, *The fast Fourier transform*. 1982: Springer.
74. Robinson, E.A. and S. Treitel, *Principles of digital Wiener filtering.* Geophysical Prospecting, 1967. **15**(3): p. 311-332.
75. Selesnick, I.W. and C.S. Burrus, *Generalized digital Butterworth filter design.* Ieee Transactions on Signal Processing, 1998. **46**(6): p. 1688-1694.
76. Serra, J. and L. Vincent, *An Overview of Morphological Filtering.* Circuits Systems and Signal Processing, 1992. **11**(1): p. 47-108.
77. Mutlag, W.K., et al. *Feature extraction methods: a review*. in *Journal of Physics: Conference Series*. 2020. IOP Publishing.
78. Umamaheswari, C., R. Bhavani, and D.K.T. Sikamani, *Texture and color feature extraction from ceramic tiles for various flaws detection classification.* International Journal on Future Revolution in Computer Science & Communication Engineering, 2018. **4**(1): p. 169-179.
79. Lowe, D.G. *Object recognition from local scale-invariant features*. in *Proceedings of the seventh IEEE international conference on computer vision*. 1999. Ieee.
80. Aly, A.A., S.B. Deris, and N. Zaki, *Research review for digital image segmentation techniques.* International Journal of Computer Science & Information Technology, 2011. **3**(5): p. 99.
81. Kuruvilla, J., et al., *A Review on Image Processing and Image Segmentation.* Proceedings of 2016 International Conference on Data Mining and Advanced Computing (Sapience), 2016: p. 198-203.
82. Xu, X.Y., et al., *Characteristic analysis of Otsu threshold and its applications.* Pattern Recognition Letters, 2011. **32**(7): p. 956-961.
83. Likas, A., N. Vlassis, and J.J. Verbeek, *The global -means clustering algorithm.* Pattern Recognition, 2003. **36**(2): p. 451-461.

84. Lu, D. and Q. Weng, *A survey of image classification methods and techniques for improving classification performance.* International Journal of Remote Sensing, 2007. **28**(5): p. 823-870.
85. Wold, S., K. Esbensen, and P. Geladi, *Principal Component Analysis.* Chemometrics and Intelligent Laboratory Systems, 1987. **2**(1-3): p. 37-52.
86. Balakrishnama, S. and A. Ganapathiraju, *Linear discriminant analysis-a brief tutorial.* Institute for Signal and information Processing, 1998. **18**(1998): p. 1-8.
87. Reynolds, D.A., *Gaussian mixture models.* Encyclopedia of biometrics, 2009. **741**(659-663).
88. Murtagh, F. and P. Contreras, *Algorithms for hierarchical clustering: an overview.* Wiley Interdisciplinary Reviews-Data Mining and Knowledge Discovery, 2012. **2**(1): p. 86-97.
89. Myles, A.J., et al., *An introduction to decision tree modeling.* Journal of Chemometrics, 2004. **18**(6): p. 275-285.
90. Biau, G. and E. Scornet, *A random forest guided tour.* Test, 2016. **25**: p. 197-227.
91. Noble, W.S., *What is a support vector machine?* Nature Biotechnology, 2006. **24**(12): p. 1565-1567.
92. Yilmaz, A., O. Javed, and M. Shah, *Object tracking: A survey.* Acm Computing Surveys, 2006. **38**(4).
93. Welch, G. and G. Bishop, *An introduction to the Kalman filter.* 1995.
94. Djuric, P.M., et al., *Particle filtering.* Ieee Signal Processing Magazine, 2003. **20**(5): p. 19-38.
95. Tang, D. and Y.-J. Zhang. *Combining mean-shift and particle filter for object tracking*. in *2011 Sixth International Conference on Image and Graphics*. 2011. IEEE.
96. LeCun, Y., Y. Bengio, and G. Hinton, *Deep learning.* Nature, 2015. **521**(7553): p. 436-444.
97. Albawi, S., T.A. Mohammed, and S. Al-Zawi, *Understanding of a Convolutional Neural Network.* 2017 International Conference on Engineering and Technology (Icet), 2017.
98. Lipton, Z.C., J. Berkowitz, and C. Elkan, *A critical review of recurrent neural networks for sequence learning.* arXiv preprint arXiv:1506.00019, 2015.
99. Xiong, Z.H., et al., *ECG signal classification for the detection of cardiac arrhythmias using a convolutional recurrent neural network.* Physiological Measurement, 2018. **39**(9).
100. Koch, P., et al., *A Recurrent Neural Network for Hand Gesture Recognition based on Accelerometer Data.* 2019 41st Annual International Conference of the Ieee Engineering in Medicine and Biology Society (Embc), 2019: p. 5088-5091.
101. Vaswani, A., et al., *Attention Is All You Need.* Advances in Neural Information Processing Systems 30 (Nips 2017), 2017. **30**.
102. Naveed, H., et al., *A comprehensive overview of large language models.* arXiv preprint arXiv:2307.06435, 2023.
103. Shapiro, A.M., et al., *Islet transplantation in seven patients with type 1 diabetes mellitus using a glucocorticoid-free immunosuppressive regimen.* N Engl J Med, 2000. **343**(4): p. 230-8.
104. Wang, Y., et al., *Systematic analysis of donor and isolation factor's impact on human islet yield and size distribution.* Cell Transplant, 2013. **22**(12): p. 2323-33.
105. Buchwald, P., et al., *Quantitative assessment of islet cell products: estimating the accuracy of the existing protocol and accounting for islet size distribution.* Cell Transplant, 2009. **18**(10): p. 1223-35.

106. Ricordi, C., et al., *Islet isolation assessment in man and large animals.* Acta Diabetol Lat, 1990. **27**(3): p. 185-95.
107. Girman, P., et al., *Digital imaging as a possible approach in evaluation of islet yield.* Cell transplantation, 2003. **12**(2): p. 129-133.
108. Olehnik, S.K., et al., *Quantitative analysis of intra- and inter-individual variability of human beta-cell mass.* Sci Rep, 2017. **7**(1): p. 16398.
109. Kin, T., et al., *Risk factors for islet loss during culture prior to transplantation.* Transpl Int, 2008. **21**(11): p. 1029-35.
110. Komatsu, H., et al., *A Multiparametric Assessment of Human Islets Predicts Transplant Outcomes in Diabetic Mice.* Cell Transplant, 2021. **30**: p. 9636897211052291.
111. Yu, X., et al., *A Smartphone-Fluidic Digital Imaging Analysis System for Pancreatic Islet Mass Quantification.* Front Bioeng Biotechnol, 2021. **9**: p. 692686.
112. Adewola, A.F., et al., *Microfluidic perifusion and imaging device for multi-parametric islet function assessment.* Biomed Microdevices, 2010. **12**(3): p. 409-17.
113. Chowdhury, A.S., et al. *Cell tracking in video microscopy using bipartite graph matching*. in *2010 20th International Conference on Pattern Recognition*. 2010. IEEE.
114. Jennings, B.R. and K. Parslow, *Particle-Size Measurement - the Equivalent Spherical Diameter.* Proceedings of the Royal Society of London Series a-Mathematical Physical and Engineering Sciences, 1988. **419**(1856): p. 137-149.
115. Fitzgibbon, A., M. Pilu, and R.B. Fisher, *Direct least square fitting of ellipses.* Ieee Transactions on Pattern Analysis and Machine Intelligence, 1999. **21**(5): p. 476-480.
116. Niclauss, N., et al., *Computer-Assisted Digital Image Analysis to Quantify the Mass and Purity of Isolated Human Islets Before Transplantation.* Transplantation, 2008. **86**(11): p. 1603-1609.
117. Huang, H.H., S. Harrington, and L. Stehno-Bittel, *The Flaws and Future of Islet Volume Measurements.* Cell Transplant, 2018. **27**(7): p. 1017-1026.
118. Qi, M., et al., *Human pancreatic islet isolation: Part I: digestion and collection of pancreatic tissue.* J Vis Exp, 2009(27).
119. Qi, M., et al., *Human pancreatic islet isolation: Part II: purification and culture of human islets.* J Vis Exp, 2009(27).
120. Pisania, A., et al., *Quantitative analysis of cell composition and purity of human pancreatic islet preparations.* Lab Invest, 2010. **90**(11): p. 1661-75.
121. Kitzmann, J.P., et al., *Islet preparation purity is overestimated, and less pure fractions have lower post-culture viability before clinical allotransplantation.* Transplant Proc, 2014. **46**(6): p. 1953-5.
122. Matschinsky, F.M. and J.E. Ellerman, *Metabolism of glucose in the islets of Langerhans.* J Biol Chem, 1968. **243**(10): p. 2730-6.
123. Bentsi-Barnes, K., et al., *Detailed protocol for evaluation of dynamic perifusion of human islets to assess beta-cell function.* Islets, 2011. **3**(5): p. 284-90.
124. Mohammed, J.S., et al., *Microfluidic device for multimodal characterization of pancreatic islets.* Lab Chip, 2009. **9**(1): p. 97-106.
125. Xing, Y., et al., *A pumpless microfluidic device driven by surface tension for pancreatic islet analysis.* Biomed Microdevices, 2016. **18**(5): p. 80.
126. Johnson, L.V., M.L. Walsh, and L.B. Chen, *Localization of mitochondria in living cells with rhodamine 123.* Proc Natl Acad Sci U S A, 1980. **77**(2): p. 990-4.

127. Yin, J., et al., *Small molecule based fluorescent chemosensors for imaging the microenvironment within specific cellular regions.* Chemical Society Reviews, 2021. **50**(21): p. 12098-12150.
128. Figueroa, J.A., et al., *Selectivity and specificity of small molecule fluorescent dyes/probes used for the detection of Zn2+ and Ca2+ in cells.* Metallomics, 2014. **6**(2): p. 301-15.
129. Nicoletto, R.E. and C.M. Ofner III, *Cytotoxic mechanisms of doxorubicin at clinically relevant concentrations in breast cancer cells.* Cancer Chemotherapy and Pharmacology, 2022. **89**(3): p. 285-311.
130. Chen, M., et al., *Genetically Encoded, Photostable Indicators to Image Dynamic Zn(2+) Secretion of Pancreatic Islets.* Anal Chem, 2019. **91**(19): p. 12212-12219.
131. Barnett, L.M., T.E. Hughes, and M. Drobizhev, *Deciphering the molecular mechanism responsible for GCaMP6m's Ca2+-dependent change in fluorescence.* PloS one, 2017. **12**(2): p. e0170934.
132. Babenko, A.P., G. Gonzalez, and J. Bryan, *The tolbutamide site of SUR1 and a mechanism for its functional coupling to K(ATP) channel closure.* FEBS Lett, 1999. **459**(3): p. 367-76.
133. Shyng, S., T. Ferrigni, and C.G. Nichols, *Regulation of KATP channel activity by diazoxide and MgADP. Distinct functions of the two nucleotide binding folds of the sulfonylurea receptor.* J Gen Physiol, 1997. **110**(6): p. 643-54.
134. Yu, X., et al., *Smartphone-microfluidic fluorescence imaging system for studying islet physiology.* Front Endocrinol (Lausanne), 2022. **13**: p. 1039912.
135. Bashkatov, A.N., et al., *Glucose and mannitol diffusion in human dura mater.* Biophys J, 2003. **85**(5): p. 3310-8.
136. Aurnhammer, C., et al., *Universal real-time PCR for the detection and quantification of adeno-associated virus serotype 2-derived inverted terminal repeat sequences.* Hum Gene Ther Methods, 2012. **23**(1): p. 18-28.
137. Qureshi, F.M., et al., *Stress-induced dissociations between intracellular calcium signaling and insulin secretion in pancreatic islets.* Cell calcium, 2015. **57**(5-6): p. 366-375.
138. *Your Kidneys & How They Work*. Available from: https://www.niddk.nih.gov/health-information/kidney-disease/kidneys-how-they-work.
139. Narayanan, S. and H.D. Appleton, *Creatinine: a review.* Clin Chem, 1980. **26**(8): p. 1119-26.
140. Patel, S.S., et al., *Serum creatinine as a marker of muscle mass in chronic kidney disease: results of a cross-sectional study and review of literature.* Journal of cachexia, sarcopenia and muscle, 2013. **4**: p. 19-29.
141. Mohabbati-Kalejahi, E., et al., *A review on creatinine measurement techniques.* Talanta, 2012. **97**: p. 1-8.
142. Hervey, G.R., *Determination of creatinine by the Jaffe reaction.* Nature, 1953. **171**(4364): p. 1125.
143. Spierto, F.W., M.L. MacNeil, and C.A. Burtis, *The effect of temperature and wavelength on the measurement of creatinine with the Jaffe procedure.* Clin Biochem, 1979. **12**(1): p. 18-21.
144. Syme, N.R., et al., *Clinical and Analytical Impact of Moving from Jaffe to Enzymatic Serum Creatinine Methodology.* J Appl Lab Med, 2020. **5**(4): p. 631-642.
145. Delanghe, J.R. and M.M. Speeckaert, *Creatinine determination according to Jaffe—what does it stand for?* Nephrology Dialysis Transplantation Plus, 2011. **4**(2): p. 83-86.

146. Fossati, P., L. Prencipe, and G. Berti, *Enzymic creatinine assay: a new colorimetric method based on hydrogen peroxide measurement.* Clin Chem, 1983. **29**(8): p. 1494-6.
147. Schmidt, R.L., et al., *A Risk Assessment of the Jaffe vs Enzymatic Method for Creatinine Measurement in an Outpatient Population.* PLoS One, 2015. **10**(11): p. e0143205.
148. Wang, A.-B., et al., *A novel lab-on-a-chip design by sequential capillary–gravitational valves for urinary creatinine detection.* Sensors and Actuators B: Chemical, 2016. **222**: p. 721-727.
149. Chen, S.J., et al., *Microfluidic Sliding Paper-Based Device for Point-of-Care Determination of Albumin-to-Creatine Ratio in Human Urine.* Biosensors (Basel), 2022. **12**(7).